Modeling and Design of a Level-2 Onboard Lithium-ion Battery Charging System for ECADO Four-wheel Electric Vehicle

Yosef Dentamo Setore

A Thesis Submitted to

The Department of Electrical Power and Control Engineering

School of Electrical Engineering and Computing

Presented in Partial Fulfillment of the Requirement for the Master of Science Degree in Electrical Power and Control Engineering (Specialization in Power Electronics)

Office of Graduate Studies

Adama Science and Technology University

Adama, Ethiopia

October, 2020

Modeling and Design of a Level-2 Onboard Lithium-ion Battery Charging System for ECADO Four-wheel Electric Vehicle

Yosef Dentamo Setore

Advisor: Tafesse Asrat (PhD)

A Thesis Submitted to

The Department of Electrical Power and Control Engineering

School of Electrical Engineering and Computing

Presented in Partial Fulfillment of the Requirement for the Master of Science Degree in Electrical Power and Control Engineering (Specialization in Power Electronics)

Office of Graduate Studies

Adama Science and Technology University

Adama, Ethiopia

October, 2020

APPROVAL OF BOARD OF EXAMINERS

We, the undersigned, members of the Board of Examiners of the final open defense by Yosef Dentamo Setore have read and evaluated his thesis entitled "Modeling and Design of a Level-2 Onboard Lithium-ion Battery Charging System for ECADO Four-wheel Electric Vehicle" and examined the candidate. This is, therefore, to certify that the thesis has been accepted in partial fulfillment of the requirement of the Degree of Masters in Power Electronics.

Name	Signature	Date
______________________	______________	______________
Name of Student		
______________________	______________	______________
Advisor		
______________________	______________	______________
External Examiner		
______________________	______________	______________
Internal Examiner		
______________________	______________	______________
Chair Person		
______________________	______________	______________
Head of Department		
______________________	______________	______________
School Dean		
______________________	______________	______________
Postgraduate Dean		

DECLARATION

I hereby declare that this MSc thesis is my original work and has not been presented for a degree in any other university, and all sources of material used for this thesis have been duly acknowledged.

Name: ____________________________

Signature:__________________________

This MSc thesis has been submitted for examination with my approval as a thesis advisor.

Name: ____________________________

Signature: _________________________

Date of submission: ______________________

ADVISOR APPROVAL SHEET

To: Department of Electrical Power and Control Engineering (EPCE)

Subject: Thesis Submission

This is to certify that the thesis entitled "Modeling and Design of a Level-2 Onboard Lithium-ion Battery Charging System for ECADO Four-wheel Electric Vehicle", submitted in partial fulfillment of the requirements of the Master of Science Degree in Electrical Power and Control Engineering, postgraduate in Power Electronics, and has been carried out by Yosef Dentamo Setore Id No. PGR/18080/11 under my supervision. Therefore, I recommend that the student has fulfilled the requirements and hereby he can submit the thesis to the department.

Name of Advisor	Signature	Date

ACKNOWLEDGMENT

First and dearest I would like to thank my supervisor **Dr. Tafesse Asrat** for his supervision, friendly attitude, and sharing of many good ideas. Regardless of his often-high workload, he always makes time to answer questions as well as giving encouraging advice. You are highly appreciated!

I am also very grateful to **staff members of CTVE** for lots of advice and helping in preparing the thesis documentation, but also for good ideas and discussions regarding everything from implementations of the system in Simulink in general.

I would moreover like to thank **Mr. Minyamer Gelawe Wase (MSc.)** for his patience, helpful attitude, and sharing of his work regarding the organization of documents used in this thesis.

Finally, I would like to thank my whole family. Especially words cannot express how grateful I am to my father and friends for their love, encouragement, and all of the sacrifices that they have made on my behalf.

ABSTRACT

Electric vehicles are considered as one of the most suitable solutions to minimize both fossil fuel consumption and emission of greenhouse gases. However, the charging mechanism, battery design, and charging-discharge time are important factors that need to be taken into consideration, when designing electric vehicles. They also determine the success and acceptance of the vehicles in the car market. According to the current research trend, a level-two onboard battery charging system is favored as compared to other charging architectures, even if it has a slow charging time when compared with the off-board charging system. To achieve improved performance levels, the battery charging system needs to have a charger integrated with the battery management system. In this regard, an interleaved boost and LLC resonant converter-based isolated onboard battery charger which is integrated with the lithium-ion battery charging management system is implemented in this research for Ethiopia can do four-wheel electric vehicle. The charging system is modeled mathematically. Also, for implementation purposes, the corresponding models are done using MATLAB software tools. Different power factor correction stage converters and isolated DC-DC converter topologies are implemented and the performance of each is evaluated. Accordingly, the interleaved boost converter is used for power factor correction and minimizing total harmonic distortion of the charging system due to its incredible performance capability. In the back-end, a multi-resonant full-bridge LLC converter is adopted for galvanic isolation and dc voltage regulation, due to their excellent performance compared to other converter topologies. This research also includes a battery management system that is only related to charging an electric vehicle to demonstrate how battery management system manages the charging system. The battery management system monitors cells, controls the charging system to charge in the Constant Current-Constant Voltage charging algorithm, estimates the state of charge, and protects the charging system from damage. A 7.6kW charger is designed to charge the battery pack with an output voltage range of 320V to 420V. As a result, the designed electric vehicle charger achieved a unity power factor, total harmonic distortion of 3.17, and the LLC converter maintain ZVS and ZCS for the overall charging stage. This implementation makes the overall battery charging system to have excellent performance.

Keywords: *ECADO-4EV, interleaved boost converter, LLC resonant converter, CC-CV charging, BMS*

TABLE OF CONTENTS

DECLARATION i

ACKNOWLEDGMENT iii

ABSTRACT iv

LIST OF FIGURES ix

LIST OF TABLES xii

LIST OF ACRONYMS xiii

LIST OF SYMBOLS xv

CHAPTER 1 1

INTRODUCTION 1

1.1 Background 1

1.2 Statement of the Problem 3

1.3. Objectives of the Study 4

1.3.1. General Objective 4

1.3.2. Specific Objectives 4

1.4. Significance of the Study 4

1.5. The Motivation of the Study 4

1.6. Scope and Limitation of the Study 5

1.7. Thesis Outline 5

CHAPTER 2 6

THEORETICAL BACKGROUND AND LITERATURE REVIEW 6

2.1. Chapter Overview 6

2.2. Electric Vehicles 6

2.3. Review of Battery for EVs 7

2.3.1. Comparison of Li-Ion Based Battery Chemistries for Electric Vehicle 10

2.4. Battery Charging Technology 10

2.4.1. Charging Strategy.. 10

2.4.2. Charging Power Levels 11

2.4.3. On-board and Off-board Chargers 12

2.5. Circuit Configurations of Onboard Charger 13

2.5.1. Challenges in Onboard Charger Design.. 15

2.6. Review of Front-end AC/DC PFC Topologies 16

2.6.1. Conventional Boost PFC Converter 17

2.6.2. Bridgeless Boost PFC Converter 18

2.6.3. Interleaved Boost PFC Converter 18

2.7. Review of Second Stage Isolated DC-DC Topologies 19

2.7.1. Full-bridge Isolated PWM Buck Converter 19

2.7.2. Full-bridge Phase-shift PWM Converter 20

2.7.3. Full-bridge Series Resonant Converter 22

2.7.4. Full Bridge LLC Resonant Converter 22

2.8. Lithium-ion Battery Management System 24

2.8.1. Basic Functions of the Battery Management System 25

2.9. Related Electric Vehicle OBC Topologies 27

2.9.1. Industry Established Charging Solutions 27

2.9.2. OBCs in Research Environment 28

CHAPTER 3.. 34

METHODOLOGY 34

3.1. Introduction 34

3.2. Methods 34

3.3. Block Diagram of the Proposed System... 35

3.4. General Boost Converter ... 37
3.5. Interleaved Boost Converter ... 39
3.5.1. Interleaving Effect on Input Ripple Current ... 39
3.5.2. Interleaving Effect on Magnetic Volume Reduction ... 41
3.5.3. Interleaving Effect on the Output Capacitor ... 42
3.6. Full-bridge LLC Converter ... 44
3.6.1. Operation Analysis With $f < fs/2$ ... 45
3.6.2. Operation Analysis with $fs/2 < f < fs$ ... 47
3.6.3. Operation Analysis with $fs < f < fp$ (f close to fs) ... 49
3.6.4. Operation Analysis with $fs < f < fp$ (f close to fp) ... 50
3.6.5. Operation Analysis with $f > fp$ ... 52
3.6.6. Summary of Switching Conditions ... 54
3.7. Battery Management System ... 54
3.7.1. Battery Cell Modeling ... 55
3.7.1. State of Charge Estimation of the Battery Pack. ... 62
3.7.2. Battery Cell Balancing ... 66
3.8. Battery Specifications ... 69
3.8.1. Designing a 7.6 kW EV Charger ... 71
3.8.2. Charging Profile of The Li-ion Battery ... 72
3.8.3. Interleaved Boost PFC Converter Design ... 73
3.8.4. Full-Bridge LLC Converter Design ... 75
CHAPTER 4 ... 79
RESULT AND ANALYSIS ... 79
4.1. Chapter Review ... 79
4.2. The Proposed Electric Vehicle Charger Results ... 79

4.2.1. Front-end Interleaved Boost Converter Results. 79

4.2.2. Back-end LLC-Resonant DC-DC Converters Results 81

4.3. Results Related to the Battery Management System 87

CHAPTER 5 90

CONCLUSIONS AND RECOMMENDATIONS 90

5.1. Conclusions 90

5.2. Recommendations 91

References 92

Reference Links 102

Appendixes 103

Appendix A: Appendixes Related to Modeling of the Battery Management System. 103

Appendix B. Related to Onboard Charging MATLAB/Simulink Model 109

Appendix C: Related to the Battery Management System... 111

Appendix D. Appendixes Related to ECADO-4EV 114

Appendix E: Appendixes Related to Data Collection 115

LIST OF FIGURES

Figure 2. 1 Comparisons of different types of Li-ion batteries used in EVs from the following perspectives: specific energy (capacity), specific power, safety, performance, life span, and cost (the outer hexagon is most desirable)......... 10

Figure 2. 2 (a) Typical block diagram of ac/dc PFC stage, (b) equivalent circuit model. 14

Figure 2. 3 Typical configurations of isolated dc/dc topology. 14

Figure 2. 4 Common switching networks, (a) half-bridge, (b) half-bridge with a split capacitor, (c) two-switch forward, (d) full-bridge 14

Figure 2. 5 Common rectifier networks, (a) center tapped rectifier, (b) current doubler rectifier, (c) half wave rectifier, (d) full bridge rectifier 15

Figure 2. 6 Single-phase boost PFC converter. 17

Figure 2. 7 Bridgeless PFC boost converter... 18

Figure 2. 8 Interleaved PFC boost converter. 18

Figure 2. 9 Full bridge isolated PWM buck converter. 20

Figure 2. 10 Waveforms of the full-bridge isolated buck converter. 20

Figure 2. 11 Full bridge phase-shift PWM converter. 21

Figure 2. 12 Waveforms of the full-bridge phase-shift converter. 21

Figure 2. 13 Full bridge SRC PFM converter. 22

Figure 2. 14 Full bridge LLC PFM converter. 23

Figure 2. 15 Schematic diagrams of a typical BMS... 24

Figure 3. 1 Block diagram of the research methodology 34

Figure 3. 2 General system architecture of a battery charger 35

Figure 3. 3 Schematic of proposed level 2 onboard charger. 36

Figure 3. 4 Schematic of the general boost converter. 37

Figure 3. 5 Simulated waveforms of the general boost converter. 38

Figure 3. 6 Schematic of the two-phase interleaved boost converter................................ 39

Figure 3. 7 Input current ripple of 2-phase interleaved boost converter. (a) $d < 0.5$. (b) $d > 0.5$. 40

Figure 3. 8 Effectiveness of input ripple cancellation for interleaved converters............ 41

Figure 3. 9 Output capacitor current ripple of the two-phase interleaved boost converter. 43

Figure 3. 10 Effectiveness capacitor RMS current reduction for interleaved converters. 43

Figure 3. 11 Schematic of a full bridge LLC resonant converter.................................... 44

Figure 3. 12 Simulated waveforms of LLC resonant converter in ZCS operation with ... 45

Figure 3. 13 Operating modes of LLC resonant converter in ZCS operation with $f < fs/2$ ($iLr(to) > 0$). 46

Figure 3. 14 Simulated waveforms of LLC resonant converter with $fs/2 < f < fs$............ 47

Figure 3. 15 Operating modes of LLC resonant converter with $fs/2 < f < fs$. 48

Figure 3. 16 Simulated waveforms of LLC resonant converter with $fs< f < fp$ (f close to fs) 49

Figure 3. 17 Operating modes of LLC resonant converter with $fs< f < fp$ (f close to fs). . 50

Figure 3. 18 Simulated waveforms of LLC resonant converter $fs< f < fp$ (f close to fp). . 51

Figure 3. 19 Operating modes of LLC resonant converter $fs< f < fp$ (f close to fp).......... 51

Figure 3. 20 Simulated waveforms of LLC resonant converter with $f > fp$. 52

Figure 3. 21 Operating modes of LLC resonant converter with $f > fp$............................. 53

Figure 3. 22 Structure of PNGV model 56

Figure 3. 23 Schematic of current and voltage profiles in the HPPC test [87]................. 57

Figure 3. 24 Process of parameter identification. 59

Figure 3. 25 experimental discharge characteristics of Li-ion battery cell 60

Figure 3. 26 Parameter optimization circuit for lithium-ion battery model...................... 61

Figure 3.27 Parameter estimation using 1-RC pair.. 61

Figure 3.28 Parameter estimation using 3-RC pair.. 62

Figure 3. 29 MATLAB model for unscented Kalman filter based battery soc estimation65

Figure 3. 30 state transition function.. 65

Figure 3. 31 Overall battery management system... 66

Figure 3. 32 The circuit that controls CC-CV charging 66

Figure 3. 33 Passive switched shunt battery cell balancing circuit 67

Figure 3. 34 Developed balancing logic algorithm 68

Figure 3. 35 Charging characteristics of a Li-Ion battery cell. 72

Figure 3. 36 Charging profile of the Li-Ion battery pack. 73

Figure 3. 37 Duty cycles corresponding to different DC link voltages 74

Figure 3. 38 Dc characteristics of the designed 7.6kW LLC converter: a) voltage characteristic b) current characteristic 77

Figure 4. 1 Interleaved converter input voltage, current and output voltages 80

Figure 4. 2 Power factor of the charging system. 80

Figure 4. 3 Total harmonic distortions of the charger. 80

Figure 4. 4 output voltage and output current @192KHz 81

Figure 4. 5 Resonant circuit voltage and current at 192kHz 82

Figure 4. 6 output voltage and output current @ 182.5 kHz 82

Figure 4. 7 Resonant circuit voltages and current @182.5kHz 83

Figure 4. 8 LLC dc-dc converter output voltage and current at turning point (*Vbat* = 420V, *Ibat* = 18.1A at 168.85KHz) 84

Figure 4. 9 Resonant circuit voltages and current @168.85kHz 84

Figure 4. 10 Output voltage and current at the endpoint of the charging 85

Figure 4. 11 Soft switchings of LLC converter at (a) 168.85KHz and 420V (b) 182.5KHz and 360V (c) 192KHz and 320V 86

Figure 4. 12 Battery cell voltage and current 87

Figure 4. 13 Temperature of the battery cell during charging and discharging 88

Figure 4. 14 Battery pack voltage in battery management circuit 89

Figure 4. 15 State of charge of each battery cell in the pack 89

LIST OF TABLES

Table 2. 1 The comparison of popular characteristics and behavior of different batteries for EVs . 8

Table 2. 1 The comparison of the three charging power levels 12

Table 2. 2 The comparison of on-board and off-board chargers 13

Table 2. 3 Comparison of AC-DC PFC topologies for EV battery charging 19

Table 2. 4 Comparison of isolated converters in EV charging applications 23

Table 3. 1 Switching conditions of LLC converter 54

Table 3. 2 Summary of the unscented Kalman filter approach for SOC estimation 63

Table 3. 3 Tractive motor and vehicle specification taken from ECADO-4EV proposal 69

Table 3. 4 Battery specifications used [ECADO-4EV] 69

Table 3. 5 Summary of parameters used in the design of an interleaved boost and full-bridge LLC resonant converter-based Li-ion battery onboard charger. 78

LIST OF ACRONYMS

BMS	Battery Management System
CC	Constant Current
CC-CV	Constant Current-Constant Voltage
CCM	Continuous Conduction Mode
CM	Common Mode
CTVE	Center of Transport and Vehicle Engineering
CV	Constant Voltage
DAB	Dual Active Bridge
DCM	Discontinuous Conduction Mode
DM	Differential-Mode
DQ	Direct-Quadrature
DSP	Digital signal processing
ECADO-4EV	Ethiopia Can Do four wheel Electric Vehicle
EKF	Extended Kalman Filter
EMI	Electromagnetic Interference
FB-SRC	Full Bridge-Series Resonant Converter
HFT	High-Frequency Transformers
HPPC	Hybrid Pulse Power Characterization
IEEE	Institute of Electrical and Electronics Engineers
IPCC	Intergovernmental Panel on Climate Change
KF	Kalman Filter
MMSE	Minimum Mean Square Error
NiCD	Nickel Cadmium
NiMH	Nickel-Metal Hydride
NN	Neural Network
OCV	Open-Circuit Voltage

PDPS	Primary-side Dual Phase-Shift
PF	Power Factor
PFC	Power Factor Correction
PFM	Pulse Frequency Modulation
PLL	Phase-Lock Loop
PNGV	Partnership for a New Generation of Vehicles
PWM	Pulse-Width-Modulation
RMS	Root Mean Square
SAE	Society of Automotive Engineers
SDPS	Secondary side Dual-Phase-Shift
SOC	State Of Charge
SVPWM	Space Vector Pulse Width Modulation
THD	Total Harmonic Distortion
UKF	Unscented Kalman Filter
UNFCCC	The United Nations Framework Convention on Climate Change
WBG	Wide Band Gaps
XFC	Extreme Fast Charging
ZCS	Zero Current Switching
ZVS	Zero-Voltage-Switching

LIST OF SYMBOLS

C	Capacitor
d	Duty cycle
D	Driving range
E	Energy
fp	Primary resonant frequency
fs	Secondary resonant frequency
I	Current
L	Inductor
P	power
Q	Discharging capacity
R	Resistor
T	Time
U	Voltage in battery modeling
V	Voltage

CHAPTER 1

INTRODUCTION

1.1 Background

In Ethiopia, over 90 percent of exports and imports are transported by road transport [1]. Because of the emerging industrialization and intensification of trade-related activities, the total vehicle fleet in the country has been growing at an annual rate of >10%, increasing from 95,925 vehicles in 1996/1997 [2] to 831,265 motor vehicles in 2017/2018 [3]. Unless preventive and adaptive measures are taken, the alarmingly growing number of internal combustion engine vehicles will be a hair-raising concern in addressing climate change. The alternative solution to continue the transportation is to replace the engine-based vehicle with the electric-based vehicle. EV is essential and simple to use for a country like Ethiopia which is expecting very big MW power generation from the Grand Ethiopian renaissance dam.

The development of Electric Vehicle (EV) has rapidly proliferated in recent years worldwide. And rechargeable batteries used as energy storage devices are playing an increasingly significant role in EV application. In this case, lithium-ion cells, due to their higher energy density, high energy efficiency, lightweight, and good cycle life, may provide a good solution for powering the EV [4]. Usually, an EV powered by lithium-ion battery storage can only travel at full power over a limited range. The limited usable range makes it necessary to develop some kind of battery charger installed on the electric vehicle itself [5]. And the charger should be designed properly for the best system performance.

Currently available battery chargers, which extracted power from an ac-line source, adopted mainly conventional boost ac/dc converter and different isolated DC-DC converters to rectify and control the power flow from the grid to charge the battery system [4]. Such a charging circuit drew a high charging current ripple and low efficiency. Nowadays topologies with high switching frequencies are used to reduce the charging current ripple and extend the battery life [6] [7]. In this research work interleaved boost converter is used to minimize input current ripple and to maintain power factor to unity. And also, LLC multi resonant converter is used to regulate the dc voltage obtained from the front-end converter and to charge the battery pack of the electric vehicle. Those converter topologies have better performance when compared with others by making the charging system to operate at unity power factor, by minimizing the total harmonic distortion below 4%, and by making the converter to operate at ZVS and ZCS during its charging cycle.

On the other hand, the high availability characteristics of the charger in EV application require the powering control system to be robust, and operate without instability, under a variety of electrical and environmental conditions. However, the nonlinearity of lithium-ion batteries presents some difficulties for designing the controller of this system [8]. To overcome the negative factor, an electrical model is set up and its parameters are evaluated through the method of pulse current discharge. Based on the accurate model, a proper control strategy is presented and analyzed in detail.

Furthermore, the charging strategy should be considered in the EV application. Because the life cycles of lithium-ion batteries are easily affected by undercharging and overcharging. Many battery charging strategies have been proposed, such as constant current (CC), constant voltage (CV), and constant current-constant voltage (CC-CV) strategies [9]. CC-CV charging strategy is widely used these days among these strategies aforementioned. And the strategy can effectively avoid overcharging. This thesis presents a lithium-ion-powered battery charging system that comprises of battery charger and battery management system.

ASTU-CTVE (Center of Transport and Vehicle Engineering) is planning to design an Electric car called Ethiopia Can Do – Four-wheel Electric Vehicle. Most of the data specifications of the traction battery and charging profile will be used from this proposal. The work here is intended to be a standardized charging system that will charge ECADO-4EV’s battery pack. In addition to this, the proposed charging system will possibly motivate other researchers and local industries to opt for and use local designs and specifications for their products. This will encourage innovation and indigenous inventions to flourish.

1.2 Statement of the Problem

IPCC report shows that the contribution of transport to the total greenhouse gas emissions in 2004 was about 23% [10]. Under the international energy agency baseline scenario, emissions related to global transport could grow to 35% in 2030. The UNFCCC indicated that road transport accounts for 74% of total transport-related CO_2 emissions. Ethiopia's contribution to global greenhouse gas emissions has been practically negligible [11]. Overall, Ethiopia's total emissions represent 0.3% of global emissions [12]. However, the projected environmental impact of conventional economic development in Ethiopia risks following the pattern observed around the globe. If current practices prevail, greenhouse gas emissions in Ethiopia will more than double from 150 megatons CO_2 to 400 megatons CO_2 in 2030 [13]. According to the report of the Ethiopian petroleum supply enterprise, 932,057 Metric Tons of refined petroleum products have been imported from July to September 2019. The payment settlement shows that above Birr 20.53 Billion have been paid for the petroleum product supplied in the period mentioned [L1].

Nowadays, with the global concern for greenhouse gases and environmental pollution, electrical vehicles are being developed in quick paces for both private and commercial purposes. However, such technology still poses some difficulties, especially in the energy storage system [3], This being the main reason why chargers are once again an essential part in the use of batteries. Currently, a large number of chargers can be found in the market, but many of them do not include features of great importance for the user of electric vehicles. Four of these characteristics can be efficiency, PF, THD of input current, and implemented charging strategies. Each of these features is dependent on the design of the charger and its integration with the battery using the battery management system. The efficiency of the converter requires excellent use of energy drawn from the grid. Sometimes that has a strong impact on consumers and the environment. The power factor and total harmonics features are related to the efficiency, but in addition to this, they are required to meet the specified standards in IEEE [14]. Charging strategy is another characteristic of a charger that can only be achieved by integrating the charger with the battery management system. The designed charging system can improve the indicated problems by specifically analyzing each part or charging system and by managing the charging algorithm using the battery management system.

1.3. Objectives of the Study

1.3.1. General Objective

The main objective of this thesis is to design and simulate a battery charging system for ECADO-4EV which is composed of Electric vehicle charger and battery management systems.

1.3.2. Specific Objectives

- To design the electric vehicle charging system with an appropriate PFC circuit, DC-DC converters, and storage system.
- To design the battery management system which manages the charging process of the electric vehicle.
- To simulate the designed EV charger and battery management system in MATLAB and
- To evaluate the performance of the charging system in the wide range voltage of the lithium-ion battery pack.

1.4. Significance of the Study

The global trend is shifting the energy source usage from non-renewable sources that will not available after a few decades to a renewable energy source that can exist forever. Similarly, ECADO- 4EV members are trying to develop EV for the Ethiopian market. Since the above-mentioned objectives are certainly fulfilled, this research study can support the trend started by ECADO-4EV (ASTU Center of Excellency) members by providing a charging system which can make the electric vehicle to charge from the grid. Similarly, As EV technology is a recent development in Ethiopia, this thesis work will be an eye-opening for the researcher who wants to invest their time and money.

1.5. The Motivation of the Study

Due to the futurity of EV technology, it is very interesting to research this area. The one who is professional EV drive is adeptly beneficial because a huge market is coming. The battery and power electronic converter technology are updating from time to time which gives hope for the easy to use EV. Power electronic converter and battery technology are getting popularity rapidly. They have been increasingly used in automotive, aerospace, consumer, industrial automation equipment, and instrumentation due to their flexibility higher efficiency, longer operational life.

1.6. Scope and Limitation of the Study

This research study includes the design and simulation of the EV battery charging system by using MATLAB software. The performance of different converter topology for the EV battery charging system is compared and analyzed. DSP hardware implementation is not included. Specification of converters and battery specified by ECADO-4EV is used. But some missing data is obtained by using analysis of existing data and calculation. The study doesn't include the detail about the EV motor and other parts of the EV. The comparison of power electronic converters and battery for EV battery charging systems is taken from literature because it is very difficult to get those converters and batteries around. If they would have available the comparison was done in the laboratory. Due to the global pandemic of the coronavirus, the price of the converter is increased dramatically and availability is another problem. Because of the problem stated above the hardware implementation of the research work could be excluded.

1.7. Thesis Outline

This thesis is organized into five chapters.

Chapter 1: Presents the background of the study, statement of the problem, objective of the study, significance of the study, motivation, scope and limitation, area of applications, and definition of terms.

Chapter 2: Gives insight on the background and structural overview of the electric vehicle battery charging system also includes the literature review of the proposed system.

Chapter 3: Covers the analysis of data, electric vehicle battery charging system modeling, and the proposed system development.

Chapter 4: Presents the results of the research wok and briefly discuss the output of the simulation.

Chapter 5: Discusses the conclusions and recommendations.

CHAPTER 2

THEORETICAL BACKGROUND AND LITERATURE REVIEW

2.1. Chapter Overview

In this chapter the background and varieties of electric vehicle battery charging solutions are discussed in detail. Advantage of interleaved boost and LLC resonant converter based on-board electric vehicle battery charging system is compared with another electric vehicle battery charger. Its recent world-wide application in research and industry, the existing control mechanism, and other related applications are reviewed and discussed.

2.2. Electric Vehicles

The world energy consumption due to the transport sector is expected to show dramatic growth of around 44% from 2008 to 2035 [15]. This consumption is responsible for the largest share (63%) of the total increase in petroleum and other fossil fuel usage from 2010 to 2040.

The combustion of fossil fuels, a non-renewable and finite resource, has caused increasing air pollution, ozone damage, acid rain, and global warming. Therefore, new technologies for alternative vehicles are of great interest to researchers, industry, governments, and the general public nowadays [16].

Electric vehicles (EVs) use electric motors for propulsion and are directly powered from an energy store rather than indirectly via internal combustion engines (ICEs). Compared with the traditional fossil fuel-powered vehicles, EVs are more eco-friendly with the attractive properties of lower greenhouse emissions, lower fuel usage and reduced air pollution. There is thus a growing interest in EVs globally.

2.3. Review of Battery for EVs

The performance of the EV highly depends on the performance of the battery and BMS. To meet the requirements of dynamic performance, safety, economy, and environmental friendliness of the EVs, the battery system should meet the following requirements:

- High specific energy: Improving the specific energy of the battery can greatly improve the driving mileage of the EVs, and also reduce the mass and volume of vehicles.
- High specific power: The specific power of the battery can effectively improve the vehicle dynamic performance of EVs so that it has excellent acceleration performance [17].
- High safety: The safety of the battery can reduce the probability of dangerous accidents such as fire and explosion of the vehicles which are caused by liquid leakage, short-circuit, collision, and so on [18].
- Long service life: Most of the cost of EVs comes from the battery system, so extending the battery life can greatly reduce the use and maintenance cost, thus reducing the cost of the vehicle [19].
- Low self-discharge rates: A low self-discharge rate can decrease the capacity degradation rate of the battery and extend its service lifetime [20].
- Low cost: Reducing the cost of the battery can effectively reduce the cost of the vehicles and improve the product competitiveness of the EVs.
- Environmental friendliness: The battery will help to establish battery recycling standards and prevent secondary pollution to the environment.

Currently, three main battery technologies are extensively used for EVs: the lead-acid battery, the nickel-metal hydride (NiMH) battery, and the Lithium-ion (Li-ion) battery technologies, whose key features are shown in Table 2.1 [21].

The lead-acid battery is used to power early EVs such as GM EV1 [22]. It has the advantages of good discharge power capacity enabling the fast response to the load changes. Meanwhile, the cost is affordable due to the mature development of the technology. However, the low energy density, heavyweight, and short life span due to the deep discharging deterioration make it not suitable for the latest EVs.

Table 2. 1 The comparison of popular characteristics and behavior of different batteries for EVs [21].

Type	Life cycle	Nominal voltage (v)	Energy density ($w.h.kg^{-1}$)	Power density ($w.kg^{-1}$)	Charging efficiency (%)	Self-discharge rate (% $moth^{-1}$)	Charging Temperature (^0C)	Discharging Temperature (^0C)
Li-ion	600-3000	3.2-3.7	100-270	250-680	80-90	2-3	0 to 45	-20 to 60
Lead acid	200-300	2.0	30-50	180	50-95	4-6	-20 to 50	-20 to 50
NiCD	1000	1.2	50-80	150	70-90	20	0 to 45	-20 to 65
NiMH	300-600	1.2	60-120	250-1000	65	30	0 to 45	-20 to 65

The NiMH batteries are employed in Toyota Prius [23] and Honda Insight [24]. Compared to the lead-acid, a NiMH battery has higher power density, due to simpler charger/discharge reactions [25]. NiMH has the high self-discharge rate which means the battery will lose charge when not used. Also, it has a higher cost and low charge acceptance capability in high-temperature conditions which reduces the charging efficiency.

Lithium-ion (Li-ion) battery has become one of the preferred energy storage units for the recent generation of EVs such as Nissan leaf [26]. Although the Li-ion battery has the issues need to be improved such as cell life, cell balance, cooling operation, cost, and safety, compared to other rechargeable batteries, Li-ion has the attractive features of higher energy density, a higher power rating (high cell voltage and output power), lower weight and great discharging power for faster acceleration.

2.3.1. Comparison of Li-Ion Based Battery Chemistries for Electric Vehicle

There are no perfect candidates for the electric powertrain, and Li-ion remains a great option. Li-ion battery also consists of several chemistries. Figure 2.1 graphically compares distinctive sorts of Li-ion batteries utilized in EVs considering several characteristics, with the larger colored area being more desirable. The major factors considered are specific energy, specific power, safety, performance, life span, and cost.

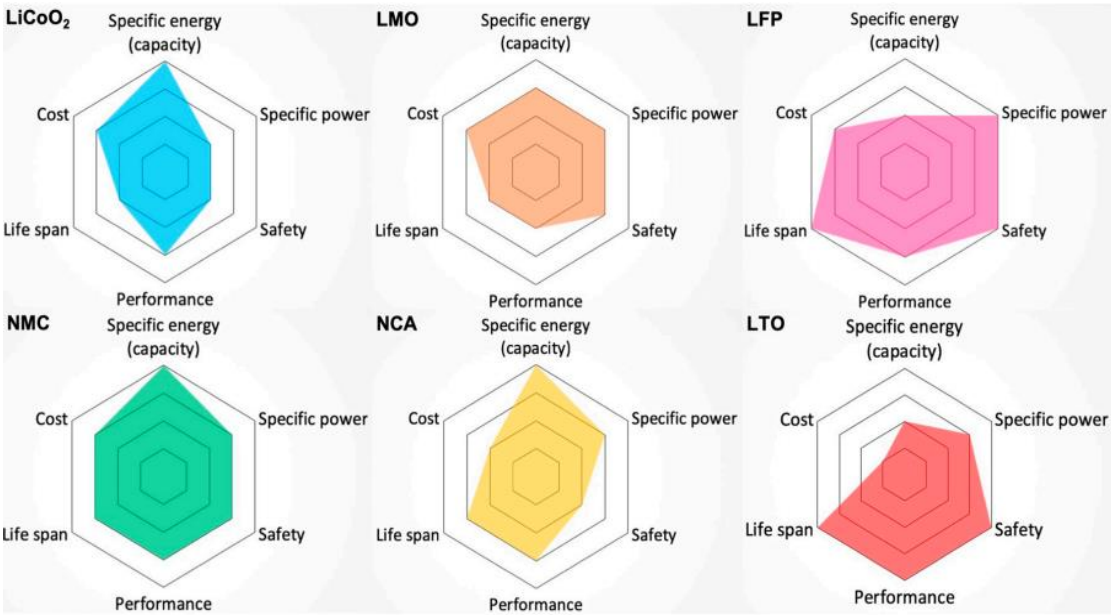

Figure 2. 1Comparisons of different types of Li-ion batteries used in EVs from the following perspectives: specific energy (capacity), specific power, safety, performance, life span, and cost (the outer hexagon is most desirable) [27].

Lithium Iron Phosphate (LiFePO4), Lithium Nickel Manganese Cobalt Oxide (NMC), and Lithium Manganese Oxide stand out as being superior among these six candidates. Due to its high specific power, longer life span, better safety concern, and tolerable cost: Lithium Iron Phosphate (LiFePO4) is used in this research work.

2.4. Battery Charging Technology

2.4.1. Charging Strategy

There are different charging methods including constant current (CC) [28], constant voltage (CV), constant power, taper current, etc. [29]. The constant voltage charger is the simplest method that charges the battery by providing the required current to obtain the constant battery voltage. It needs an extra circuit to protect the battery. Constant current charger supplies a fixed current (usually the maximum current to get fast charging) into the battery and the battery voltage increases linearly. A constant power charger is usually preferred for giant and costly batteries in a slow charging approach. It is worth noting that the main limitation when charging in a domestic environment, is the maximum current which should be less than the single-phase outlet fuse current.

For the Li-ion battery, the constant current constant voltage (CC-CV) charging scheme is usually employed [30]. In this CC-CV charging profile, the charging process includes two stages: the CC mode and CV mode. The first stage is the CC mode, during which the current should be regulated at a fixed value (usually the maximum current which the battery tolerates without causing damage) while the battery voltage increases rapidly to its rated maximum level. After that, further continuing the constant current charging will cause overcharging and excessive heating which might damage the battery.

To avoid this, when the battery voltage reaches the threshold voltage (nearly fully-charged voltage), the charging process is switched to the CV mode, during which the battery voltage is maintained at a constant value while the battery is slowly charged. Meanwhile, the battery charging current decreases to avoid over-charging of the battery until the current reaches a specific low value at which the charging process is terminated [31].

2.4.2. Charging Power Levels

EV OBCs are categorized as level-1, level-2, and level-3 chargers based on their power levels according to SAE J1772 standard [32].

1) Level-1: Level-1 EV chargers have the lowest charging power level and take the longest time to achieve full battery charge. The peak power of AC level-1 chargers is 3.8 kW [33].

2) Level-2: Level-2 EV chargers have increasing popularity within the EV community on a global scale. The peak power of level-2 chargers is 22 kW [32], [33]. Almost every popular EV worldwide utilizes level-2 OBCs in the 6.6 kW-7.8 kW range. This power level is most suitable for current battery capacities because full battery charging can be nearly completed in 4 hours to 8 hours.

3) Level-3 AC: Level-3 EV chargers are the highest charging power options for onboard charging. Level-3 AC-chargers offer three-phase AC for power levels between 22 kW and

43.5 kW [32], [33]. Level-3 AC-chargers can be on-board the vehicle. But it will be integrated with motor and other converters of an electric vehicle.

4) Level-3 DC: Level-3 DC-chargers provide direct power to the EV's battery for power levels up to 350 kW, or higher [34]. Due to their high-power level and hence bulky size, level-3 DC-chargers is located off-board the EV. DC level-3 is the fastest charging option, which for Extreme Fast Charging (XFC) is proposed to achieve 200 additional miles of driving range in 10 minutes or less [34]. However, the design of a ubiquitous high-power off-board charging infrastructure will take significant time as well as a substantial monetary investment. The discussion presented on EV charger classifications is summarized in Table 2.2.

Table 2. 2 The comparison of the three charging power levels [32]

SAE J1772 Level	Classification	Power rating (kW)	Charging time
AC Level 1	Slow charging	<3.7	10-12 hrs.
AC Level 2	Primary charging	3.7-22<22	4-8 hrs.
AC Level 3	AC fast charging	22-43.5	<1 hr.
DC level 3	Extremely fast charging	<200	<15 minutes

2.4.3. On-board and Off-board Chargers

Typically, the battery chargers for EVs are usually categorized into on-board chargers and off-board chargers, as shown in Table 2.3. Off-board chargers, also known as standalone fast-charging stations, act like filling stations for liquid fuel vehicles to provide rapid charge at high power [17]. Off-board charger stations are usually installed in public areas such as shopping centers, car parks, and motorway services which can greatly extend the range of pure-battery EVs [35]. There are reduced constraints of size, weight, or space to develop such an off-board station; however, these stations need significant investment and long-term construction.

In contrast, on-board chargers are mounted in the vehicles, provide simple charging at domestic user dwellings overnight when the EVs are plugged into a household utility outlet. As the charger can be built into the EV, it will not require significant extra cost compared to an off-board charger station.

Table 2. 3 The comparison of on-board and off-board chargers

Classification	Size limit	Weight limit	Space limit	Construction requirement	Level type	Typical charging time
Off-board	Less	Less	Less	Yes	50 kW	Fast charging less than 1 hour
On-board	Yes	Yes	Yes	Less	2-22 kW	Slow charging 4-12 hours

Despite the constraints such as size, weight, space limit the input power level, and slow charging, onboard charging is still a promising solution due to its compact structure, simplicity of usage, and low cost. Two technologies are available for the On-board charger, including the conductive method and inductive approach depending on the direct electrical contact between the grid and the vehicle [36].

As most EVs are being designed with a plug-in battery connector, a conductive battery system is a more common solution. According to the SAE J1772 standard [32], on-board charger usually adopts Level 1 and Level 2 which are supposed to be installed in the vehicle, and Level 3 is usually employed in the off-board charger.

2.5. Circuit Configurations of Onboard Charger

The first stage ac/dc PFC converter typically contains an EMI filter, rectifier, PFC converter, as well as a DC link capacitor as shown in Figure 2.2 (a). The PFC converter is controlled by a high-frequency signal to regulate the ac line current to follow the ac line voltage and frequency. Ideally, the AC-DC PFC stage could be equivalent to a resistive load, as shown in Figure 2.1(b), to eliminate the total harmonic distortion, and to maximize the power transfer.

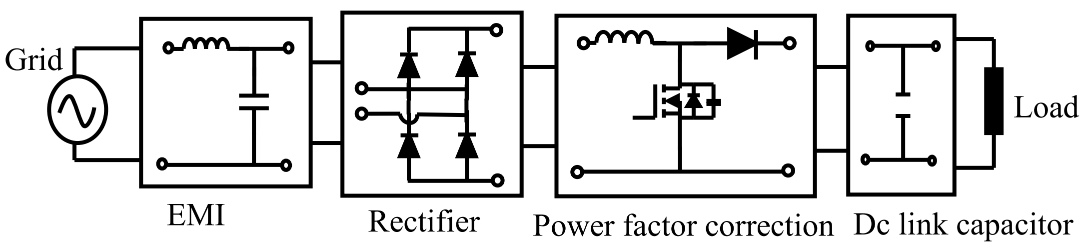

(a)

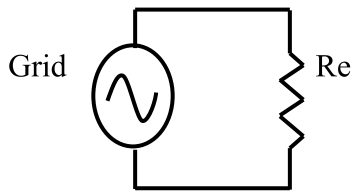

(b)

Figure 2. 2 (a) common block diagram of AC-DC PFC stage, (b) equivalent circuit.

The typical second stage isolated DC-DC converter consists of a switching network, high-frequency transformer, rectifier, and a low pass filter as shown in Figure 2.3. For frequency-modulated resonant converters, an additional resonant tank between the switching network and high frequency is required.

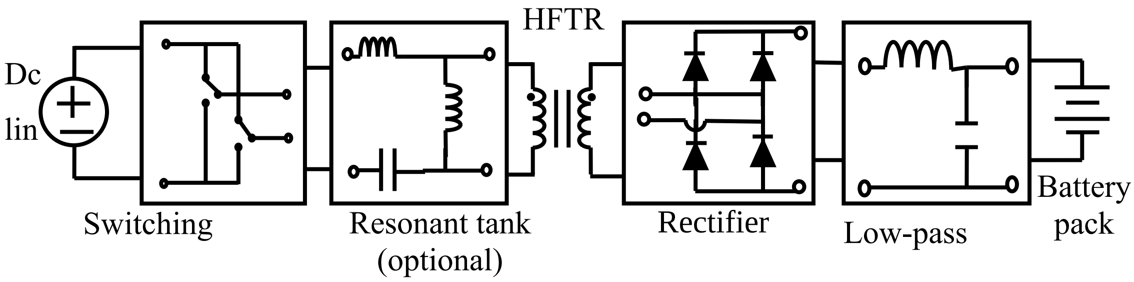

Figure 2. 3 Typical configurations of isolated dc/dc topology.

Four different switching networks are shown in Figure 2.4 With the same dc-link voltage and switch ratings, the RMS output voltage of full-bridge is twice of that of half-bridge configuration. Therefore, the full-bridge topology with the same switch ratings can be designed and utilized with two times higher output power capability. To achieve shorter charging time, a higher power level is always desirable for onboard battery chargers. Consequently, only full-bridge configurations are considered for this thesis.

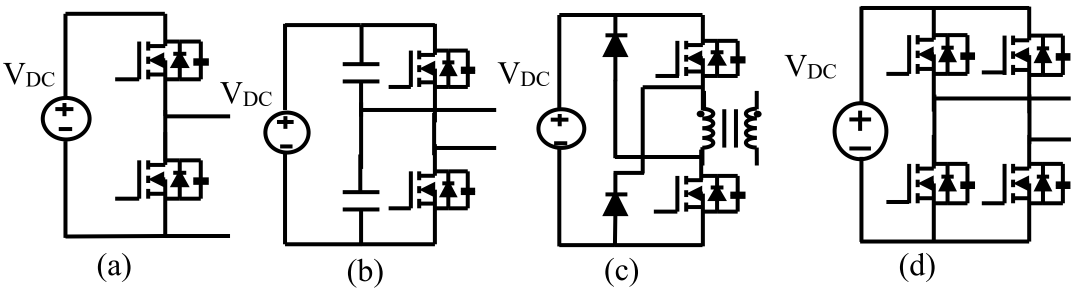

Figure 2. 4 Common switching networks, (a) half-bridge, (b) half-bridge with a split capacitor, (c) two-switch forward, (d) full-bridge [37]

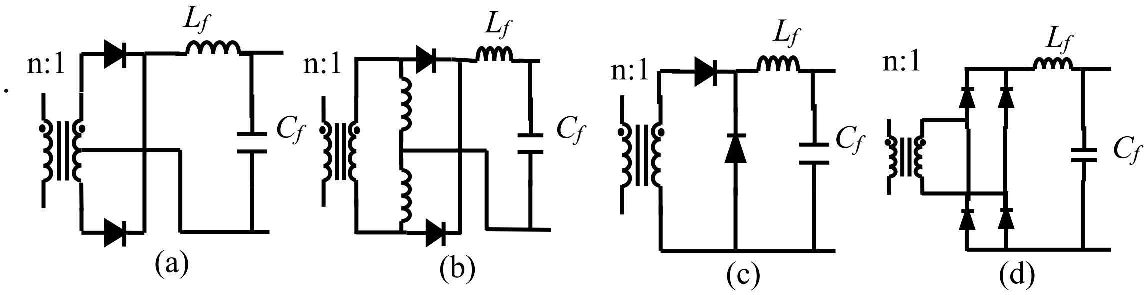

Figure 2. 5 Common rectifier networks, (a) center tapped rectifier, (b) current doubler rectifier, (c) half wave rectifier, (d) full bridge rectifier [36].

Four different rectifier networks are shown in Figure 2.5 Half wave rectifier only utilizes half of the input voltage cycle and does not provide a high-power density. The current doubler rectifier and center-tapped rectifier are more suitable for low voltage and high current applications, respectively. The voltage rating of rectifier diodes must be higher than twice the output voltage. However, onboard battery charging is associated with high battery pack voltage and relatively low charging current, where full bridge rectifier is more suitable. Consequently, only full-bridge rectifier configurations are considered in this thesis.

2.5.1. Challenges in Onboard Charger Design

To design a compact and highly efficient onboard charging interface, the following considerations must be taken into account:

- High switching frequency is desired to reduce the volume and weight;
- Both step-down and step-up operations should be realized to satisfy the wide output voltage range requirements;
- Zero-voltage-switching (ZVS) feature is desired to reduce the switching losses as well as high-frequency electro-magnetic interference (EMI);
- A high-frequency transformer must be integrated to achieve galvanic isolation without negotiating the size and weight;
- Conversion efficiency must be optimized across the full battery voltage ranges as well as different load conditions.

In high switching frequency applications, MOSFET is preferred due to its fast switching speed and no tail current. In hard switching topologies, higher switching frequencies would lead to high stress and high EMI noise. Thus, soft switching techniques, which include zero voltage switching (ZVS) and zero current switching (ZCS), are desired. For MOSFETs, ZVS is more suitable because operation with ZVS eliminates both body diodes reverse recovery and semiconductor output capacitances from inducing switching loss in MOSFETs [38]. However, the ZVS technique could lead to high circulating current and increased conduction losses. Moreover, in some specific topologies, such as phase shift full-bridge converter, even though ZVS operation is achievable in full loads. However, MOSFETs in the lagging leg might lose ZVS features in light load conditions.

Another encounter comes from the wide voltage variation of the high voltage battery pack in the EV. Corresponding to the depleted SOC and full SOC, the voltage of the battery pack varies from the cut off voltage to the charge voltage (e.g. 320V to 420V). This means the dc/dc conversion stage must be able to be adapted to this wide voltage range. The pulse-width-modulation (PWM) topologies have the advantages of easy regulation of the output voltage in a wide range. However, they also have the disadvantages of incomplete ZVS range. Frequency modulated resonant topologies have a full ZVS range. However, the efficiency of resonant topologies can be only optimized in some specific output voltage [39].

The typical circuit configuration of the onboard EV battery charger has two stages. The first stage is the front-end PFC circuit which maintains the power factor and reduces the input current ripple to minimize the total harmonic distortion. On the other hand, the back-end DC-DC converter which regulates the DC voltage to charge a high voltage propulsion battery of the EV. The following sections describe the comparison of converters in each stage.

2.6. Review of Front-end AC/DC PFC Topologies

The front-end ac/dc converter is a critical component of an EV charger. Proper selection of the topology is essential to meet the regulatory requirements for input current harmonics, output voltage regulation, and implementation of power factor correction.

Boost topology and its derivatives are broadly used for AC-DC power factor correction (PFC) purposes [40]. In comparison with operation in continuous conduction mode (CCM), a boost converter operating in discontinuous conduction mode (DCM) would have smaller switching losses. However, for high power levels, operation in DCM means large current stress to circuit components. Therefore, only CCM is considered for high power EV battery charging applications. There are various topologies in the PFC circuits when a device is connected to the AC power source. The following points show the insight view of each topology and its limitations.

2.6.1. Conventional Boost PFC Converter

Figure 2.6 shows the schematic of a single-phase boost PFC converter. A diode bridge is utilized to rectify the AC voltage from the grid to DC; a boost converter is followed to correct the power factor. In most applications, the conventional boost PFC is commonly used as it is simple to design. This topology has a few limitations in charging the battery packs for EVs is summarized as follows.

1. This topology has an efficient operation for low to medium power range, up to 1 kW. In high power levels, the high peak current of the inductor in DCM is associated with a bulky magnetic component. The circuit control and sensing the complexity level also increase.
2. The input diode bridge (D1-D4) degrades the performance of the converter when the power level increases since the reverse recovery time of the input diodes cause more heat dissipation over an area, which is problematic.
3. The only parasitic capacitance that contributes to CM noise is the drain-to-ground capacitance of MOSFET.
4. The volume of the inductor design also becomes problematic at high power levels.
5. The voltage stress on conventional boost devices is high.
6. The high-frequency operation makes the reverse recovery losses from the boost diode a big concern. The reverse recovery current of the diode (DF) during the turn-on of the MOSFET creates a sudden shoot-through in the output capacitor and causes more EMI in the circuit due to negative spikes in the diode current [41].

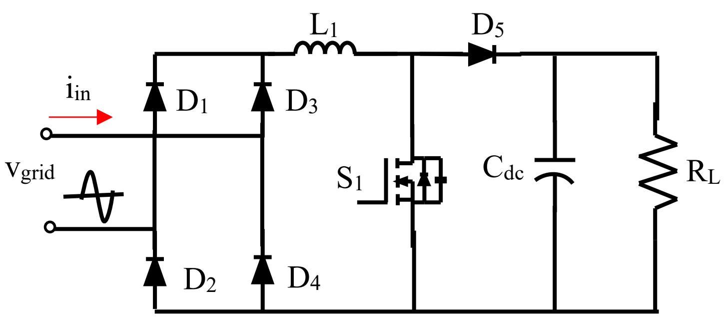

Figure 2. 6 Single-phase boost PFC converter [41].

2.6.2. Bridgeless Boost PFC Converter

Figure 2.7 shows the schematic of the bridgeless PFC boost converter. In comparison with conventional boost PFC converter, bridgeless topology gets rid of the diode bridge while keeping the boost feature. Consequently, the loss associated with the diode rectifier bridge is reduced, which makes it suitable to be applied to a higher power level. However,

1. Bridgeless configuration brings problems of high EMI [42] Besides,
2. The floating input line makes it impossible to sense the input voltage without a low-frequency transformer or an optical coupler. To sense the input current, a complex circuit is necessary to sense the current in the MOSFET and diode separately [43].
3. In a high-power level, the high peak current of the inductor is also associated with bulky magnetic components.

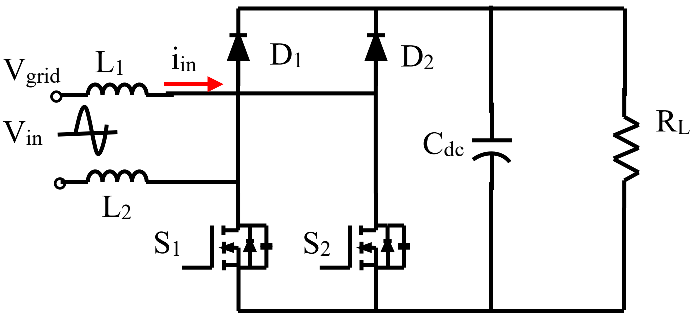

Figure 2. 7 Bridgeless PFC boost converter [43].

2.6.3. Interleaved Boost PFC Converter

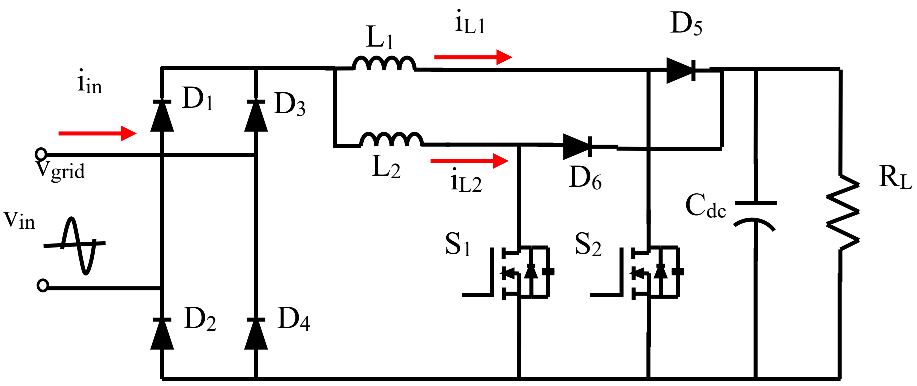

Figure 2. 8 Interleaved PFC boost converter.

Figure 2.8 shows the schematic of the interleaved PFC boost converter. In single-phase interleaved topology, two boost converters are in parallel and operated with a 180-degree phase difference. The input current equals the summation of both inductor current. Since the inductor ripple currents are the output of phase, they can cancel with each other. Thus, the high-frequency input current ripple could be significantly reduced, so that the size of the input EMI filter could be reduced [44]. Moreover, the power of the converter is evenly shared between those two boost legs, thus the current stress on the circuit components is reduced by half.

The performance comparison of those three different PFC topologies is summarized in Table 2.4. As shown in Table 2.4, interleaved boost PFC topology has the best overall performance in high power applications.

Table 2. 4 Comparison of AC-DC PFC topologies for EV battery charging [45]

Topology	Conventional boost	Bridgeless boost	Interleaved boost
Power level	Low	Medium	High
EMI/Noise	Fair	Poor	Best
Capacitor ripple	High	High	Low
Input current ripple	High	High	Low
Magnetic size	Large	Medium	Small
Efficiency	Poor	Good	Good
Cost	Low	Medium	Medium

2.7. Review of Second Stage Isolated DC-DC Topologies

Selecting the right second stage DC-DC converter is an additional vital subject in designing an electric vehicle charger. These converter topologies control the DC voltage following the battery voltage of the electric vehicle battery pack. The review of the second-stage isolated DC-DC converter is discussed as follows.

2.7.1. Full-bridge Isolated PWM Buck Converter

The schematic and the simulated waveforms of full-bridge isolated buck converter in EV battery charging application is shown in Figures 2.9 and Figure 2.10, respectively.

In this converter topology, it is easy to regulate the output voltage by controlling the duty cycle, d. The boost behavior required by the battery charger could be achieved by suitably designing the turns ratio of the transformer, n. In the light load condition, the converter could switch to a discontinuous conduction mode (DCM). In DCM mode, the MOSFETs are turned on at ZVS.

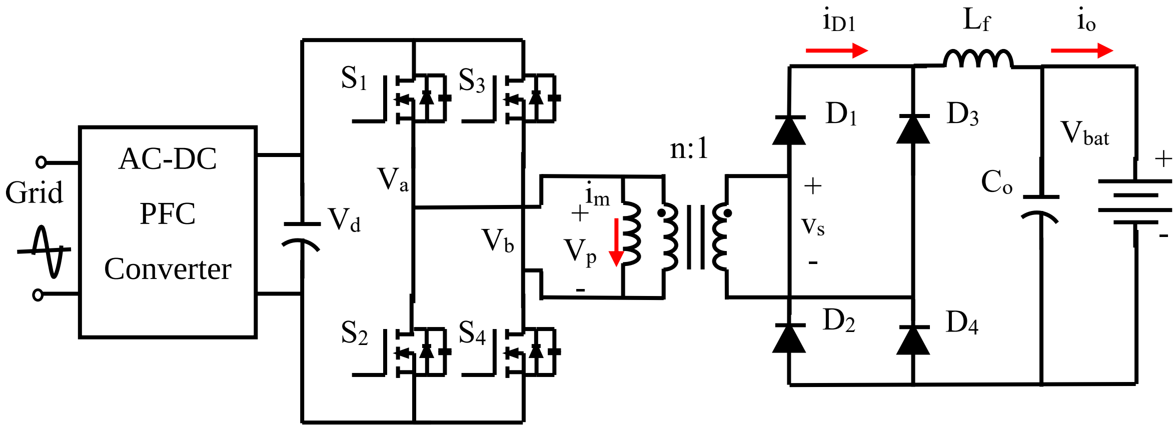

Figure 2. 9 Full bridge isolated PWM buck converter [46].

It should be noted that in CCM mode the MOSFETs of full-bridge isolated buck converter are turned on and off with hard switching. This causes significantly high switching losses and EMI problems, which greatly constrain the switching frequency. Moreover, in the time interval (DT_s, T_s], current in the magnetic inductor circulates in the primary side of the magnetic core. This causes high conduction losses [46].

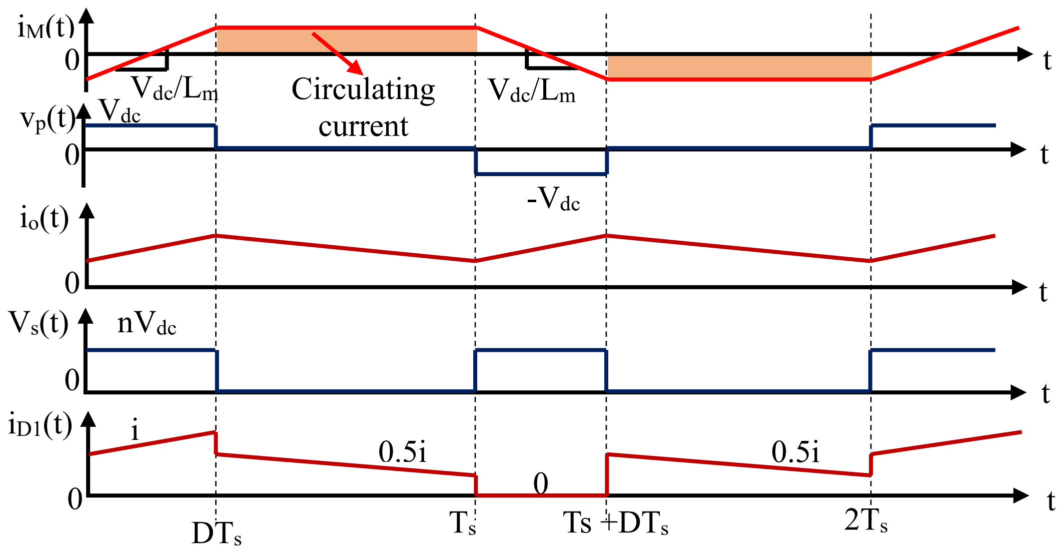

Figure 2. 10 Waveforms of the full-bridge isolated buck converter.

2.7.2. Full-bridge Phase-shift PWM Converter

Full bridge phase-shift converter is one of the most common topologies in the power range of a few kilowatts for isolated DC-DC conversion applications [47]. The schematic and simulated waveforms of the full-bridge phase-shift converter is shown in Figure 2.11 and

Figure 2.12, respectively. In the full-bridge phase-shift converter, the primary side MOSFETs are turned on with ZVS; and the body diodes are turned off with ZCS. The output voltage is regulated by the duty cycle and is easy to control. Besides, control of full-bridge phase-shift topology is easy to implement in comparison with its PFM resonant counterpart [48].

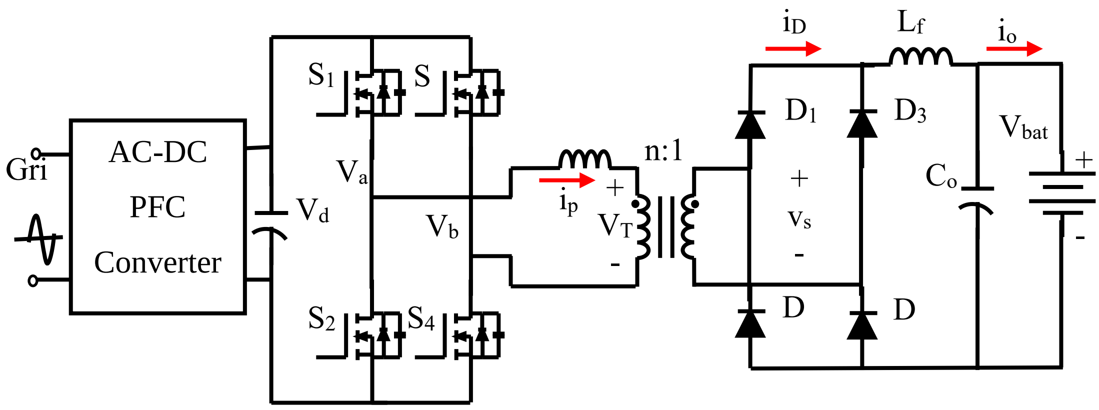

Figure 2. 11 Full bridge phase-shift PWM converter.

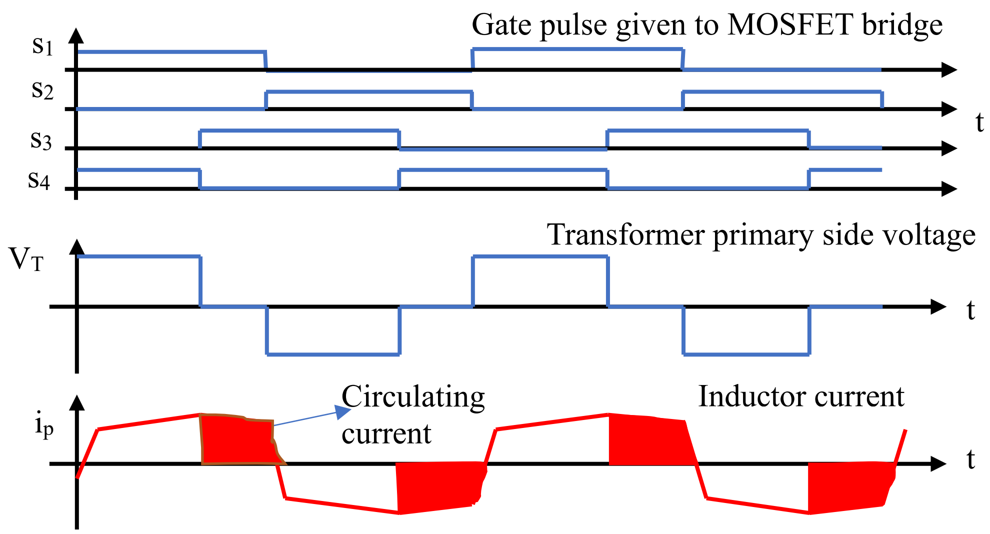

Figure 2. 12 Waveforms of the full-bridge phase-shift converter.

However, in EV battery charging applications, the output power range is wide. In the light load condition, limited energy is stored in L_r. This makes the MOSFETs in the lagging leg lose ZVS features [48]. Moreover, in the time intervals when either both upper switches are on or both lower switches are on, the circulating power is high and would cause higher conduction losses. Besides, the turning off of secondary diodes would cause high voltage overshoots and oscillations due to the high voltage of the battery pack.

2.7.3. Full-bridge Series Resonant Converter

Full bridge series resonant converter (FB-SRC) is another candidate for isolated dc/dc conversion [49]. The schematic of the full-bridge series resonant converter is shown in Figure 2.13. With the switching frequency higher than the resonant frequency of L_r and C_r, the primary side power MOSFETs are turned on with ZVS, and freewheeling diodes are turned off with ZCS. This ZVS feature is irreverent to different load conditions. One of the most attractive features of FB-SRC is that its circulating losses are very low. Moreover, FB-SRC has good short circuit protection performances; short circuit current could be easily regulated by boosting the switching frequency [50].

However, the critical defect of FB-SRC lies in its unacceptable poor voltage regulation performance in light load conditions. Slight perturbation from input voltage causes a large scale of frequency shift. This makes it hard to regulate the voltage and increases the switching losses and conduction losses. Moreover, secondary-side diodes are turned off with very high *di/dt*, which corresponds to big reverse recovery losses.

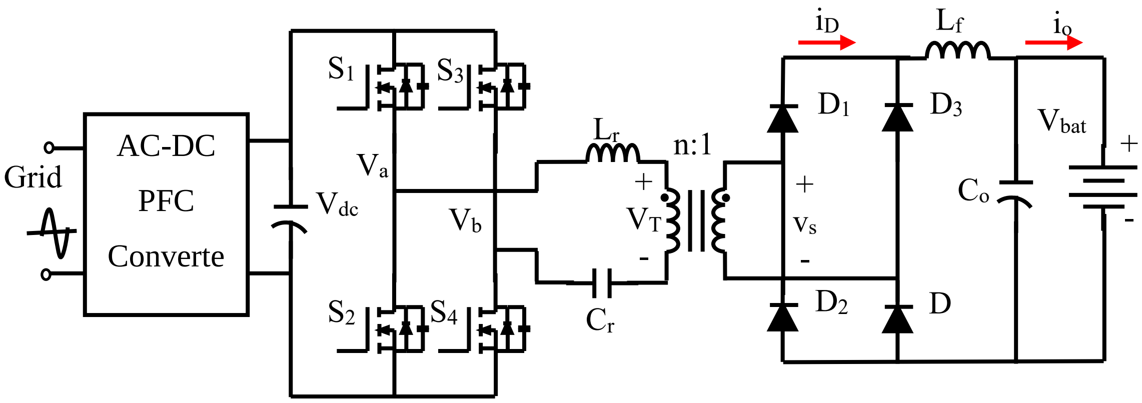

Figure 2. 13 Full bridge SRC PFM converter [49].

2.7.4. Full Bridge LLC Resonant Converter

Full bridge LLC resonant converter shown in Figure 2.14 has been proved to be one of the most suitable candidates for DC-DC conversion in applications, which require constant output voltage. When the input impedance is inductive, turning on of primary MOSFETs and turning off of freewheeling didoes are ZVS and ZCS, respectively. When the switching frequency is smaller than primary resonant frequency (f_p), which is the resonant frequency of L_r and C_r, secondary-side diodes are turned off with ZCS [51]. When switching frequency is smaller than f_p, and the input impedance is still inductive, circulating losses of FB-LLC are higher than FB-SRC. The short circuit performance of LLC is not as good as

FB-SRC but still acceptable [52].

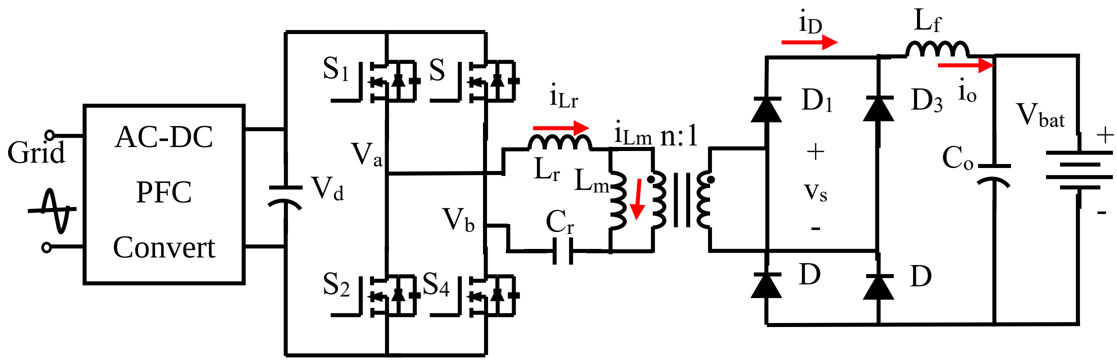

Figure 2. 14 Full bridge LLC PFM converter [51].

The performances of FB-Buck, FB-FS, FB-SRC, and FB-LLC topologies are summarized in Table 2.6.

Table 2. 5 Comparison of isolated DC-DC converters in EV charging applications

Performance	Full-bridge isolated buck	Full-bridge phase shifted	Full-bridge series resonant	Full-bridge LLC resonant
Modulation method	PWM	PWM	PFM	PFM
Additional filter inductor on the secondary side	Yes	No	No	No
Short circuit protection performance	Bad	Bad	Good	Good
Primary MOSFETs switching losses in normal load	High, hard switching	Low, ZVS	Low, ZVS	Low, ZVS
Secondary diode switching loss in normal load	High, hard switching	Low, ZCS	High, hard switching	Low, ZCS
Harmonic distortion in normal load	High	Low	Low	Low
Light load circulating losses	Low	High	Low	Moderate
Light load switching losses	Low	High, ZVS feature lost	Low	Low
Voltage regulation capability at light load	Good	Good	Poor	Good

2.8. Lithium-ion Battery Management System

Lithium-Ion is a low maintenance battery, an advantage that most other chemistries cannot claim. This Lithium-Ion battery is the best alternative source of energy storage for Electric Vehicle (EV). Even though this Lithium-Ion battery pack has a lot of advantages and get more popular lately, but there are problems due to the price of the Lithium-ion battery pack are too expensive nowadays. Thus, the Lithium-ion battery could ignite if overcharged. This is a serious problem, especially in EV applications, because an explosion could cause a deadly accident. Moreover, over-discharge causes reduced cell capacity due to irreversible chemical reactions. Therefore, a BMS needs to monitor and control the battery charging system based on the safety circuitry incorporated within the battery packs. Whenever any abnormal conditions, such as over-voltage or overheating, are detected, the BMS should notify the user and execute the preset correction procedure.

In addition to these functions, the BMS also monitors the system temperature to provide a better power consumption scheme and communicates with individual components and operators. In other words, a comprehensive BMS should include the following functions; data acquisition, safety protection, ability to determine and predict the state of the battery, ability to control battery charging and discharging, cell balancing, thermal management, delivery of battery status, and authentication to a user interface, communication with all battery components. Figure 2.15 shows the schematic diagram of a typical BMS.

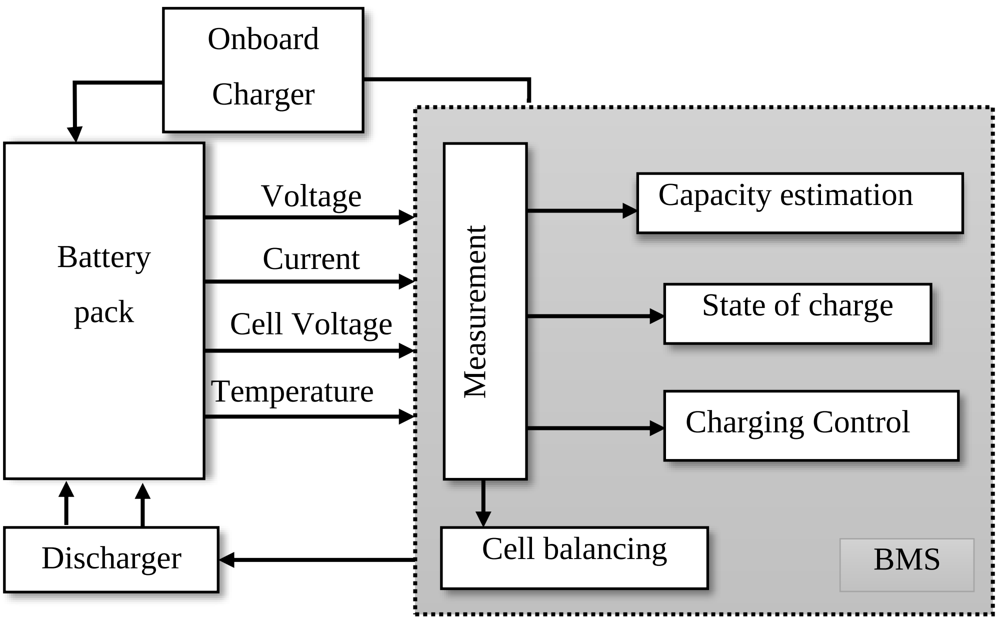

Figure 2. 15 Schematic diagrams of a typical BMS

2.8.1. Basic Functions of the Battery Management System

The main functions of the BMS include state monitoring, safety protection, charging control, state of charge estimation, battery cell equalization, thermal management, etc.

2.8.1.1. Battery Cell Monitoring

The battery is a complex and nonlinear time-varying system with multiple states that change in real-time. Accurate monitoring of the battery state is the key to the battery cell and its system management, which is also the basis for management and control of the EVs electric vehicle charging system. It indicates the necessity of the charge control, the protections from the overcharged conditions, the control of the temperature by providing information on current, voltage, temperature, etc. in real-time conditions. And that plays a vital role in facilitating the early failure detections in electric vehicle batteries [53].

The abnormal change in the battery current and voltage values may cause system failure or system burnout. Thus, the monitoring of the current and voltage levels of battery cells is essential for protecting the cells from the over-current/voltage and under-current/voltage operations [54]. Also, the records of the current and voltage values present the status of the energy storage system so that the BMS can decide for further action.

2.8.1.2. Charging Control

Developing a genuine battery charging method is another essential function of the BMS. The method is based on accurate battery estimations for the state of charge (SOC) and temperature. The proper battery charging approach facilitates efficient battery charging from the initial to the final SOC battery state, as well as protect the battery from overheating, prolonging its life span, and improving capacity utilization.

The effective charging and discharging controls remove the memory effect and boost the discharging period of the battery. It is recommended to charge the Li-ion battery by the CC-CV (constant current- constant voltage) charging algorithm [55]. In this case CC-CV charging is used for this thesis.

2.8.1.3. State of Charge Estimation

Estimating a battery's state of charge provides a fuel gauge to the load device that indicates the amount of charge (coulombs) which currently can be discharged from the battery divided by the total charge of the battery in its fully charged state. For the load device, it is useful to know the state of charge (SOC) to provide the user with feedback (estimated remaining run time in a backup power system, or driving range in an electric vehicle), but it is also critical for the battery management system and the battery system itself as several other battery parameters depend upon the SOC.

Typical methods for SOC estimation include ampere-hour (AH) counting (e.g., Coulomb counting), inverse nonlinear mapping from the open-circuit voltage (OCV) to the SOC, the Kalman filter (KF) [56] and its extensions [57], [e.g., the extended KF (EKF) and unscented KF (UKF)], artificial neural network (NN)-based methods [58], and fuzzy logic-based methods [59]. Because the KF cannot be used directly for state prediction of a nonlinear system, the EKF- [57], and UKF-based methods [60] are the most widely used. However, the EKF must compute the Jacobian matrix and is generally not suitable for highly nonlinear systems with non-Gaussian noise. Similar to the EKF, the UKF is another extension of the KF and is also a recursive minimum mean square error (MMSE) estimator. The UKF outperforms the KF and EKF in terms of accuracy and robustness for nonlinear estimation. The UKF does not need to calculate the Jacobian matrix and does not require noise to be Gaussian, which makes it more appealing for SOC estimation because battery systems are highly nonlinear and the noise properties are typically not known. So in this thesis, the unscented Kalman filter is used to determine the state of charge of the lithium-ion battery cell.

2.8.1.4. Battery Cell Voltage Equalization

Cycling a battery pack eventually causes individual cells to become out of balance. Different columbic efficiency across the cells is one typical cause of this problem which manifests itself as the difference in soc level among cells. This situation is undesirable because it limits the total amount of energy that enters or exits the battery pack. Since the weakest cell limits, the amount of charge that can be drawn from the entire system and the strongest cell limits the extent to which the system can be charged.

Typically balancing is done in either of two ways. Using a dissipative method is commonly referred to as passive balancing in which the excess charge from the cells at the top bleeds through the resistors connected in parallel with each cell. Another balancing method is a non-dissipative method commonly called active balancing in which the excess charge from some cells is redistributed among other cells that require it [61].

The active cell balancing technique equalizes variations among cells in series by moving electrical energy from higher SOC cells to lower SOC cells with little loss. When the charge of one cell is higher than the average charges of the balancing module, the cell will have no option but to be deprived of the extra charges which are moved to the cell with fewer charges. This method is very efficient because the excess energy is transferred to the cell with low energy instead of being precipitated away, but it increases balancing circuit complexity [62]. But controlling the system is very complex and costly.

The passive cell balancing method is relatively simple compared to the active cell balancing method., The conventional cell balancing approaches are passive where the excess charge of cells with high SOC is dissipated as heat across a resistor [63], resulting in reduced energy efficiency. However, this method is good for low-cost system applications in which no active control is utilized to equalize. In this method, the resistor is placed in parallel with each cell and the resistor size determines the balance rate. There are two types of passive cell balancing topologies. They include the fixed shunting resistor and switched the shunting resistor [64]. The intent is simply to discharge the cells at higher SOCs (or higher remaining charge) to match the rest of the cells. Passive balancing is still the dominant method in use today. For this thesis work passive balancing with switched resister is used to balance cells.

2.9. Related Electric Vehicle OBC Topologies

Due to the identified trends in EVs regarding increased battery capacity and hence increased OBC power rating, OBC converter topologies strictly level-2 OBC will be identified and analyzed in this section, coming from both industries as well as research environments.

2.9.1. Industry Established Charging Solutions

Currently, at least three suppliers offer high-power OBC solutions that can be designated as the industry state of the art. The following information was found using available primary online resources, and thus this list may be incomplete, as many companies and EV manufacturers do not release their OBC information because of competitive privacy reasons.

1. Brusa [L2]: Brusa offers the NLG664 and NLG667 on-board chargers, which are both liquid-cooled and compatible with up to 7 kW single-phase and 22 kW three-phase.

They achieve three-phase efficiency of over 94% and single-phase efficiency of over 90%, with 1.83 kW/kg specific power, and 1.82 kW/L power density. The chargers utilize conventional Si switching devices. Those chargers have an extremely high cost. The charger cost £4,017.60.

2. G-Power [L3]: The G-Power OBC can operate as either a 10 kW three-phase charger, or a 6.6 kW single-phase charger. The OBC achieves 94% efficiency, and a 0.52 kW/L power density. Furthermore, the charger is air-cooled, which is likely the main contributor to its large volume.
3. Continental [L4]: The Continental OBC is a single- and three-phase compatible charger supporting power levels up to 22 kW. A detailed datasheet including Figures for peak converter efficiency, power density, and weight is not available at this time.

Discussion: Each of these industry-level chargers is capable of operating over a wide input voltage range and variable grid frequency. The benefit of the wide input voltage and grid frequency ranges is that the charge is compatible with the global EV market and EVSE units. Furthermore, each charger is capable of a wide output voltage range variation to charge the EV’s propulsion battery throughout the full state-of-charge profile. The above section gives industry level chargers. Technical design and the circuit configuration are not available due to security and patent issues. Finally, in terms of efficiency, power density, and specific power, none of the presented commercially available OBCs meet the U.S. Drive Partnership’s 2020 targets [65], illustrating the need for increased research and development.

2.9.2. OBCs in Research Environment

Several non-integrate high-power OBC topologies and their associated control algorithms have been researched in the literature. OBC is a unique component inside the EV that interfaces the charging input and provides conditioned output power to the high voltage propulsion battery. The typical structure of a nonintegrated OBC includes an electromagnetic interference (EMI) filter, an AC-DC PFC, a DC link, and an isolated DC-DC converter.

One of the primary difficulties in high-power OBCs is balancing efficiency, cost, size, reliability, and weight. Efficiency and cost considerations are particularly important at higher power levels because the current-related conduction losses may be high, and thus paralleled switching devices may be required. The presented strategies each approaches this issue in different ways. While most of these topologies are two-stage, several single-stage topologies are also identified. Single-stage topologies may be advantageous to meet stringent power density requirements posed by auto manufacturer's targets. In addition to that saving weight, reducing cost, and enhancing reliability with the removal of the electrolytic DC link capacitor [66]. But single-stage battery chargers have high stress on components and have high EMI. This section provides a review of high power non-integrated OBCs available in the literature, to the best knowledge of the authors at the time of authorship.

The authors in [67] proposed circuit topology of a charger that is designed for a single-phase module of the three-phase charger. While this converter is rated for 10.5 kW, it utilizes three parallel single-phase charging modules each rated for an equal distribution of full power, at 3.5 kW. Each single-phase charger is composed of a diode bridge and a boost converter operating at 90 kHz switching frequency, connected to a DC link. The DC-DC stage for each single-phase unit is an isolated half-bridge LLC resonant converter, with a diode bridge at the secondary side. The half-bridge LLC converter is operated using frequency modulation with a switching frequency range between 90 kHz-275 kHz. There is a single input filter with a high EMI filtering requirement from each of the three single-phase converters. While the burden on the input and output filters is high, there are no duplicate filtering elements in the circuit as compared to having filters for each phase.

It is reported that the converter achieves an efficiency of 95.6% and a power density of 1.75 kW/L. An advantage of this design is modular power processing, zero-voltage switching (ZVS) capabilities in the half-bridge LLC switches, and reduced system complexity with the PFC input and LLC secondary side diode bridges. In addition to that, the charger uses SiC diode to construct a rectifier bridge due to its very low reverse recovery current. Disadvantages include unidirectional power flow, since boost converter is used as a PFC stage converter it needs to have a high EMI filter design. This makes the charger have a large volume. And also, the converter has a bulky capacitor to filter voltage ripple in the dc-link stage. The converter uses a half-bridge LLC converter this makes the charger have component stress.

The authors in [68] proposed circuit topology of a charger that is designed for a single-phase module of a three-phase converter. This charger is designed for 22 kW and is composed of three single-phase 7.2 kW units. Each single-phase unit is comprised of a full-bridge switch network, which is operated as a full-wave rectifier. This leads to a rectified AC voltage across the AC link capacitor bank. Since the AC link capacitor is not an energy storage capacitor, the topology is designated a single-stage solution. Following the AC link in each single-phase unit is an isolated full-bridge dual-active-bridge (DAB) DC-DC converter.

With the front-end full-bridge only offering rectification, the DAB converter is therefore responsible for shaping the input current to achieve PFC action. In this case, a secondary side dual-phase-shift (SDPS) control strategy is developed, which can shape the input current accurately as well as offer ZVS on every switch. When the battery voltage is low, a primary-side dual phase-shift (PDPS) control strategy is utilized to ensure ZVS operation and reduce DC-DC converter MOSFET current stress. The converter has a complex control method since a dual active bridge is used for both power factor correction and dc voltage regulation. The converter also uses a large number of active switches which leads to higher losses.

In comparison to [69], where a direct matrix converter is used to directly convert single-phase AC to DC, the converter topology is similar to [68]. The downside of the structure in [69] is the necessity of bidirectional switches to accommodate the positive and negative half cycles of the input voltage. This doubles the switch and driving circuit count where expensive GaN devices are required in parallel for thermal and loss considerations. Since the front-end rectifying bridge switches at mains frequency, conventional Si MOSFETs are suitable because the only important switch characteristic is the on-state resistance. One area of concern in the proposed charging system is the high source and sink characteristics of the AC link, however, this AC link capacitor bank can be realized with a much smaller form factor than its DC link counterpart.

Additionally, the authors constructed a SiC prototype and drew comparisons between the two emerging wide bandgaps (WBG) technologies in [70]. It was concluded that the GaN prototype exceeded its SiC counterpart in the categories of efficiency, power density, and projected 2020 cost. It is reported that the charger achieves a peak efficiency of over 97% and a power density of 3.3 kW/L. The advantages of this design include no DC link capacitor, very high-power density, and high converter efficiency. Disadvantages of the charging system include the addition of active components for single-phase implementation, high cost of GaN components at the current price levels, and complex control implementation.

The authors in [71] proposed circuit topology of a charger that is designed for a 10-kW power rating utilizing a three-phase input connection. The charging unit is comprised of a three-phase boost PFC connected to a DC link capacitor, followed by an isolated LLC resonant DC-DC converter with half-bridge structure at the primary side, and a full-bridge topology on the secondary side. The charging unit also has an additional input connection to the DC link from a boost converter that connects to a solar panel input.

While the authors do not mention the control technique for the three-phase boost PFC, several related documents regarding control with a single DC link voltage sensor, duty cycle compensation, and a soft-switching strategy can be found in [72] [73]. On the other hand, the half-bridge LLC resonant converter is controlled using typical frequency modulation, with the switching frequency varying between 90 kHz-150 kHz. One desirable control capability of the front-end PFC is a variable DC link voltage control to maximize the efficiency of the cascaded DC-DC converter.

It is reported that the converter achieves an efficiency of 96%. But, numbers for power density and weight were not provided. An advantage of this design is reduced system complexity for high-power compatibility, bidirectional power flow due to the active front end and DC-DC secondary sides, and comparatively high efficiency. However, disadvantages lie in the high RMS currents of the half-bridge LLC, reliability due to higher stress on resonant capacitors, high EMI filter requirement due to the active front-end PFC and loss related to diode bridge.

The authors in [74] proposed circuit topology of a charger that is designed for a 20-kW power rating with a three-phase input. It is comprised of a three-phase boost PFC connected to a DC link capacitor, followed by two parallel-connected isolated half-bridge LLC resonant DC-DC converters, with two high-frequency transformers (HFT) connected in series-star configuration, and two parallel secondary side diode bridges. The two HFTs, connected in series-star configuration, are significant to ensure equal current flow between the primary sides of the two DC-DC converters, mitigating resonant component discrepancies between the two converters. By utilizing a relay on the star points, the circuit could be reconfigured to operate without the second DC-DC converter unit in lower power modes.

The PFC and DC-DC converters are independently controlled by respective DSPs. The three-phase boost PFC is controlled with discontinuous pulse width modulation (DPWM) in combination with a direct-quadrature (DQ) reference frame current loop and an outer DC bus voltage loop, both supplied with reference signals by a phase-lock loop (PLL). The DPWM control strategy is utilized over the traditional space vector pulse width modulation (SVPWM) technique to achieve a higher DC link voltage of over 600 V and reduce switching loss, at the cost of increased conduction loss. Additionally, variable DC link voltage control is utilized to achieve maximum efficiency through the isolated DC-DC converters.

On the other hand, the half-bridge LLC utilizes traditional frequency modulation to fulfill the output voltage and current requests from the vehicle's BMS. A 180-degree phase shift is incorporated between the two primary side half-bridges to simplify the current loop control to a single PI loop.

Finally, the secondary side diode bridges can be reconfigured from a parallel to a series connection to realize an output voltage range from 400 V_{DC} to 900 V_{DC}. One important consideration that is neglected in this study is the size, weight, volume, and efficiency contributions from the input EMI filter. Comprehensive design approaches and optimization for both common-mode (CM) and differential-mode (DM) filters in the three-phase boost PFC have been systematically evaluated in [75], [76]. The EMI filter is particularly significant in the three-phase boost PFC as there is an inherent requirement for attenuation of high-frequency CM components [75]. Additionally, DM filter optimization can lead to a compact and lightweight contribution of the filter to the overall system, which is addressed in [75] and [76].

It is reported that the converter achieves an efficiency of 96%; however, power density and weight numbers were not provided. Advantages of the converter include flexible output voltage range capabilities, accurate current sharing with star connection between the two transformers, and high-power processing at reasonably high efficiency (although the efficiency measurements are not given the authors mention a peak larger than 96%). Disadvantages include potentially high RMS currents at 20 kW through the half-bridge

LLC primary side, reliability concerns in the DC link and resonant capacitors, and unidirectional power flow due to the use of secondary side diode bridges. Bidirectionality could be achieved using secondary side full-bridge MOSFETs at the cost of increased system complexity.

In conclusion, most of the above discussed onboard electric vehicle chargers uses conventional boost converter for front end PFC circuit and half-bridge LLC converter to regulate the dc-link voltage to battery voltage. However, the boost converter has high input current ripple that needs a larger magnetic size filter that makes the charger to be big. Using half-bridge LLC converter makes the converter to highly stressed and to have large RMS current. In addition to it, the above-discussed chargers don’t give any clue about the charging algorithm that charger charges the battery, how it is managed, and how it integrates with the battery using the battery management system.

This thesis uses interleaved boost converter and full-bridge LLC resonant converters to design an onboard battery charger. Also, a battery management system is developed to manage the charging algorithm. This will improve the problems discussed above.

CHAPTER 3

METHODOLOGY

3.1. Introduction

This chapter includes data analysis, mathematical modeling, design, and comparison of parts of isolated interleaved boost- LLC resonant dc-dc converter based onboard lithium-ion battery charger and battery management system that closely related to charging the battery pack is set up in MATLAB. Analysis of identified topologies is performed. Then modeling of the overall charging system is performed. Finally, the system is simulated by using MATLAB software.

3.2. Methods

The following method is used to study the specific objectives of the proposed system. First, closely related works are reviewed. Then the necessary data used throughout this study is collected. The specification of the charging system and battery is taken from the ECADO-4EV center of Excellency. Additional information is obtained from other related electric vehicles on the internet. The collected data are analyzed for understanding and developing system modeling.

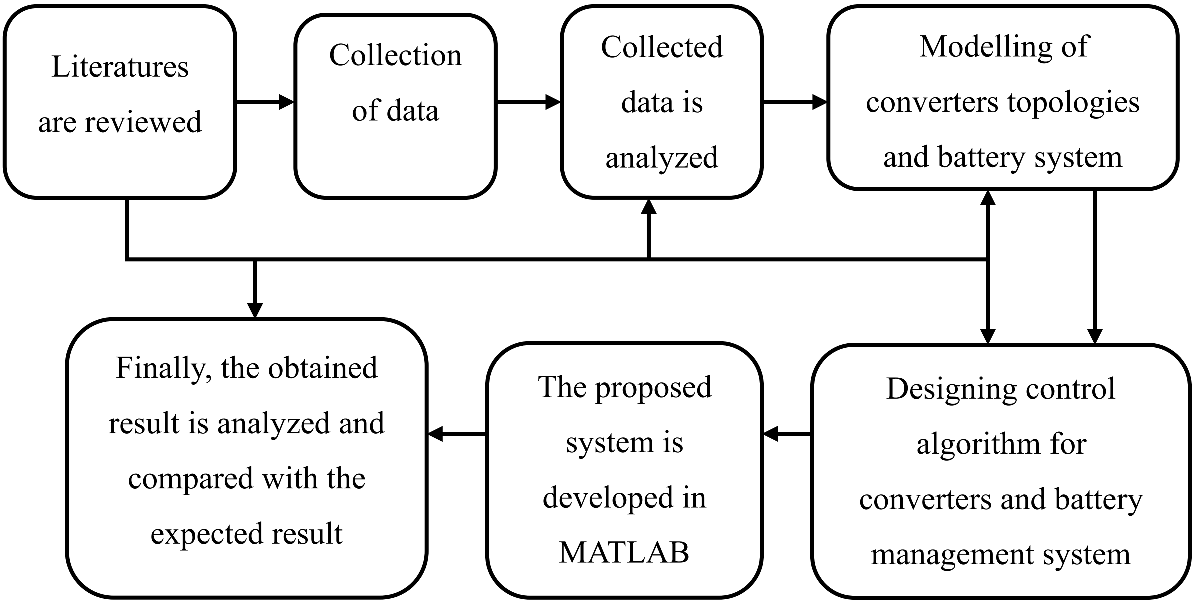

Figure 3. 1 Block diagram of the research methodology

The modeling of isolated interleaved boost and LLC resonant based onboard lithium-ion battery charger is developed. Then the system is simulated by using MATLAB/Simulink /Simscape/code. The result of the simulation is compared with expected output. In general, the method followed throughout the research study can be summarized as the following flow chart of Figure 3.1.

3.3. Block Diagram of the Proposed System

High power density, high conversion efficiency, high power factor, and low THD are the desired features expected from onboard electric vehicle (EV) battery chargers [77]. Figure 3.2 shows the general power electronics architecture of a typical onboard EV battery charger. The system consists of a front-end ac/dc converter used for rectification at unity power factor, and a second stage dc/dc converter responsible for battery voltage regulation and providing galvanic isolation.

The boost converter is the common front-end PFC interface due to its simple structure, good THD reduction performance, and unity power factor operation capability [78]. However, the volume of the converter tends to increase with the increase of charging power. Moreover, high root mean square (RMS) current in the dc-link capacitors would generate high power loss and significantly reduce the capacitor's lifetime, leading to capacitor failures.

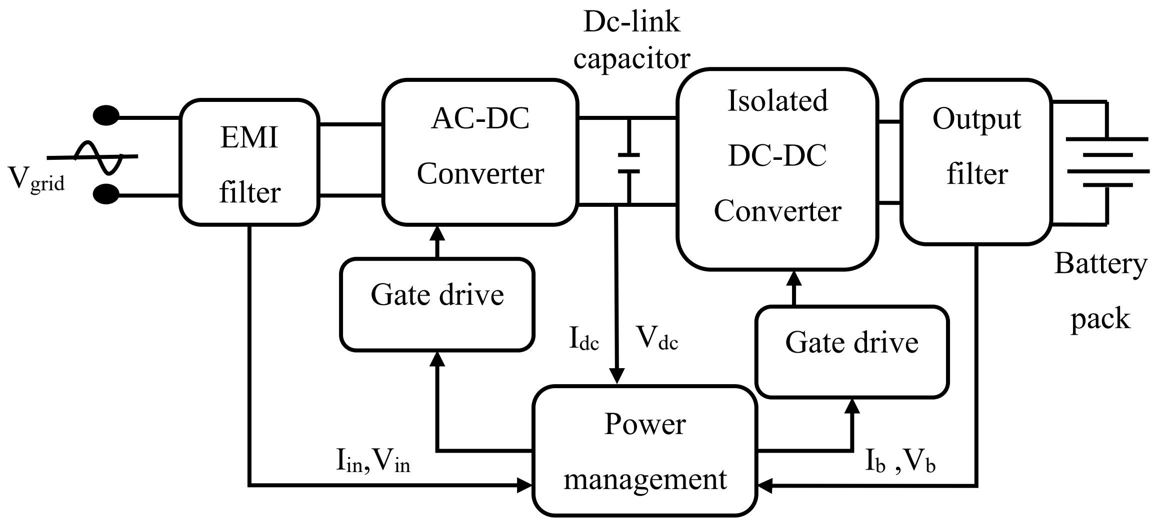

Figure 3. 2 General system architecture of a battery charger

Also, the required inductance value to reduce the ripples in the input current for better THD performance, would considerably increase as the charging power increase. This results in a large volume inductor core and wire size. In comparison with single-phase boost PFC converter, the interleaved boost topology has the benefits of reduced overall volume and improved power density [79].

In the DC/DC isolation stage, resonant converters are preferable at high voltage and high power EV battery charging applications. In particular, multi-resonance based LLC topology has several advantages over other resonant topologies, such as good voltage regulation performance at light load condition, the ability to operate with zero voltage switching (ZVS) over wide load ranges, no diode reverse recovery losses through soft commutation, the low voltage stress on the output diodes, and having only a capacitor as the output filter compared to the conventional LC filters [80].

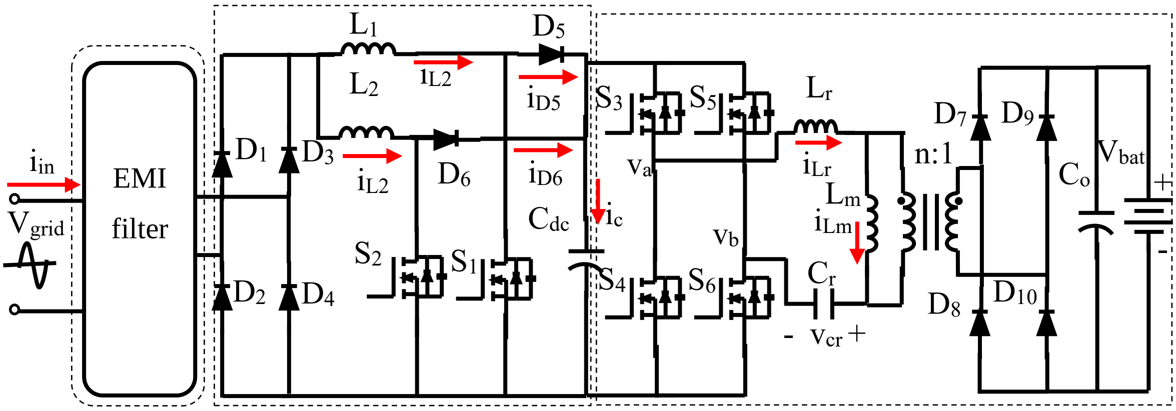

Figure 3. 3 Schematic of proposed level 2 onboard charger.

Despite these advantages, operating the circuit at the maximum efficiency considering the conduction and switching losses over the full output voltage ranges remains a challenging issue, as the battery voltage varies in a wide range depending on the different state-of-charge (SOC) [81], [82]. In this work, an onboard EV charger topology consisting of an interleaved boost PFC rectifier followed by an LLC multi-resonant dc/dc converter is designed as shown in Figure 3.3.

Both the interleaved boost PFC and the full-bridge LLC stages are extendible to much higher power levels with high power density and conversion efficiency. The proposed charger design is optimized for a wide voltage range (320V-420V) in a Lithium-ion battery pack. Moreover, the optimum design of LLC magnetic components, to achieve the maximum overall efficiency, is addressed in detail.

3.4. General Boost Converter

As shown in Figure 3.4, a general boost converter consists of an inductor *L*, a switch *S*, a diode *D*, and a filter capacitor *C*. The switch is turned on and off periodically with the period equals to *T*. The waveforms of the boost converter are plotted in Figure 3.5.

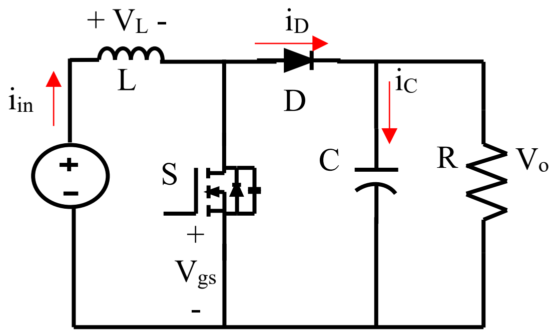

Figure 3. 4 Schematic of the general boost converter.

In (0, *dT*], the switch is on while the diode is off; the voltage across the inductor is the input voltage (V_{in}). In (*dT*, T], the switch is off while the diode is on; the voltage across the inductor is the input voltage subtracts output voltage (V_{in}-V_o). According to the volt-second balance of inductor, the average voltage applied to the inductor during one switching period is zero as shown in Equation (3.1).

$$dV_{in} + (1 - d)(V_{in} - V_o) = 0 \tag{3.1}$$

According to Equation (3.1), the relationship between the input voltage and output voltage could be calculated as Equation (3.2),

$$V_o = {}^{V_{in}}\!/_{(1 - d)} \tag{3.2}$$

According to the principle of energy conservation, the power input equals the power delivered to the load.

$$V_{in} I_{in} = V_o I_0 \tag{3.3}$$

where I and I_o are the average values of input and output currents.

From Equations (3.2) and (3.3), the relationship between input and output current is calculated as Equation (3.4).

$$I_o = {}^{I_{in}}/_{(1-d)} \tag{3.4}$$

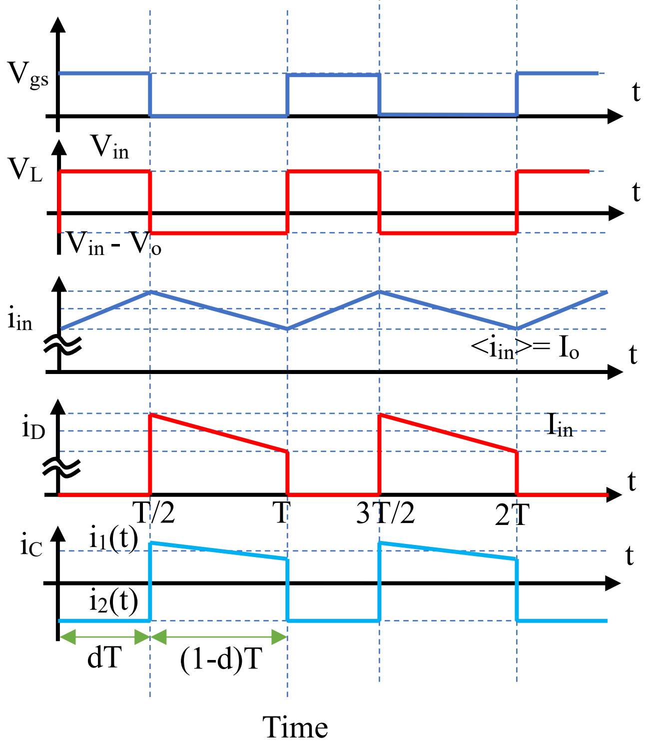

Figure 3. 5 Simulated waveforms of the conventional boost converter.

In (0, dT], the input current increases at the speed of V_{in}/L. Thus, the input current ripple is calculated as shown in Equation (3.5),

$$\Delta I_{in} = i_{max} - i_{min} = dT\frac{V_{in}}{L} \tag{3.5}$$

For a single-phase boost converter, the input current (i_{in}) equals the inductor current (i_L). Thus, the ripple current ratio [$K(d)$], which is defined to be the ratio between i_{in} *and* i_L, always equals to 1, as indicated in Equation (3.6).

$$K(d) = \frac{i_{in}}{i_L} = 1 \tag{3.6}$$

Since the switching period is very small (usually smaller than 20 μs), the input current in each switching cycle could be approximated as a constant. Thus, the capacitor's current ripple could be looked like a square wave. The envelope of the capacitor square wave is calculated as Equations (3.7) and (3.8),

$$i_1(t) = i_{in}(t) - i_o(t) = i_{in}(t)dt \tag{3.7}$$

$$i_2(t) = -i_o(t) = -i_{in}(t)[1 - d(t)] \tag{3.8}$$

For a single-phase boost converter, the RMS capacitor current can be calculated as Equation (3.9),

$$i_{c,rms}(t) = \sqrt{i_2(t)^2 d(t) + i_1(t)^2[1 - d(t)]} \tag{3.9}$$

Substituting Equations (3.7) and (3.8) into Equation (3.9), the normalized output capacitor RMS current $i_{rms,1}/i_{in}$ can be obtained as,

$$i_{c,rms}(t) \Big/ i_{in}(t) = \sqrt{d(t) - d(t)^2} \tag{3.10}$$

3.5. Interleaved Boost Converter

An interleaved converter is simply a multi-leg converter, each leg operating 360°/*n* out of phase, where *n* denotes the number of phases. A two-leg interleaved boost converter, whose interleaving legs are operated with 180° phase difference, is shown in Figure 3.6. The control of the interleaved converters is based on shifting the phase of S_1 with respect to S_2 such that the ripples cancel out each other.

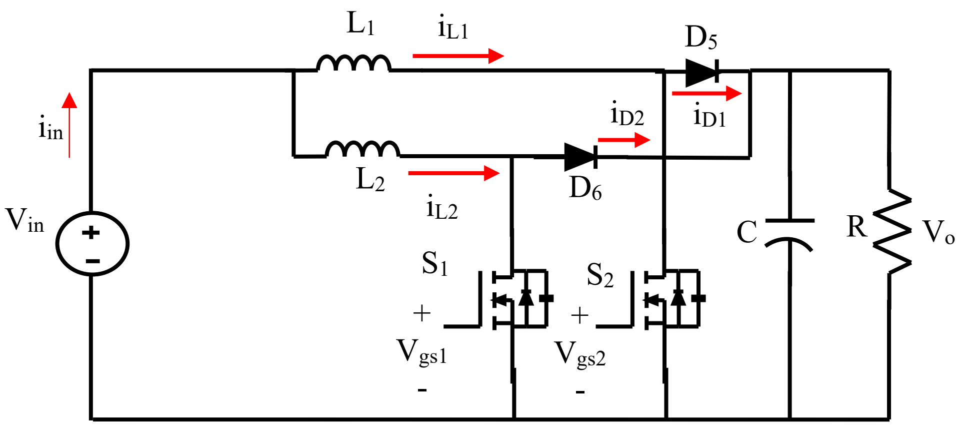

Figure 3. 6 Schematic of the two-phase interleaved boost converter.

3.5.1. Interleaving Effect on Input Ripple Current

The simulated current ripple waveforms of a two-phase interleaved boost converter are presented in Figure 3.7. In one switching period (0, *T*], S_1 is on in [0, *dT*); S_2 is on in [*T*/2, *T*/2+*dT*). The input current (i_{in}) is the sum of the two inductor currents (i_{L1}+ i_{L2}). Since the regions [0, T/2) and [T/2, T) are symmetrical, the frequency of the input current ripple is doubled. Thus, a half period [0, T/2) is sufficient to calculate the input current ripple.

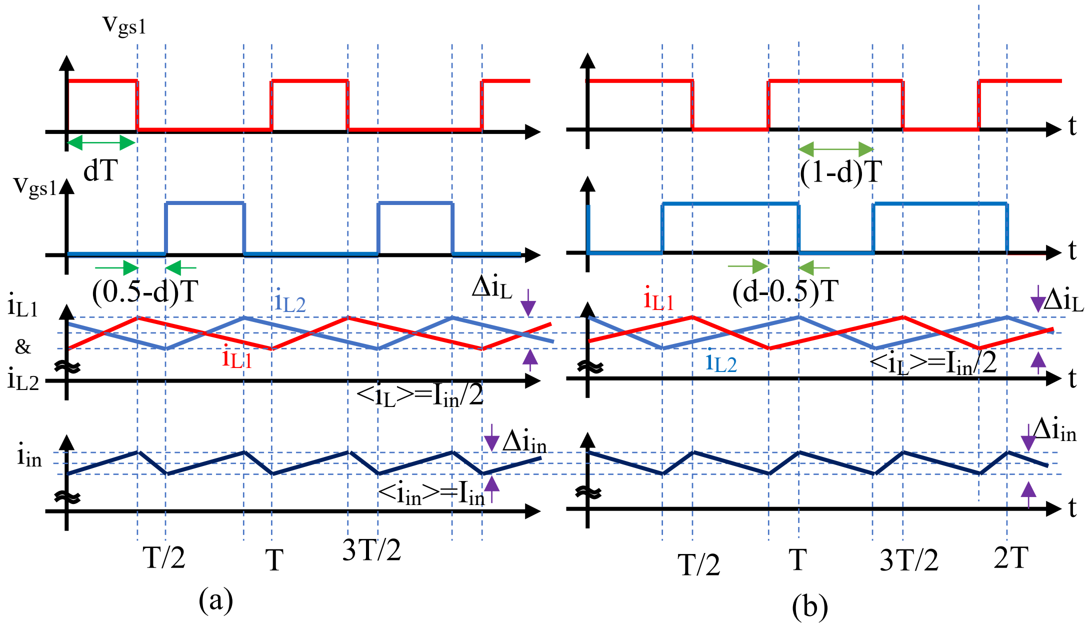

Figure 3. 7 Input current ripple of 2-phase interleaved boost converter. (a) d < 0.5. (b) d > 0.5.

If $d \leq 0.5$, from 0 to dT, S_1, and D_2 is on, while S_2 and D_1 are off. The voltage across L_1 is V_{in}.

Thus, i_{L1} increases at the speed of V_{in}/L. The voltage across L_2 is (V_{in} -V_o). Thus, i_{L2} changes at the speed of (V_{in}-V_o)/L. Since $I_{in} = I_{L1} + I_{L2}$, I_{in} increases from the minimum value to the maximum value at the speed of (2V_{in}-V_o)/L. Thus, the input current ripple could be calculated as Equation (3.11),

$$\Delta i_{in} = i_{max} - i_{min} = dT\frac{2V_{in} - V_o}{L} = dT\frac{(1-2d)}{L} \tag{3.11}$$

If d > 0.5, from 0 to (d-0.5) T, S_1 and S_2 are on, while D_1 and D_2 are off. The voltages across L_1 and L_2 are both V_{in}. Thus, both i_{L1} and i_{L1} increase at the speed of V_{in}/L. Since $I_{in} = I_{L1} + I_{L2}$, I_{in} increases from the minimum value to the maximum value at the speed of 2V_{in}/L. Thus, the input current ripple could be calculated as Equation (3.12),

$$\Delta i_{in} = i_{max} - i_{min} = (d-0.5)T\frac{2V_{in}}{L} = (1-d)T\frac{(2d-1)V_o}{L} \tag{3.12}$$

Either when $d < 0.5$, or $d > 0.5$, for each inductor, the current ripple could be calculated as Equation (3.13),

$$\Delta i_L = dT\frac{V_{in}}{L} = dT\frac{(1-d)V_O}{L} \tag{3.13}$$

Thus, the ripple current ratio, *K(d)*, could be calculated as Equation (3.14).

$$Kd = \frac{\Delta i_{in}}{\Delta i_L} = \begin{cases} \frac{1-2d}{1-d}, d \leq 0.5 \\ \frac{2d-1}{d}, d > 0.5 \end{cases} \tag{3.14}$$

According to Equations (3.10) and (3.14), the curves of the normalized current ripple as a function of the duty cycle are plotted in Figure 3.8. As seen in Figure 3.8, In comparison with single-phase boost topology, the two-phase interleaved boost converter has a smaller normalized ripple current over the full duty cycle range. The best input inductor ripple current cancellation occurs at a 50 percent duty cycle.

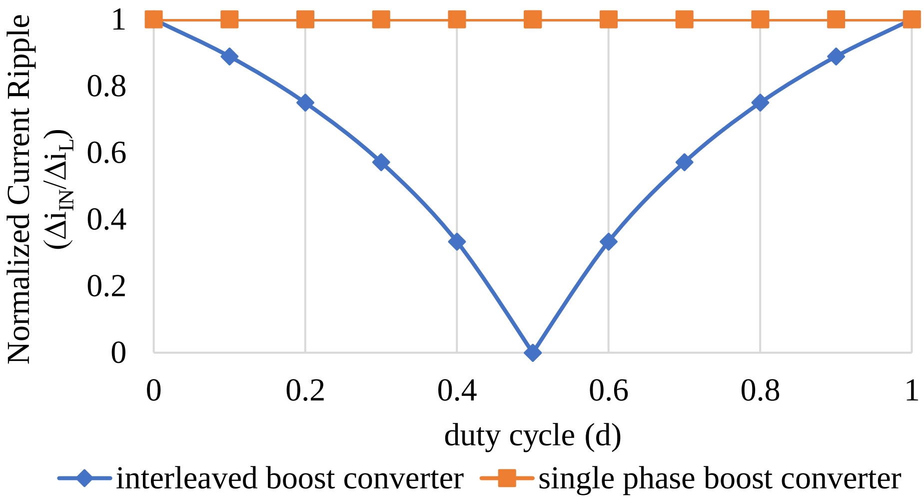

Figure 3. 8 Effectiveness of input ripple cancellation for interleaved converters.

3.5.2. Interleaving Effect on Magnetic Volume Reduction

The input current is evenly shared between the two inductors. For the interleaved topology, the energy stored in the inductor is described as Equation (3.15),

$$E = \frac{1}{2}L\left(\frac{I_{in}}{2}\right)^2 + \frac{1}{2}L\left(\frac{I_{in}}{2}\right)^2 = \frac{1}{4}LI_{in}{}^2 \tag{3.15}$$

According to Equation (3.15), the energy stored in the inductor is reduced to half in comparison with the single-phase boost topology. This reduction could effectively reduce the total energy and inductor volume for the same criteria as of the conventional boost converter. A volume reduction of 32% is reported in case an interleaved structure is used [83].

3.5.3. Interleaving Effect on the Output Capacitor

The root mean square (RMS) current in the output capacitor generates power losses due to the existence of equivalent series resistance (ESR). The temperature rise caused by the power loss may seriously reduce the capacitor lifetime [84]. For a two-phase interleaved boost converter, the output capacitor current is the sum of the two diode currents minus the dc output current (i_{D1} + i_{D2} - i_o). The output capacitor current waveform is plotted in Figure 3.9.

If $d \leq 0.5$ [Figure 3.9 (a)], the envelopes of the capacitor current square wave of the double phase interleaved structure can be calculated as Equations (3.16) and (3.17),

$$i_1(t) = i_{in}(t) - i_o(t) = d(t) i_{in}(t) \tag{3.16}$$

$$i_2(t) = \frac{1}{2} i_{in}(t) - i_o(t) = -[0.5 - d(t)]\, i_{in}(t) \tag{3.17}$$

If d > 0.5 [Figure 3.9 (b)], the envelopes of the capacitor current square wave can be calculated as,

$$i_1{}'(t) = \frac{1}{2} i_{in}(t) - i_o(t) = i_{in}(t)[d(t) - 0.5] \tag{3.18}$$

$$i_2{}'(t) = -i_o(t) = -i_{in}(t)[1 - d(t)] \tag{3.19}$$

Hence, the RMS value of capacitor current can be calculated as Equation (3.20)

$$i_{c,rms}(t) = \begin{cases} \sqrt{2[0.5 - d(t)] i_{in}(t)^2 + 2d(t) i_2(t)^2}, d \leq 0.5 \\ \sqrt{2[1 - d(t)]\, i_1{}'(t)^2 + 2[d(t) - 0.5] i_2{}'(t)^2} \end{cases} \tag{3.20}$$

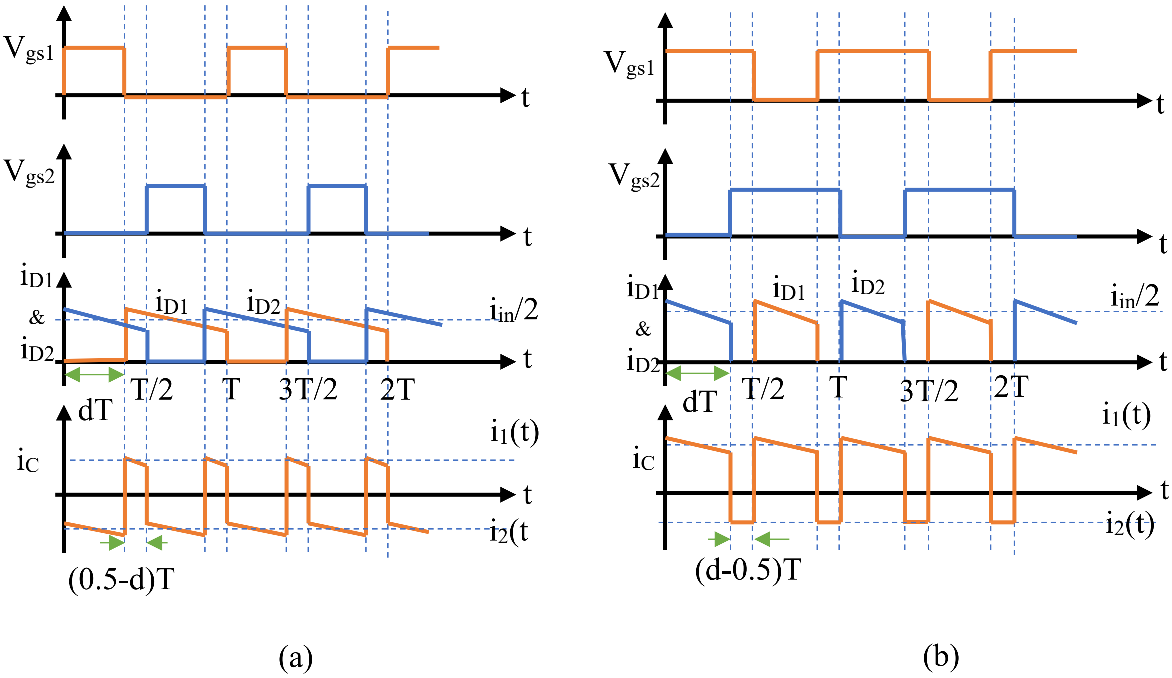

Figure 3. 9 Output capacitor current ripple of the two-phase interleaved boost converter (a) *d* < 0.5. (b) *d* > 0.5.

Substituting Equations (3.16-3.19) into Equation (3.20), the normalized capacitor RMS current $i_{c,\,RMS}/i_{in}$ can be obtained as Equation (3.21),

$$i_{c,rms}(t)/i_{in}(t) = \begin{cases} \sqrt{-d(t)^2 + 0.5d(t)}, & d \leq 0.5 \\ \sqrt{-d(t)^2 + 1.5d(t) - 0.5}, & d > 0.5 \end{cases} \tag{3.21}$$

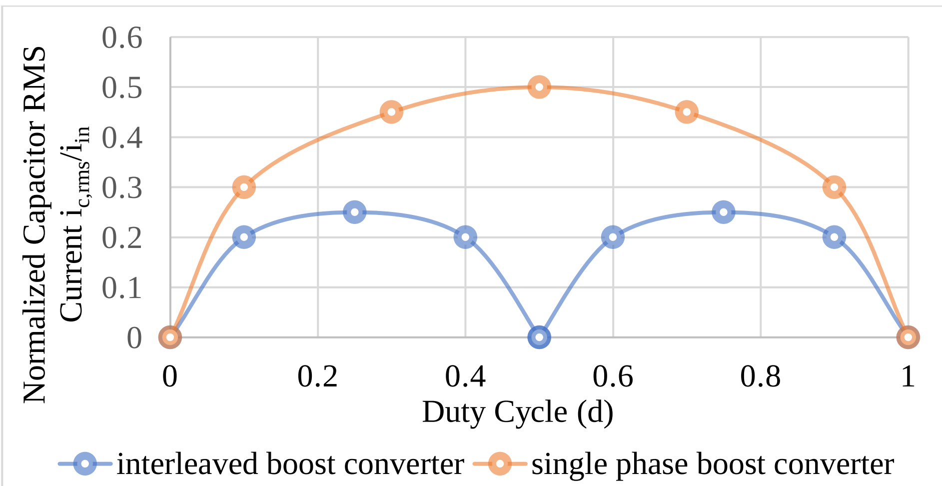

Figure 3. 10 Effectiveness capacitor RMS current reduction for interleaved converters.

According to Equations (3.14) and (3.21), the curves of normalized capacitor RMS current as a function of the duty cycle are plotted in Figure 3.10. In comparison with the single-phase boost structure, the peak capacitor RMS current is reduced to half in the two-phase interleaved structure. For the interleaved boost topology, as the duty cycle approaches 0, 0.5, and 1, the capacitor RMS current would approach zero. The improvement in capacitor RMS current reduces the power loss caused by ESR, reduces the electrical stress in the capacitor, and improves the system reliability.

3.6. Full-bridge LLC Converter

A full-bridge LLC resonant converter is shown in Figure 3.11. The series resonant network is formed by L_r, C_r, and L_m. L_m is arranged in parallel with the load. There are two resonance frequencies in this resonant network. The primary resonance frequency (f_p) is determined by L_r and C_r, while the secondary resonance frequency (f_s) is determined by $L_r + L_m$ and C_r. f_p and f_s are calculated in Equations (3.22) and (3.23), respectively.

$$f_p = \frac{1}{2\pi\sqrt{L_r C_r}} \tag{3.22}$$

$$f_s = \frac{1}{2\pi\sqrt{(L_r + L_m)C_r}} \tag{3.23}$$

Based on the relationship between the switching frequency (f), two resonant frequencies (f_p and f_s), and the load condition, there are five possible modes of operation.

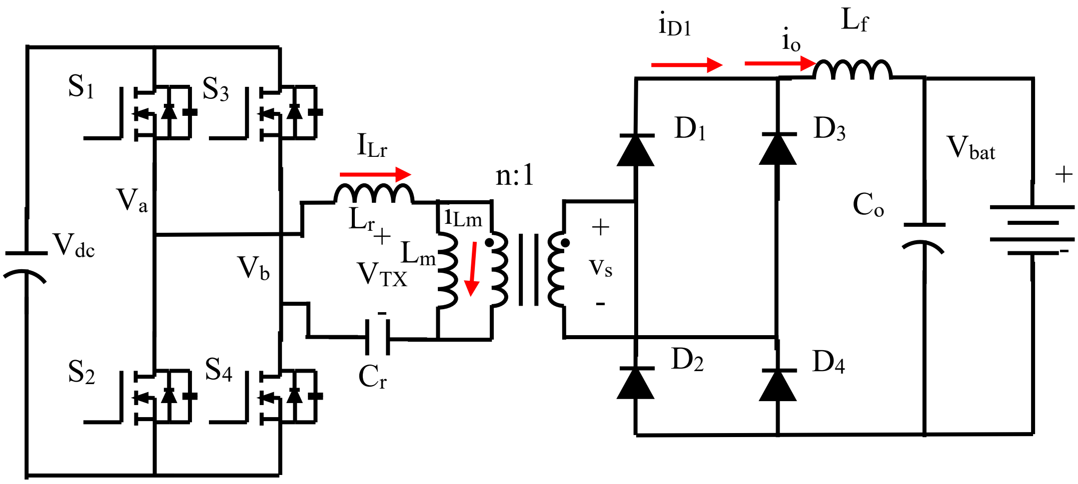

Figure 3. 11 Schematic of a full bridge LLC resonant converter.

3.6.1. Operation Analysis With $f < fs/2$

With the switching frequency smaller than $f_p/2$, the waveforms of the resonant tank input voltage (v_{ab}), resonant capacitor voltage (v_{Cr}), resonant inductor current (i_{Lr}), magnetizing inductor current (i_{Lm}), output current (i_o), and transformer primary voltage (v_t), are simulated. Figure 3.11 denotes those parameters with the signs. When switches S_1 and S_4 are turned on, the initial value of i_{Lr} could be either positive or negative, depending on the phase angle of the resonance. When $i_{Lr}(t_o)$ is positive, the simulated waveforms are shown in Figure 3.12. The operation of the half switching cycle can be divided into three modes, as shown in Figure 3.13. The discussion below is based on the condition when $i_{Lr}(t_o)$ is positive.

Mode I (t_o, t_1): According to Figure 3.12, $i_{Lr}(t_o) > 0$. At t_0, body diodes D_{S2} and D_{S3} are turned off at a finite current and a finite voltage. Mode I begin at this moment. i_{Lm} is equal to i_L; i_{Lr} is positive and flows through S_1 and S_4. Switches S_1 and S_4 turn on at a finite current and a finite voltage. Both the turn-off of D_{S2} and D_{S3} and the turn-on of S_1 and S_4 result in switching losses.

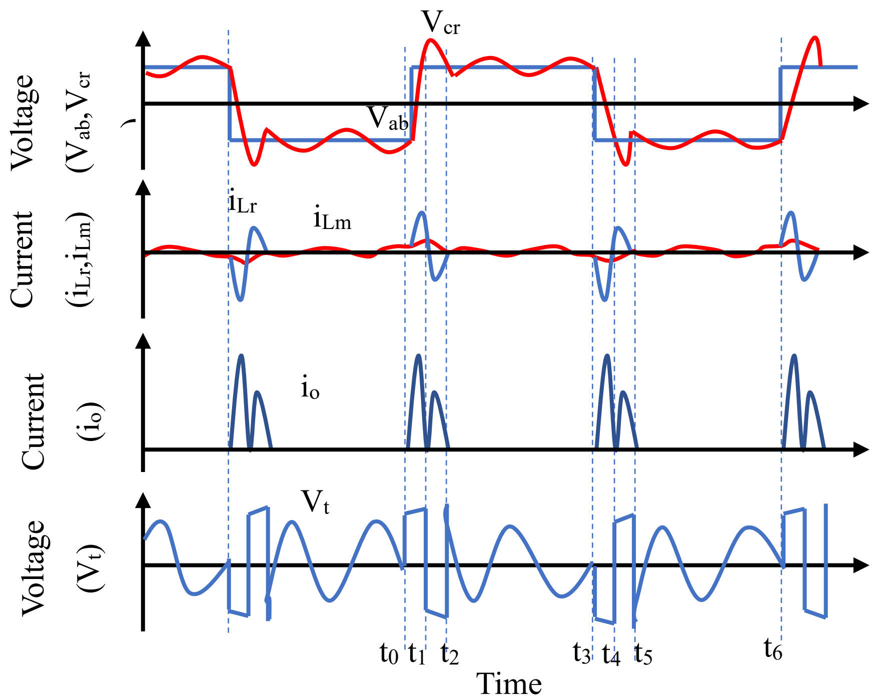

Figure 3. 12 Simulated waveforms of LLC resonant converter in ZCS operation with $f < f_s/2$ ($i_{Lr}(t_o) > 0$)

From t_o to t_1, the current flowing through S_1 and S_4 forces secondary diodes D_1 and D_4 to conduct. The voltage across the primary side of the transformer and L_m is nV_o. Thus, i_{Lm}

increases linearly. The sum of voltages applied across L_r and C_r equals to V_{DC} - nV_o. L_r resonates with C_r.

Mode II (t_1, t_2): At t_1, i_{Lm} reaches i_{Lr}, and mode II begins. Diodes D_1 and D_4 are turned off while diodes D_2 and D_3 is turned on. From t_1 to t_2, the sum of voltages applied across L_r and C_r equals to $V_{DC}+nV_o$. L_r resonates with C_r. During this mode, i_{Lr} crosses zero twice somewhere in between t_1 and t_2. The auto switch of conductions happens between S_1 & S_4 and D_{S1} & D_{S4} at those time points.

Mode III (t_2, t_3): At t_2, i_{Lm} reaches i_{Lr} again and mode III begins. Diodes D_2 and D_3 are turned off at zero current. From t_2 to t_3, secondary diodes $D_{1\text{-}4}$ are all off. The sum of voltages applied across L_m, L_r, and C_r equals to V_{DC}. L_m *participates* in the resonance with Lr and C_r. i_{Lm} is equal to i_{Lr}. At this mode, depending on the switching period, i_{Lr} crosses zero multiple times in between t_2 and t_3. Each time i_{Lr} cross zero, S_1 & S_4 and body diode D_{S1} & D_{S4} would swap conductions at zero voltage and zero current. At t_3, switches S_1 & S_4 are turned off at a finite current and a finite voltage. Mode III ends at this moment. i_{Lm} is equal to i_L; i_{Lr} is positive and flows through S_2 &S_3. Body diode D_{S2} & D_{S3} is turned off at a finite current and a finite voltage. Both the turn-on of S_2 & S_3 and the turn-off of D_{S2} & D_{S3} result in switching losses.

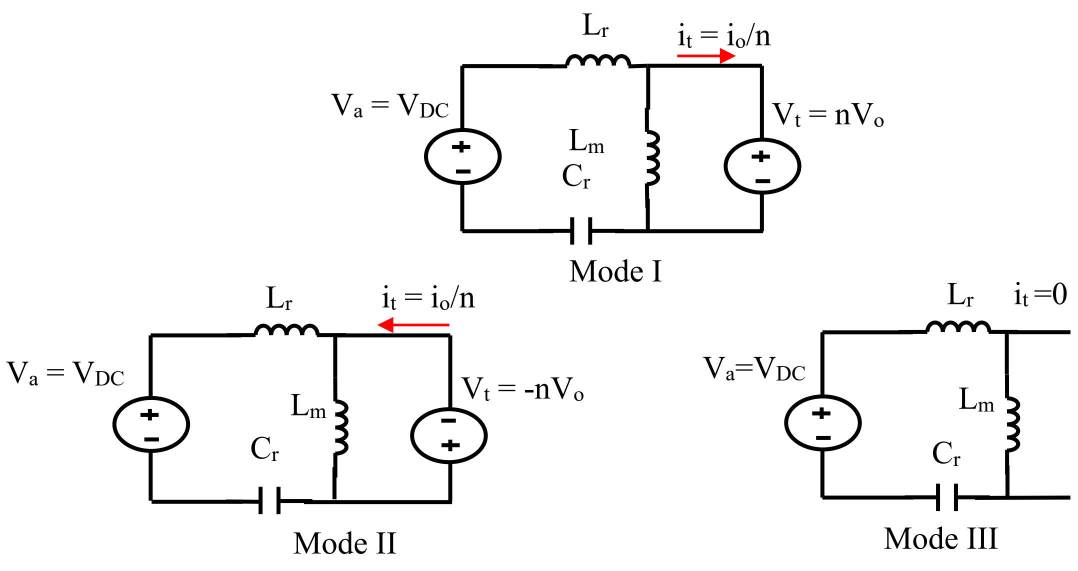

Figure 3. 13 Operating modes of LLC resonant converter in ZCS operation with $f < f_s/2$ ($i_{Lr}(t_o) > 0$).

For the next half-cycle, the operations are symmetrical to modes I-III. According to the operation modes analysis, the switches are turned off at zero voltage and zero current.

However, at the beginning of mode I and at the end of mode III, the turn-on of switches and the turn-off of body diodes are both hard switching.

3.6.2. Operation Analysis with *fs*/2 < *f* < *fs*

With the switching frequency between $f_s/2$ and f_s, the same group of waveforms is plotted in Figure 3.14. The operation of the half switching cycle can be divided into four modes. Figure 3.15 shows those four operating modes.

Mode I (t_o, t_1): At t_0, body diodes D_{S2} & D_{S3} are turned off at a finite current and a finite voltage. Mode I begin at this moment. i_{Lm} is equal to i_L; i_{Lr} is positive and flows through S_1 & S_4. Switches S_1 & S_4 turns on at a finite current and a finite voltage. Both the turn-off of D_{S2} & D_{S3} and the turn-on of S_1 & S_4 result in switching losses. From t_o to t_1, the current flowing through S_1 & S_4 forces secondary diodes D_1 & D_4 to conduct. The voltage across the primary side of the transformer and L_m is nV_o. Thus, I_{Lm} increases linearly. The sum of voltages applied across L_r and C_r equals to V_{DC} - nV_o. L_r resonates with C_r.

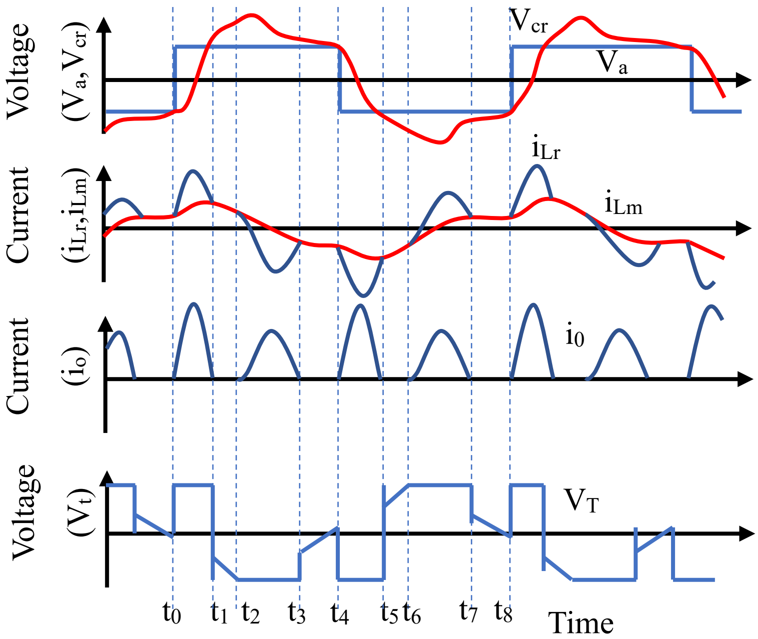

Figure 3. 14 Simulated waveforms of LLC resonant converter with $f_s/2 < f < f_s$.

Mode II (t_1, t_2): At t_1, i_{Lm} reaches i_{Lr}, and mode II begins. Diodes D_1 & D_4 are turned off at zero current without reverse recovery process. From t_1 to t_2, the sum of voltages applied across L_r, L_m and C_r equals to V_{DC}. L_m participates in the resonance with L_r and C_r.

Mode III (t2, t3): At t2, the voltage across *Lm* reaches -*nVo*, and mode III begins. From t_2 to t_3, the current flowing through S_1 & S_4 forces secondary diodes D_2 and D_3 to conduct.

The voltage across the primary side of the transformer and Lm is $-nVo$. Thus, i_{Lm} decreases linearly. The sum of voltages applied across Lr and Cr equals to $VDC+nVo$. Lr resonates with Cr. At this mode, in the resonance, i_{Lr} crosses zero somewhere in between t_2 and t_3. At this moment, S_1 & S_4 are turned off at zero current and the body diode D_{S1} & D_{S4} begins to conduct.

Mode IV (t3, t4): At t3, i_{Lm} reaches i_{Lr} again and mode IV begins. Diode D_1 & D_4 are turned off at zero current without small di/dt. From t_3 to t_4, the sum of voltages applied across L_r, L_m, and C_r equals to VDC. L_m participates in the resonance with L_r and C_r. At t_4, body diodes D_{S2} & D_{S3} are turned off at a finite current and a finite voltage. Mode IV ends at this moment. i_{Lm} is equal to i_L; i_{Lr} is negative and flows through S_2 & S_3. Switch S_2 & S_3 are turned on at a finite current and at a finite voltage. Both the turn-off of D_{S2} & D_{S3} and the turn-on of S_2 & S_3 result in turn-on switching losses.

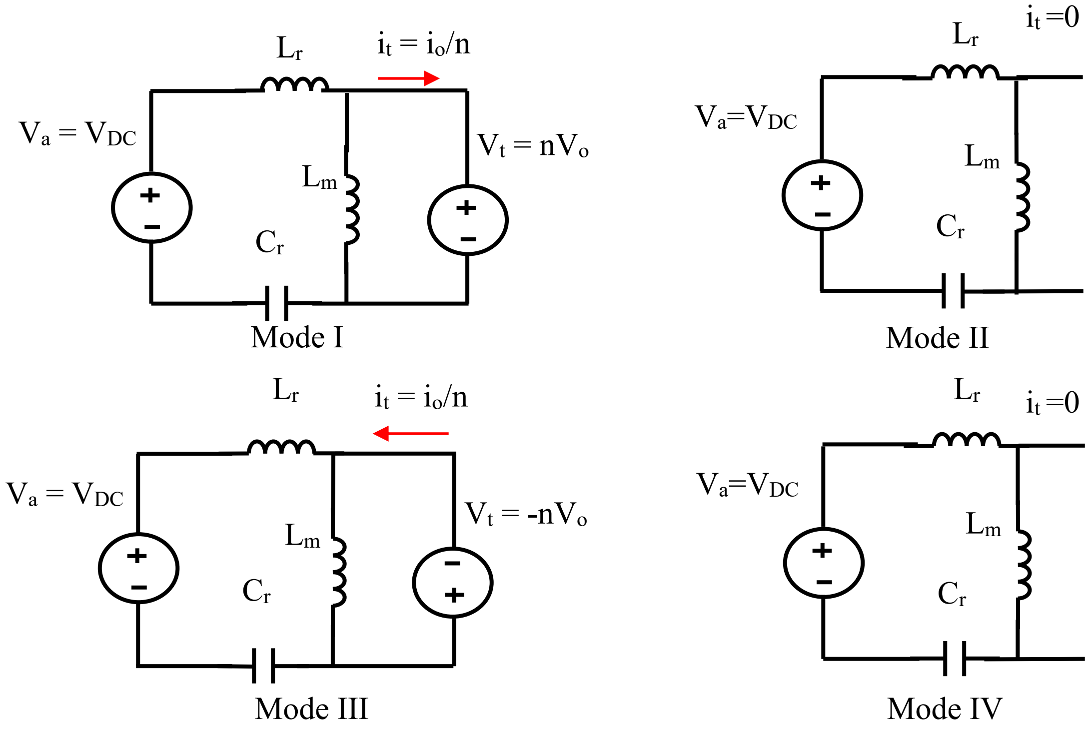

Figure 3. 15 Operating modes of LLC resonant converter with $f_s/2 < f < f_s$.

For the next half-cycle, the operations are symmetrical to modes I-IV. According to the operation modes analysis, the body diodes are turned on and the switches are turned off with soft switching (both zero voltage and zero current). Secondary diodes are also turned on and off at zero current. However, the turn-off of body diodes and the turn-on of switches are both hard switching.

3.6.3. Operation Analysis with $f_s < f < f_p$ (f close to f_s)

With the switching frequency between f_s and f_p, if f is sufficiently close to f_s, the same group of waveforms is plotted in Fig 3.16. The operation of half switching cycle can be divided into three modes. Fig. 3.17 shows those three operating modes.

Mode I (t_o, t_1): At t_0, body diodes D_{S2} & D_{S3} are turned off at a finite current and a finite voltage. Mode I begin at this moment. Switches S_1 & S_4 turn on at a finite current and at a finite voltage. Both the turn-off of D_{S2} & D_{S3} and the turn-on of S_1 & S_4 result in switching losses. From t_o to t_1, the current flowing through S_1 & S_4 forces secondary diodes D_1 & D_4 to conduct. The voltage across the primary side of the transformer and L_m is nV_o. Thus, i_{Lm} increases linearly. The sum of voltages applied across L_r and C_r equals to V_{DC}-nV_o. L_r resonates with C_r.

Mode II (t_1, t_2): At t_1, i_{Lm} reaches i_{Lr}, and mode II begins. Diodes D_1 & D_4 are turned off at zero current without small di/dt. From t_1 to t_2, the sum of voltages applied across L_r, L_m, and C_r equals to V_{DC}. L_m participates in the resonance with L_r and C_r.

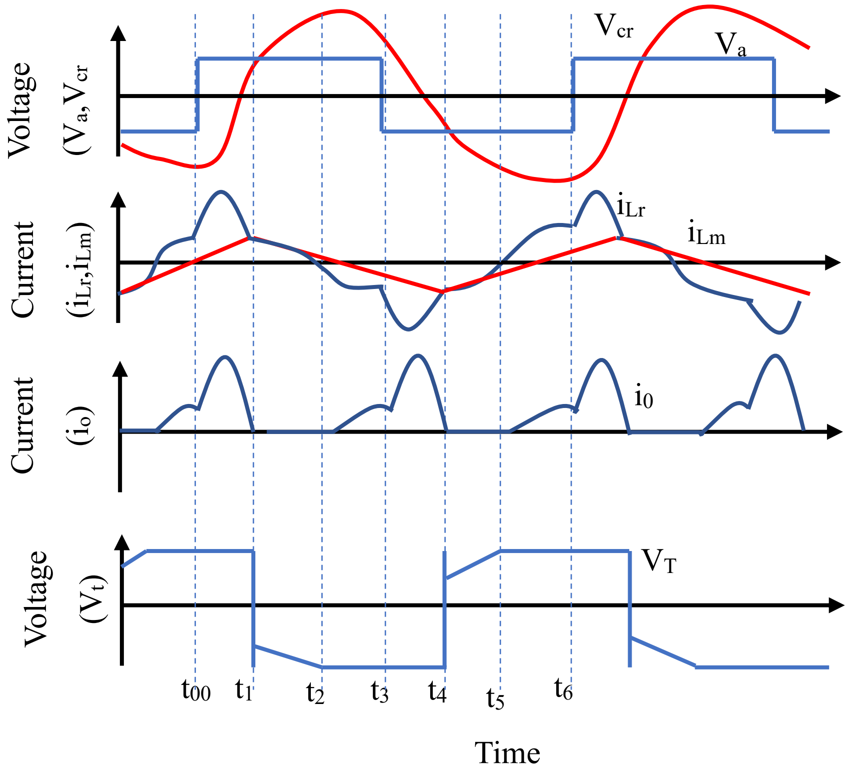

Figure 3. 16 Simulated waveforms of LLC resonant converter with $f_s < f < f_p$ (f close to f_s)

Mode III (t_2, t_3): At t_2, the voltage across L_m reaches -nV_o, and mode III begins. From t_2 to t_3, the current flowing through S_1 & S_4 forces secondary diode D_2 & D_3 to conduct. The voltage across the primary side of the transformer and L_m is $-nV_o$. Thus, I_{Lm} decreases linearly. The sum of voltages applied across L_r and C_r equals to $V_{DC}+nV_o$. L_r resonates with C_r. At this mode, in the resonance, i_{Lr} crosses zero somewhere in between t_2 and t_3. At this moment, S_1 & S_4 are turned off at zero current and the body diode D_{S1} & D_{S4} begin to conduct. At t_3, body diodes D_{S1} & D_{S4} are turned off at a finite current and a finite voltage. Mode III ends at this moment. i_{Lr} is negative and flows through S_2 & S_3. Switches S_2 & S_3 turn on at a finite current and a finite voltage. Both the turn-off of D_{S1} & D_{S4} and the turn-on of S_2 & S_3 result in turn-on switching losses.

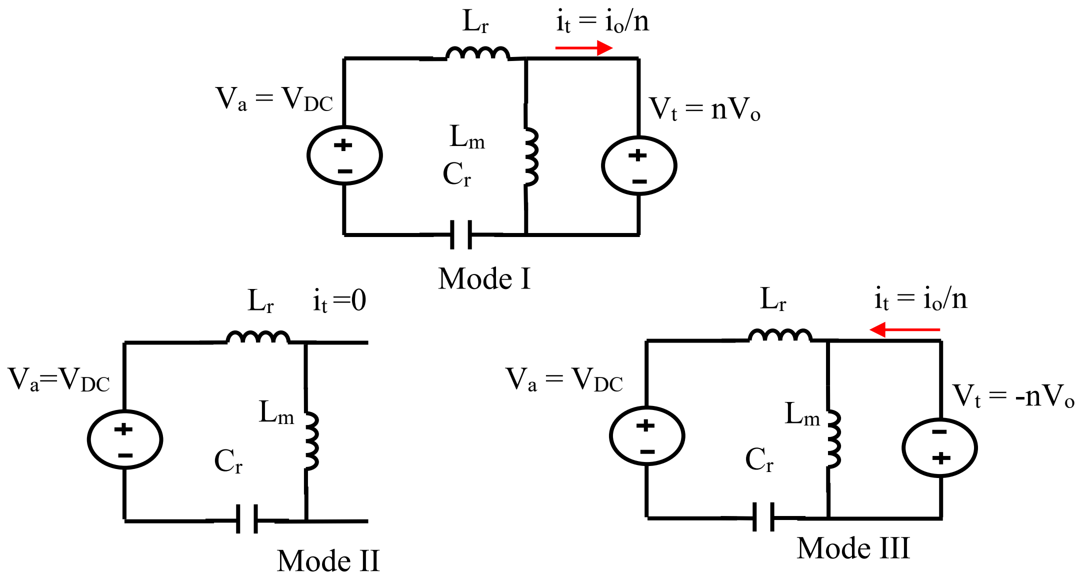

Figure 3. 17 Operating modes of LLC resonant converter with $f_s < f < f_p$ (f close to f_s).

For the next half-cycle, the operations are symmetrical to modes I-III. According to the operation modes analysis, the turn-off of switches is soft switching. Secondary diodes are turned off at zero current. However, the turn-off of body diodes and the turn-on of switches are both hard switching.

3.6.4. Operation Analysis with $f_s < f < f_p$ (f close to f_p)

With the switching frequency between f_s and f_p, if f is sufficiently close to f_p, the same group of waveforms is plotted in Figure 3.18. The operation of the half switching cycle can be divided into two modes. Figure 3.19 shows those two operating modes.

Mode I (t_0, t_1): At t_0, switches S_2 & S_3 are turned off at a finite current and a finite voltage. Mode I begin at this moment. Body diodes D_{S1} and D_{S4} turn on. The turn-off of S_2 & S_3 results in switching losses.

From t_0 to t_1, the current flowing through S_1 & S_4 forces secondary diode D_1 & D_4 to conduct. The voltage across the primary side of the transformer and L_m is nV_o. Thus, i_{Lm} increases linearly. The sum of voltages applied across L_r and C_r equals to V_{DC}. L_r resonates with C_r. At this mode, in the resonance, i_{Lr} crosses zero somewhere in between t_0 and t_1. At this moment, the body diodes D_{S1} & D_{S4} are turned off and the switches S_1 & S_4 begin to conduct at zero voltage.

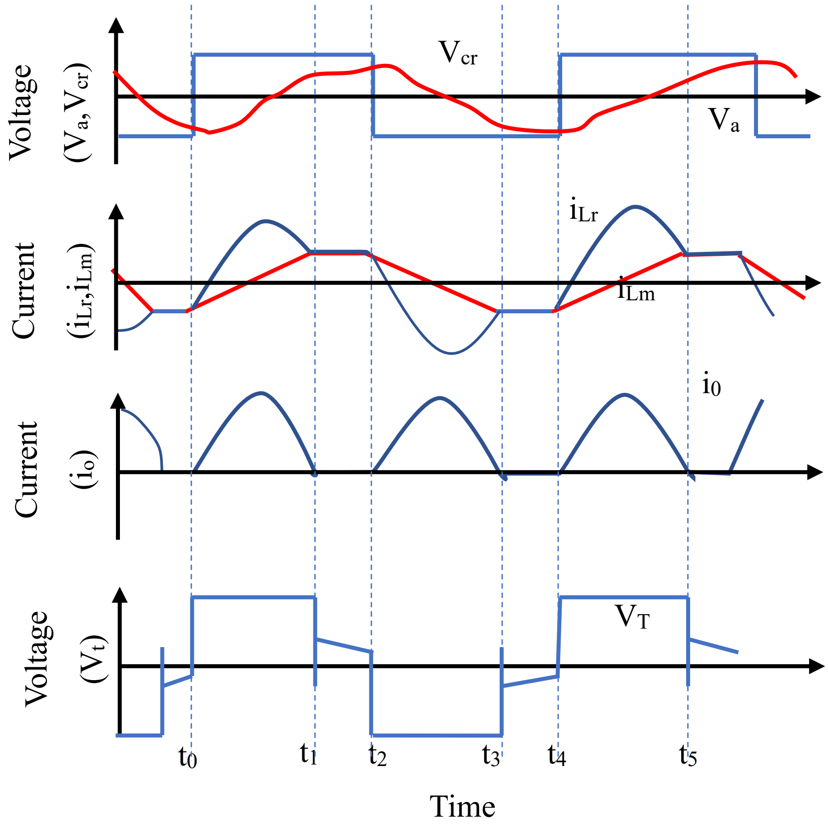

Figure 3. 18 Simulated waveforms of LLC resonant converter $f_s < f < f_p$ (f close to f_p).

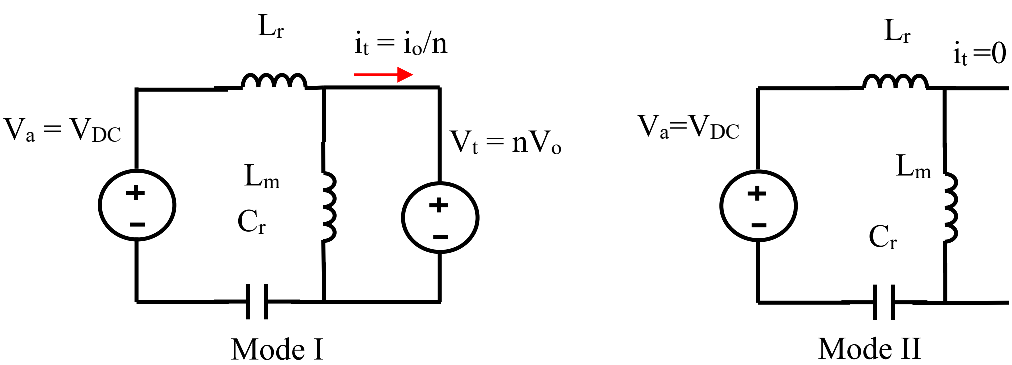

Figure 3. 19 Operating modes of LLC resonant converter $f_s < f < f_p$ (f close to f_p).

Mode II (t_1, t_2): At t_1, i_{Lm} reaches i_{Lr}, and mode II begins. Diodes D_1 and D_4 are turned off at zero current with small *di/dt*. From t_1 to t_2, the sum of voltages applied across L_r, L_m, and C_r equals to V_{DC}. L_m participates in the resonance with L_r and C_r.

At t_2, switches S_1 & S_4 are turned off at a finite current and a finite voltage. Mode II ends at this moment. i_{Lr} is positive and flows through body diode D_{S2} & D_{S3}. The turn-off of S_1 & S_4 results in switching losses.

For the next half-cycle, the operations are symmetrical to modes I-II. According to the operation modes analysis, the turn-on of switches and the turn-off of body diodes are both soft switching. Secondary diodes are turned off at zero current. However, the turn-off of switches is hard switching.

3.6.5. Operation Analysis with $f > f_p$

With the switching frequency larger than f_p, the group of waveforms is plotted in Figure 3.20. The operation of the half switching cycle can be divided into two modes. Figure 3.21 shows those two operating modes.

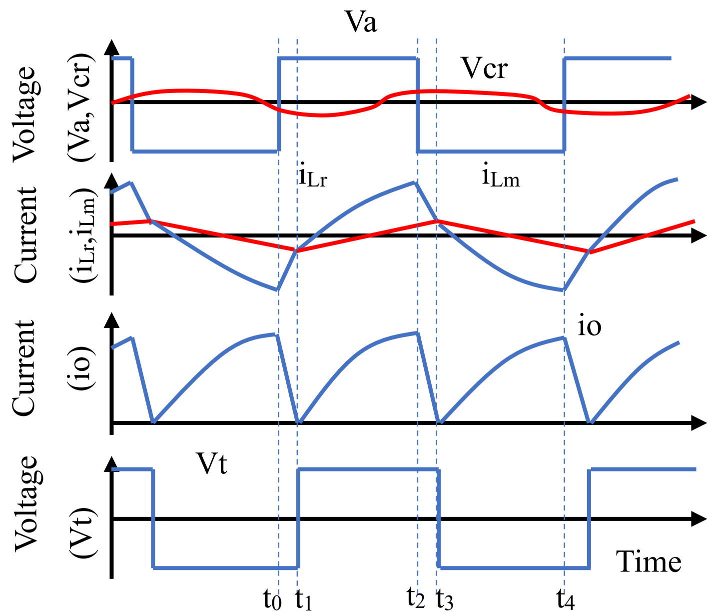

Figure 3. 20 Simulated waveforms of LLC resonant converter with $f > f_p$.

Mode I (t_0, t_1): At t_0, switches S_2 and S_3 are turned off at a finite current and a finite voltage. Mode I begin at this moment. Body diodes D_{S1} and D_{S4} turn on. The turn-off of S_2 and S_3 results in switching losses.

From t_o to t_1, the current flowing through S_1 & S_4 forces secondary diode D_2 & D_3 to conduct. The voltage across the primary side of the transformer and L_m is $-nV_o$. Thus, i_{Lm} decreases linearly. The sum of voltages applied across L_r and C_r equals to $V_{DC}+nV_o$. L_r resonates with C_r. Secondary diodes S_2 & S_3 are turned off with large di/dt. Turn off of S_2 & S_3 results in reverse recovery losses.

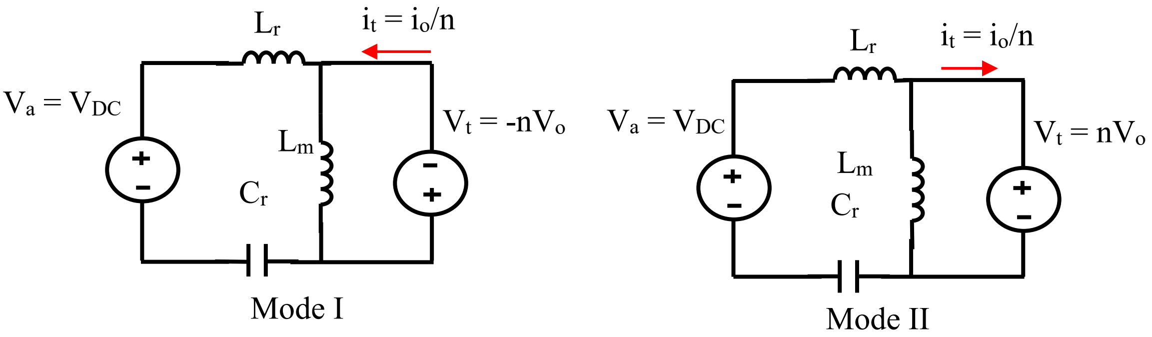

Figure 3. 21 Operating modes of LLC resonant converter with $f > f_p$.

Mode II (t_1, t_2): At t_1, i_{Lm} reaches i_{Lr}, and mode II begins. From t_1 to t_2, the current flowing through S_1 & S_4 forces secondary diodes D_1 & D_4 to conduct. The voltage across the primary side of the transformer and L_m is nV_o. Thus, I_{Lm} increases linearly. The sum of voltages applied across L_r and C_r equals to $V_{DC}-nV_o$. L_r resonates with C_r. L_m does not participate in the resonance with L_r and C_r. At t_2, switches S_1 & S_4 are turned off at a finite current and a finite voltage. Mode II ends at this moment. i_{Lr} is positive and flows through body diode D_{S2} & D_{S3}. The turn-off of S_1 & S_4 results in switching losses.

For the next half-cycle, the operations are symmetrical to modes I-II. According to the operation modes analysis, the turn-on of switches and the turn-off of body diodes are both soft switching (ZVS). Secondary diodes are also turned off at large di/dt. The turn-off of switches and the turn-off of secondary diodes are both hard switching and result in switching losses.

For the regions of (a) $f < f_s/2$, with $i_{Lr}(t_o) > 0$, (b) $f_s/2 < f < f_s$, and (c) $f_s < f < f_p$ with f close to f_s, the freewheeling diodes (body diodes) are turned off at a finite current and finite voltage. In those cases, the freewheeling diodes must have good reverse-recovery characteristics to avoid large reverse spikes flowing through the switches, and to minimize the diode turn-off losses. It is possible to use thyristors as switches in low-switching frequency applications.

For the regions of (d) $f_s < f < f_p$ with f close to f_p, and (e) $f > f_p$, the freewheeling diodes (body diodes) are turned off at a zero current and at zero voltage. Thus, the freewheeling diodes do not need to have very fast reverse-recovery characteristics. In those cases, it is possible to use MOSFETs as switches in high-switching frequency applications.

In conclusion, if MOSFETs are used as the primary switches, the LLC converter should operate in the regions (d) $f_s < f < f_p$ with f close to f_p, and (e) $f > f_p$.

3.6.6. Summary of Switching Conditions

Based on previous analyses, the switching conditions of the LLC converter are summarized in Table 3.1.

Table 3. 1 Switching conditions of LLC converter

Frequency range	Additional condition	Hard switching		Soft switching (ZCS AND ZVS)	
		Turn on	Turn off	Turn on	Turn off
f<fs/2	i_{Lr}(to)>0	S_1-S_4	D_{S1}-D_{S4}		S_1-S_4, D_{S1}-D_{S4}
fs/2<f<fs	n/a	S_1-S_4	D_{S1}-D_{S4}		S_1-S_4, D_{S1}-D_{S4}
fs<f<fp	f near fs	S_1-S_4	D_{S1}-D_{S4}		S_1-S_4, D_1-D_4
	f near fp	None	S_1-S_4	S_1-S_4	D_{S1}-D_{S4}, D_1-D_4
f>fp	n/a	None	S_1-S_4, D_1-D_4	S_1-S_4	D_{S1}-D_{S4}

3.7. Battery Management System

The battery management system (BMS) is responsible for the safe operation, performance monitoring, and battery life assessment under diverse charge-discharge and environmental conditions. When designing a BMS, it is needed to develop feedback and supervisory control that:

- Monitors cell voltage and temperature;
- Estimates state-of-charge;
- Limits power input and output for thermal and overcharge protection;
- Controls the charging profile;
- Balances the state-of-charge of individual cells;
- Isolates the battery pack from the load when necessary.

Simulink modeling and simulation capabilities enable BMS development, including cell-equivalent circuit formulation and parameterization, electronic circuit design, control logic, automatic code generation, verification, and validation. With Simulink, the system can be designed and simulate the battery management systems by:

- Modeling battery packs using electrical networks whose topology mirrors that of the actual system and scales with the number of cells.
- Parameterizing equivalent circuit elements using test data for an accurate representation of cell chemistry.
- Designing the power electronics circuit that connects the pack with the controls.
- Developing closed-loop control algorithms for supervisory and fault detection logic
- Designing state observers for state-of-charge estimation.

3.7.1. Battery Cell Modeling

A lithium-ion battery is the widely used battery type in modern electric vehicles because of their high specific energy, good cycle life, and very low self-discharge. However, all these advantages come with the need for careful battery management. To ensure safe operation and acceptable durability. For example, voltage and temperature should remain with a suitable limit to avoid early degradation as should power delivery an acceptable. This section describes how to create a mathematical model for a battery cell to be used in battery system design and control of a lithium-ion battery cell in a charging system.

First, it is necessary to describe how the equivalent circuit represents the dynamic behavior of the battery cell. This is important since the BMS as any controller needs to tune to the dynamics of the plant it is connected to. The good model of the battery cell describes how it behaves as a function of environmental conditions and state of charge.

Secondly, parameterizing the equivalent circuit based on measurement data using parameter estimation has to be done using technique-based optimization to fit all experimental data. Finally, improve and refine an estimation adding fidelity to a model with the use of more elaborate equivalent topologies, complement the study with curve fitting and accelerate calculations using parallel computing.

Developing a battery system using model-based design requires a model of the battery cell that accurately represents its real-life behaviors and dependency on environmental and operating conditions. Although it will be desirable to capture all the details electrochemical phenomena present in the battery cell. Control oriented applications depend on a more efficient approach that can be scaled up to the battery pack level and eventually capable of realistic simulation. A widely accepted compromise between fidelity and simulation time is the equivalent circuit.

The equivalent circuit is an electrochemical analogy aiming and representing the behaviors of an electrochemical cell using a relatively simple electrical circuit containing a voltage source and several resister and capacitor that collectively reflect the open circuit potential, the internal resistance, and the relaxation time of the real cell. When modeling a battery cell using an equivalent circuit it is important to choose circuit topology and parameterization, in a way that it can respond as similarly as possible as a physical battery cell.

The Partnership for a New Generation of Vehicles (PNGV) model is a typical nonlinear equivalent circuit model, which can describe the characteristics of the battery more accurately considering the influence of the battery state and working conditions on the model parameters [85]. The parameters of the PNGV equivalent circuit model are functions of SOC and temperature. The PNGV model is suitable for modeling power Li-ion batteries because the PNGV model can reflect its transient response process at a very high rate of charging and discharging.

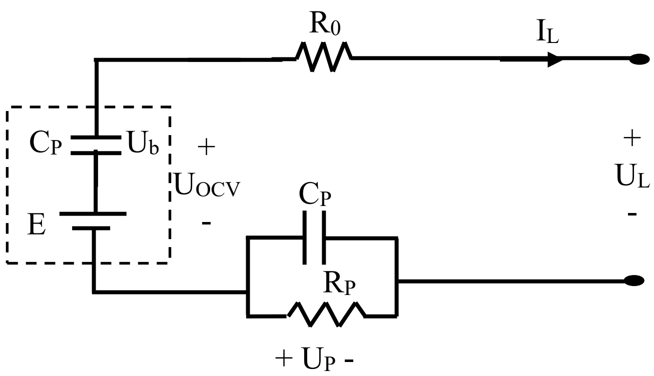

Figure 3. 22 Structure of PNGV model [85]

The structure of the PNGV is shown in Figure 3.22. In the model, E is an ideal voltage source, which expresses the open-circuit voltage of the battery, capacitor C_b describes the variation of open-circuit voltage caused by the accumulation of current. These two parameters together express the variation of open-circuit voltage. R_o represents the ohmic resistance of the battery, R_P and C_P represent the polarization resistance and the polarization capacitance of the battery respectively. R_P and C_P in parallel simulate the polarization characteristic during charging and discharging. I_L denotes the current in the loop, U_L represents the external voltage of the battery. The relationship between U_L and I_L is established according to the equivalent circuit model, which is shown as Equation (3.24).

$$U_L = U_{ocv} - I_L R_o - U_P \tag{3.24}$$

The specimens used in this work are Li-ion batteries with a nominal capacity of 31 Ah and a voltage of 3.6V. According to the Freedom CAR Battery Laboratory Manual [86], the Hybrid Pulse Power Characterization (HPPC) test is carried out to measure the dynamic behavior of the battery. Figure 3.23 shows the current activation and voltage response profiles of a portion of the HPPC test.

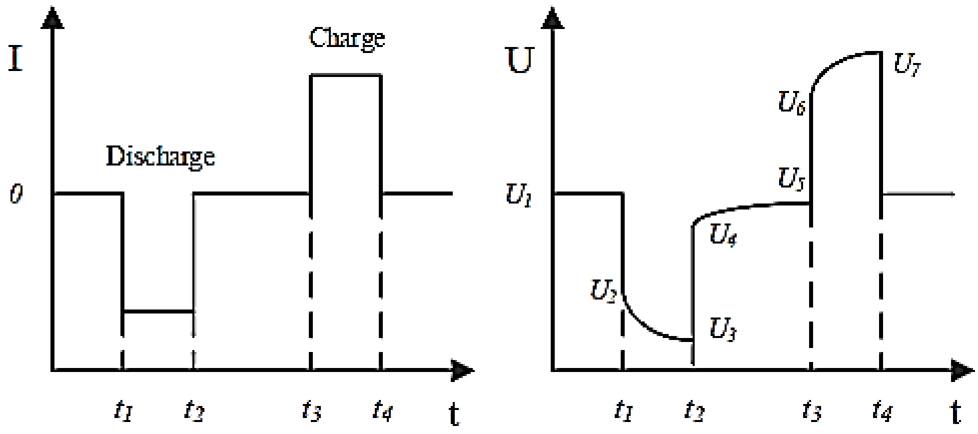

Figure 3. 23 Schematic of current and voltage profiles in the HPPC test [87]

From the voltage response of the HPPC test, features can be extracted and model parameters can be calculated based on the following analysis.

(1) At discharging time t_1, voltage drops vertically. Such an instantaneous voltage drop is caused by the battery's ohmic resistance. R_o can be calculated by using Equation (3.25).

$$R_o = \frac{\Delta U}{I} \tag{3.25}$$

Where $\Delta U = U_1 - U_2$ and I is discharging current

(2) Voltage U_1 is greater than voltage U_2, which is the recovered stable voltage after discharging. This is because discharging current integration on the polarization capacitor makes a voltage difference. So C_b can be calculated by Equation (3.26) and Equation (3.27).

$$\Delta Q U_{ocv} = \frac{1}{2} C_b [(U_{ocv} + \Delta U_{ocv})^2 - U_{ocv}^2] \tag{3.26}$$

$$C_b = \frac{\Delta Q}{\Delta U_{ocv}} \tag{3.27}$$

According to the law of energy conservation, Equation 3.26 is simplified as Equation 3.27, ΔQ is the discharging capacity and is recorded by the test instrument. ΔU_{OCV} is the open-circuit voltage difference, which is U_1-U_5.

(3) After discharging, the terminal voltage of the battery rises slowly. In this process, the polarization capacitor discharges through polarization resistance, which is the zero-input response of the RC parallel circuit. The time constant τ can be calculated.

$$U_p = U_o e^{-t/\tau} \tag{3.28}$$

Where U_o is the initial polarization voltage and τ is the time constant of the RC parallel unit.

(4) During discharging, the terminal voltage of the battery drops slowly. In this process, the polarization capacitor is charged by the polarization current, which is the zero-state response of the RC parallel circuit. Parameter R_P can then be calculated using Equation (3.29).

$$U = U' - \frac{1}{C_b} \int I dt - I R_P - \left(1 - e^{-\frac{t}{\tau}}\right) \tag{3.29}$$

Where U' is the voltage after the vertical drop, namely U_2 in Figure 3.23. Substituting the obtained time constant τ into Equation (3.29). In the same way, then parameter Rp can be identified by fitting Equation (3.29) to the slow-changing portion of the discharging voltage profile. The parameters of the polarization capacitance C_P were obtained by dividing the time constant τ by R_P. The whole process of parameter identification is shown in Figure 3.24.

One possible way to determine the characteristics parameter of an equivalent circuit is by performing parameter estimation in MATLAB software. Parameter estimation is an optimization-based procedure by which simulation results are compared against experimental measurement and the parameters of the model are determined in such a way the simulation matches the experiment.

It all begins by proposing an equivalent circuit architecture based on previous knowledge of the system which is believed to represent the behavior of the real system. The initial parameterization of the equivalent circuit is done using tentative values based on experience. The simulation is set to reproduce the condition of the discharge experiment typically done in a controlled temperature environment.

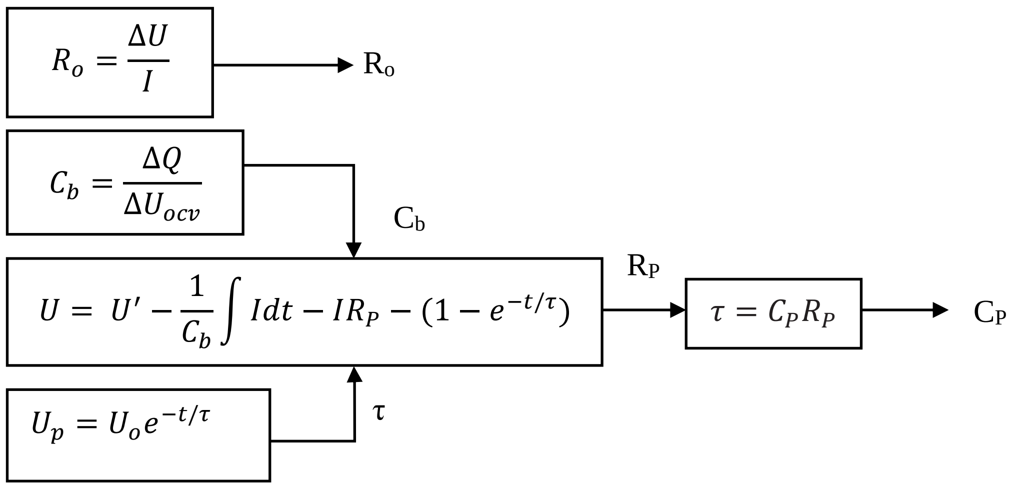

Figure 3. 24 Process of parameter identification.

Let’s look at experimental data first keeping the constant temperature of 20^{0}C. A 31Ah lithium-ion battery cell is discharging from the full charged stage down to zero SOC as shown in Figure 3.25.

Since the experiment is not done in the laboratory due to the unavailability of lithium-ion battery this experimental data is taken from the literature [88].

While current flowing out of the battery the measured voltage drops and then recovers after the pulse. The shape of voltage drops and recovery are characteristics of this particular battery chemistry. The goal of these procedures is to be able to reproduce it using the equivalent circuit with the right parameters.

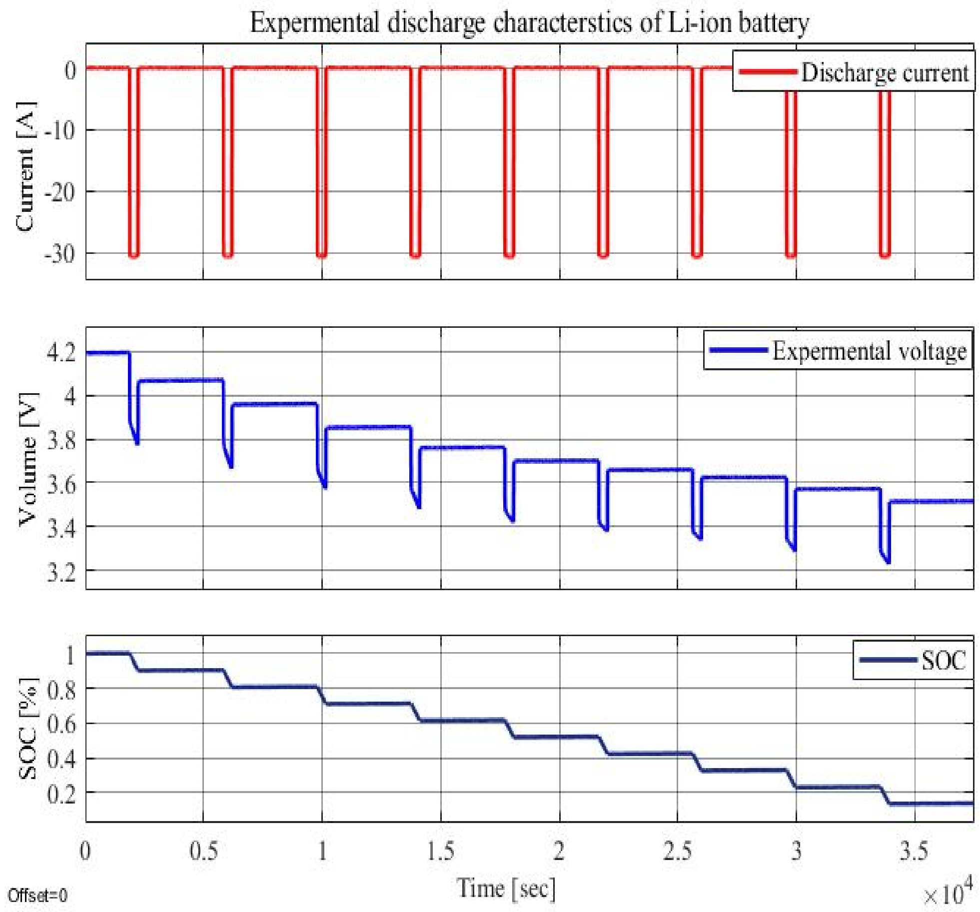

Figure 3. 25 experimental discharge characteristics of Li-ion battery cell [88]

More specifically the series resistance needs to account for the instantaneous portion of the recovery, the combined RC pair needs to explain the initial portion of the recovery and the voltage source must deliver the correct OCV as the function of SOC.

Additionally, one can observe the response is different at different state of charge level because of the state of charge can't be controlled directly. However, it is the state that changes as current drops out of the cell.

Figure 3.26 shows the Simulink model designed for such purpose. The series of discharge current pulse is drawn from the equivalent circuit inside the lithium-ion battery block. At the same time, the voltage across terminals is measured using the voltage sensor that is located on the right of the lithium-ion battery cell to be compared by the optimizer against voltage measured experimentally.

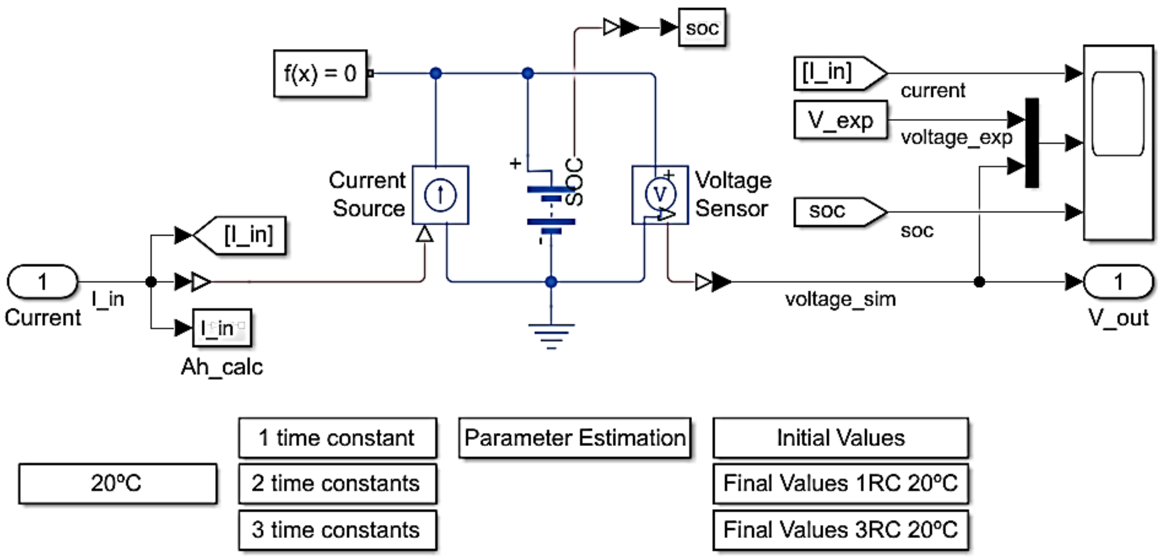

Figure 3. 26 Parameter optimization circuit for lithium-ion battery model

As it can be seen from Figure 3.27, the one-time constant is not enough to capture the dynamics of this particular cell. There is a mismatch between simulation and experimental data measurement. Therefore, by increasing the number of RC pairs the estimated data must fit the experiment result.

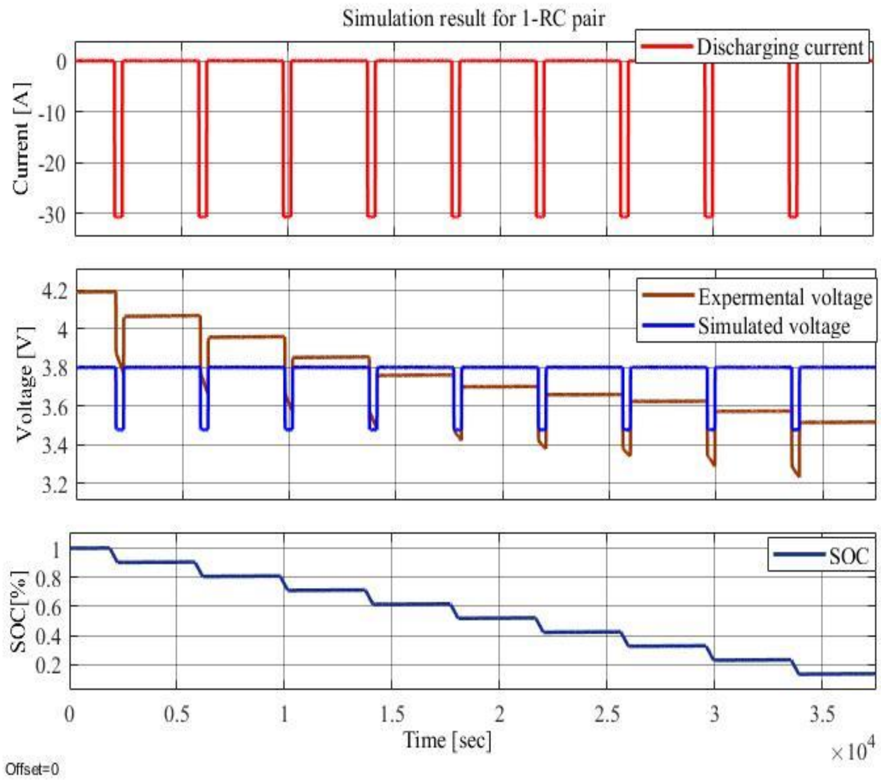

Figure 3.27 Parameter estimation using 1-RC pair

Simulink will work with MATLAB optimization functions trying to minimize the difference between simulation and experimental data by adjusting the parameters of the equivalent circuit. This is done using a library called Simulink design optimization. This tool acts as a bridge between Simulink and MATLAB optimization function. Finally, by using MATLAB optimization function and by making the RC pair three exact the same waveform with the experimental data is achieved as shown below in Figure 3.28.

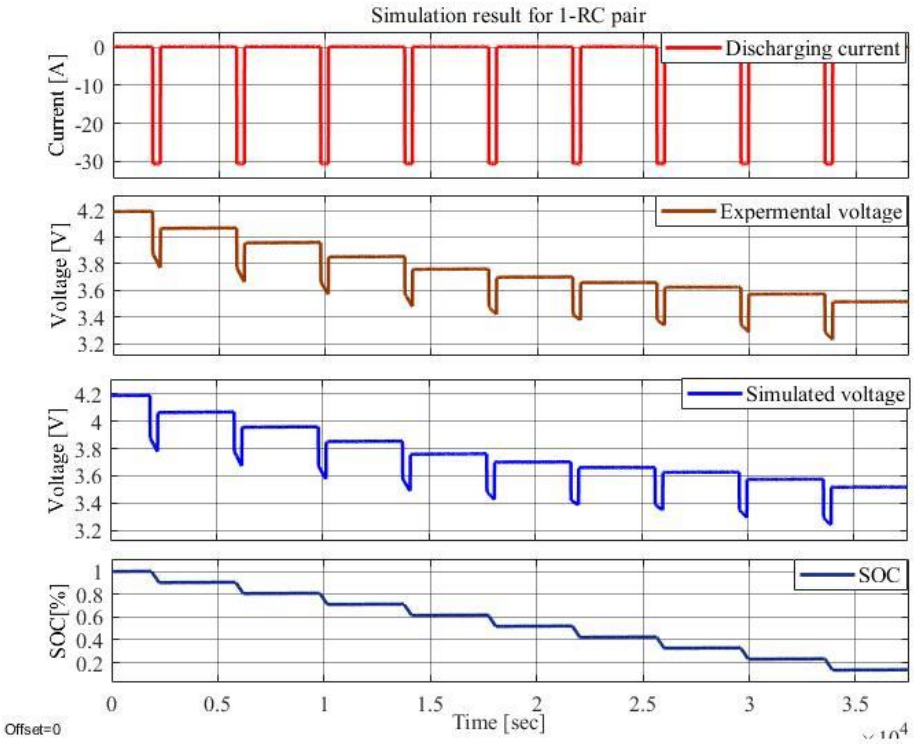

Figure 3.28 Parameter estimation using 3-RC pair

3.7.1. State of Charge Estimation of the Battery Pack.

Another function of BMS is to simulate the repeated charge-discharge profile of the battery by using non-linear Kalman filter based SOC estimation method. Precise estimation of SOC is critically important in BMS for a variety of reasons. Among them the mitigation of range anxiety. If anyone charging the electric car, they have to know how much the battery is charged before unplugging it.

Unlike a conventional vehicle fuel tank whose level can be directly measured the SOC, the battery cannot be measured by using an indirect method. For example, OCV estimation, coulomb counting, or the combination of both. These methods have drawbacks and sometimes they are not applied effectively. For example, for cells with a very flat discharge profile. The more advanced approach to estimating the state of charge preferable.

Typically, a Kalman filter which takes the input and the output signal from the battery and computes the internal state using the model of the battery cell and recursive algorithm.

The unscented Kalman filter algorithm has been widely used in the optimization of nonlinear systems estimation. UKF algorithm can follow the accurate state of the system even the initial value has an apparent bias.

$$x_{k+1} = f(x_k, u_k) + w_k \tag{3.30}$$

$$y_k = g(x_k, u_k) + v_k \tag{3.31}$$

Equation (3.30) and Equation (3.31) are the system's state equation and observation equation respectively, where x_k is the system's state variable, y_k is the system's output variable, u_k denotes the system's input variable. $f(x_k,u_k)$ and $g(x_k,u_k)$ are both nonlinear functions. Function $f(x_k,u_k)$ can be derived from the equivalent circuit model and function $g(x_k,u_k)$ is the fitting equation of the OCV curve . Both w_k and v_k are system noises, which are independent of each other. The unscented Kalman filter algorithm can be summarized as shown in Table 3.2.

Table 3. 2 Summary of the unscented Kalman filter approach for SOC estimation [89]

Non-linear state-space model
$\boldsymbol{x_{k+1} = f(x_k, u_k) + w_k}$
$\boldsymbol{y_k = g(x_k, u_k) + v_k}$
Initialization
Measure ambient temperature, prepare U_{OCV} (SOC, T) and R_p, C_p
Initial guess: S_0
Covariance matrix: P_0
Process and measurement noise covariance: $\sum \boldsymbol{wo}$, $\sum \boldsymbol{v}$
Computation
For k = 1, 2, . . . compute
Generate sigma points at time k-1, (k ∈ [l, … ∞])
$\boldsymbol{x_{k-1} = \begin{bmatrix} S_{k-1} \\ R_{k-1} \end{bmatrix} = [\bar{x}_{k-1}, \bar{x}_{k-1} + \sqrt{(n+\lambda)P_{k-1}}, \bar{x}_{k-1} - \sqrt{(n+\lambda)P_{k-1}}}$
Predict the prior state mean and covariance
Calculate sigma points through state function:

$$\boldsymbol{x^i_{k|k-1}} = \begin{bmatrix} \boldsymbol{S^i_{k|k-1}} \\ \boldsymbol{R^i_{k|k-1}} \end{bmatrix} = \begin{bmatrix} \boldsymbol{S^i_{k-1}} - \dfrac{\boldsymbol{I_{K-1} * \Delta t}}{\boldsymbol{C_n}} \\ \boldsymbol{R^i_{k-1}} \end{bmatrix}, \boldsymbol{i = 1, \dots, 2n}$$

Calculate the prior mean and covariance:

$$\boldsymbol{\hat{x}_k^-} = \sum_{i=0}^{2n} \boldsymbol{w_m^i\, x^i_{k|k-1}}, \boldsymbol{P_k^-} = \sum_{i=0}^{2n} \boldsymbol{w_c^i} \left[\boldsymbol{x^i_{k|k-1}} - \boldsymbol{\hat{x}_k^-}\right]\left[\boldsymbol{x^i_{k|k-1}} - \boldsymbol{\hat{x}_k^-}\right]^{\boldsymbol{T}} + \sum \boldsymbol{w}$$

Update using the measurement function

Calculate the sigma points: $\boldsymbol{y_{k|k-1}} = \boldsymbol{U_{OCV}}\left(\boldsymbol{soc_{k|k-1}}, \boldsymbol{T}\right) - \boldsymbol{I_k} * \boldsymbol{R(T)_k} + \boldsymbol{C(T)}$

Calculate the propagated mean: $\boldsymbol{\hat{y}_k^-} = \sum_{i=0}^{2n} \boldsymbol{w_m^i\, y^i_{k|k-1}}$

Calculate the covariance of the measurement: $\boldsymbol{P_{y_k^-, y_k^-}} = \sum_{i=0}^{2n} \boldsymbol{w_c^j} \left[\boldsymbol{y^i_{k|k-1}} - \boldsymbol{\hat{y}_k^-}\right]^{\boldsymbol{T}} + \sum \boldsymbol{v}$

Calculate the cross-covariance and the state and measurement:

$$\boldsymbol{P_{x_k^-, y_k^-}} = \sum_{i=0}^{2n} \boldsymbol{w_c^i} \left[\boldsymbol{x^i_{k|k-1}} - \boldsymbol{\hat{x}_k^-}\right]\left[\boldsymbol{y^i_{k|k-1}} - \boldsymbol{\hat{y}_k^-}\right]^{\boldsymbol{T}}$$

Compute filter gain and update and achieve the posterior SOC estimation

Compute the filter gain: $\boldsymbol{k_k} = \boldsymbol{P_{x_k^-, y_k^-} P^{-1}_{y_k^-, y_k^-}}$

Update the posterior state mean: $\boldsymbol{S_k^+} = \boldsymbol{S_k^-} + \boldsymbol{k_k}(\boldsymbol{y_k} - \boldsymbol{\hat{y}_k^-})$

Update the posterior covariance: $\boldsymbol{P_k} = \boldsymbol{P_k^{-1}} + \boldsymbol{k_k P_{x_k^-, y_k^-} k_k^T}$

An unscented Kalman filter is a type of non-linear estimator from the control system toolbox of MATLAB. A non-linear observer is needed because of the non-linear relationship between OCV and SOC.

As shown in Figure 3.29 the UKF requires a minimum of two functions as an argument. State transition and measurement function. The former describes the relationship between state and inputs. The latter yells the system output as a function of state and input. These functions can be in MATLAB or Simulink function block. This research uses the latter.

As shown in Figure 3.30, the state transition function calculates the evolution of the states based on the current input. The calculation requires the previous computation of the equivalent circuit parameters using the temperature and current signals that go through a nonlinear lookup table that characterizes the battery cell that has been estimated above in the battery modeling section.

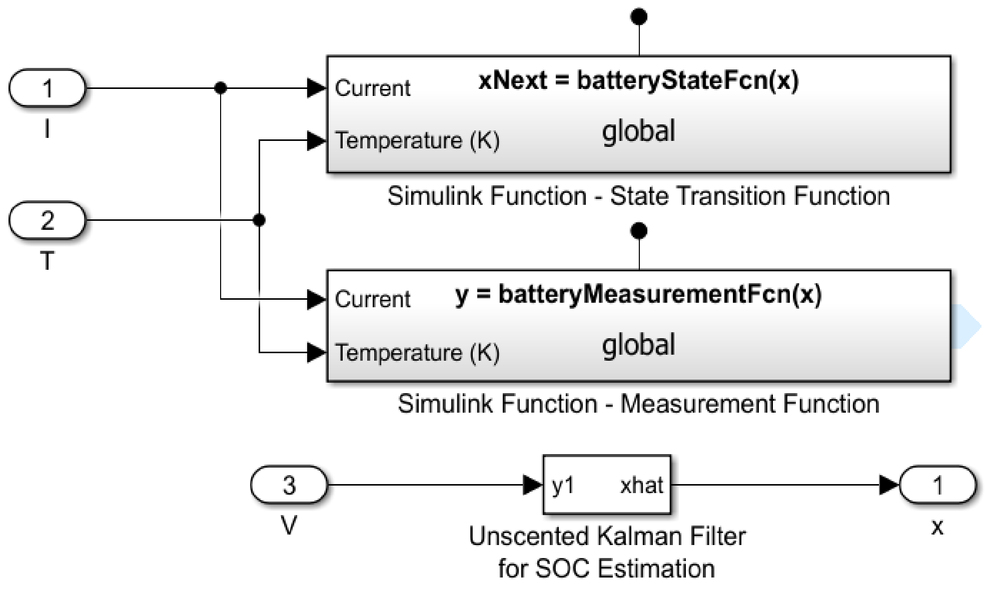

Figure 3. 29 MATLAB model for unscented Kalman filter based battery soc estimation

```
function xdot = fx(x,R1,R2,R3,t1,t2,t3,Cq,I)
xdot = zeros(size(x));
U1 = x(2);
U2 = x(3);
U3 = x(4);
xdot(1) = -I/(3600*Cq);
xdot(2) = -1/t1*U1 + I/(t1/R1);
xdot(3) = -1/t2*U2 + I/(t2/R2);
xdot(4) = -1/t3*U3 + I/(t3/R3);
```

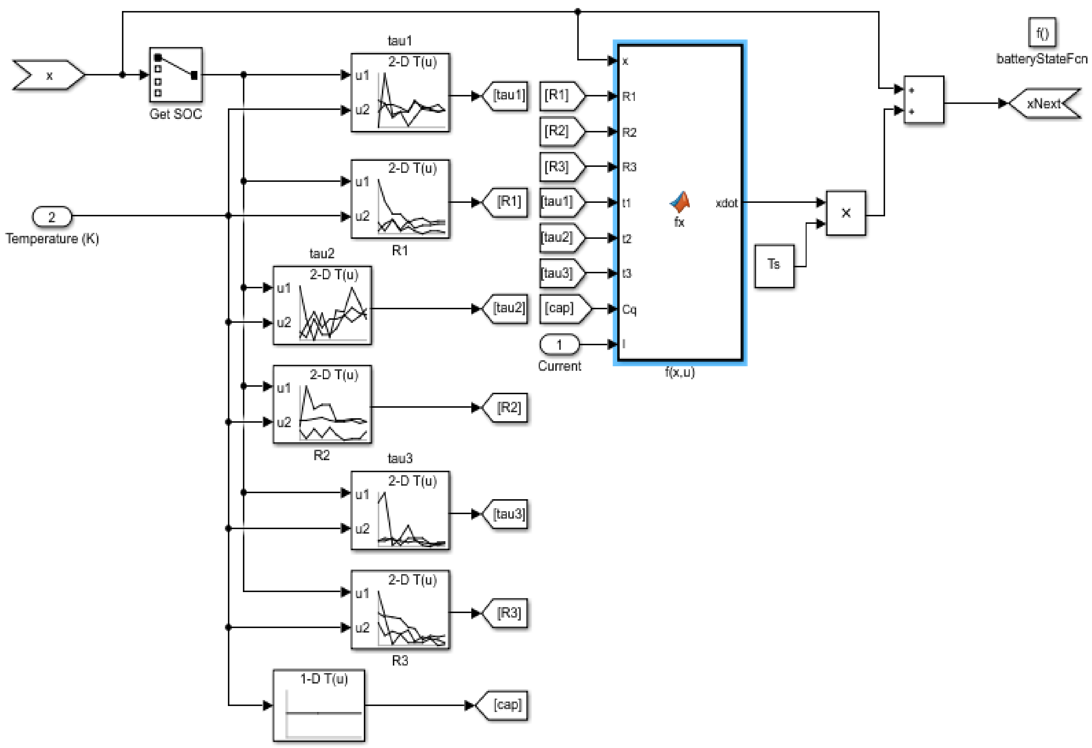

Figure 3. 30 state transition function

Inside the block which is marked, there is a MATLAB function shown above with state update equations for the four states. Namely SOC and the three voltages across the RC components. The measurement function calculates the terminal voltage as the deference between OCV and the sum of the individual voltage drops across the resistors of the equivalent circuit elements.

3.7.2. Battery Cell Balancing

During the design of the balancing system, it has to be determined when to balance during charge, during discharge, or both. And over what soc range to do the balancing. In this thesis, balancing is done during charging over the entire SOC range.

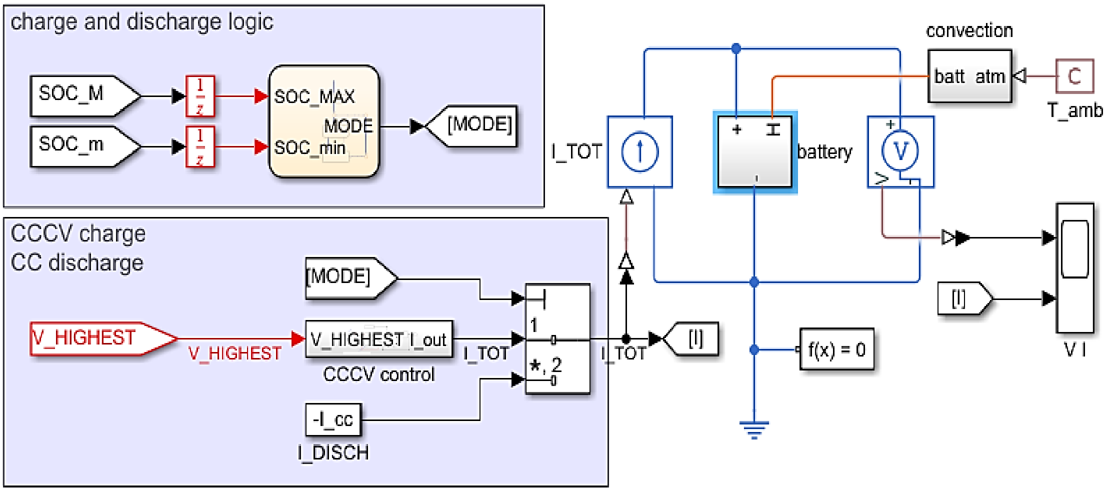

Figure 3. 31 Overall battery management system

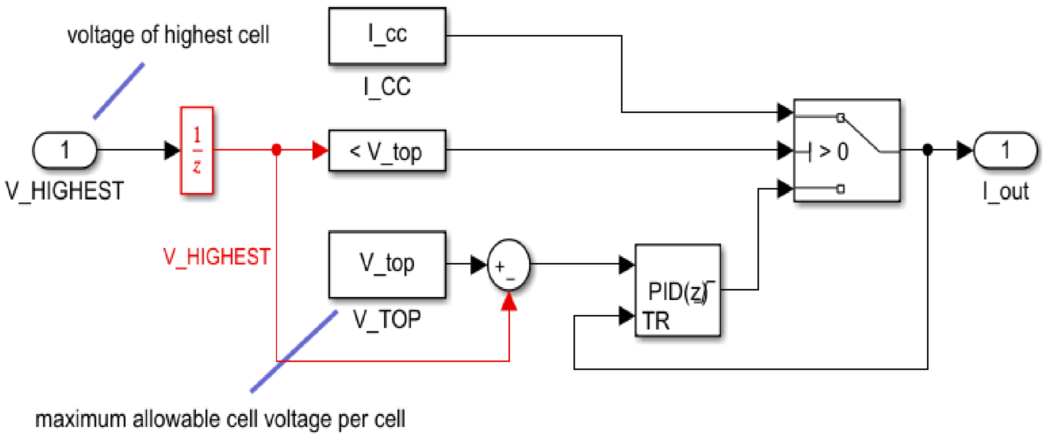

Figure 3. 32 The circuit that controls CC-CV charging

The charge controlling circuit shown in Figure 3.31 is the part of BMS which makes the charging pattern follow the CC-CV charging algorithm. On the initial charging stage, the battery cell charge in constant current and once the voltage measured across terminals reach the nominal full charge OCV value the BMS changes to constant voltage with this voltage value as a set point. Charging continues until the current reaches the predetermined lower threshold. The change from constant current to constant voltage is done with the switch shown in Figure 3.32.

Figure 3.33 represents a small battery pack with three series 1 parallel configuration. On the right, it can be seen the balancing circuit which includes resistors and transistors that selectively switch the bypass branch on and off according to the relative SOC of the battery cells. When it is appropriate the resistors divert part of the charging current by slowing down the rate of charge of the cell in which they are connected to allowing the cell below to catch up.

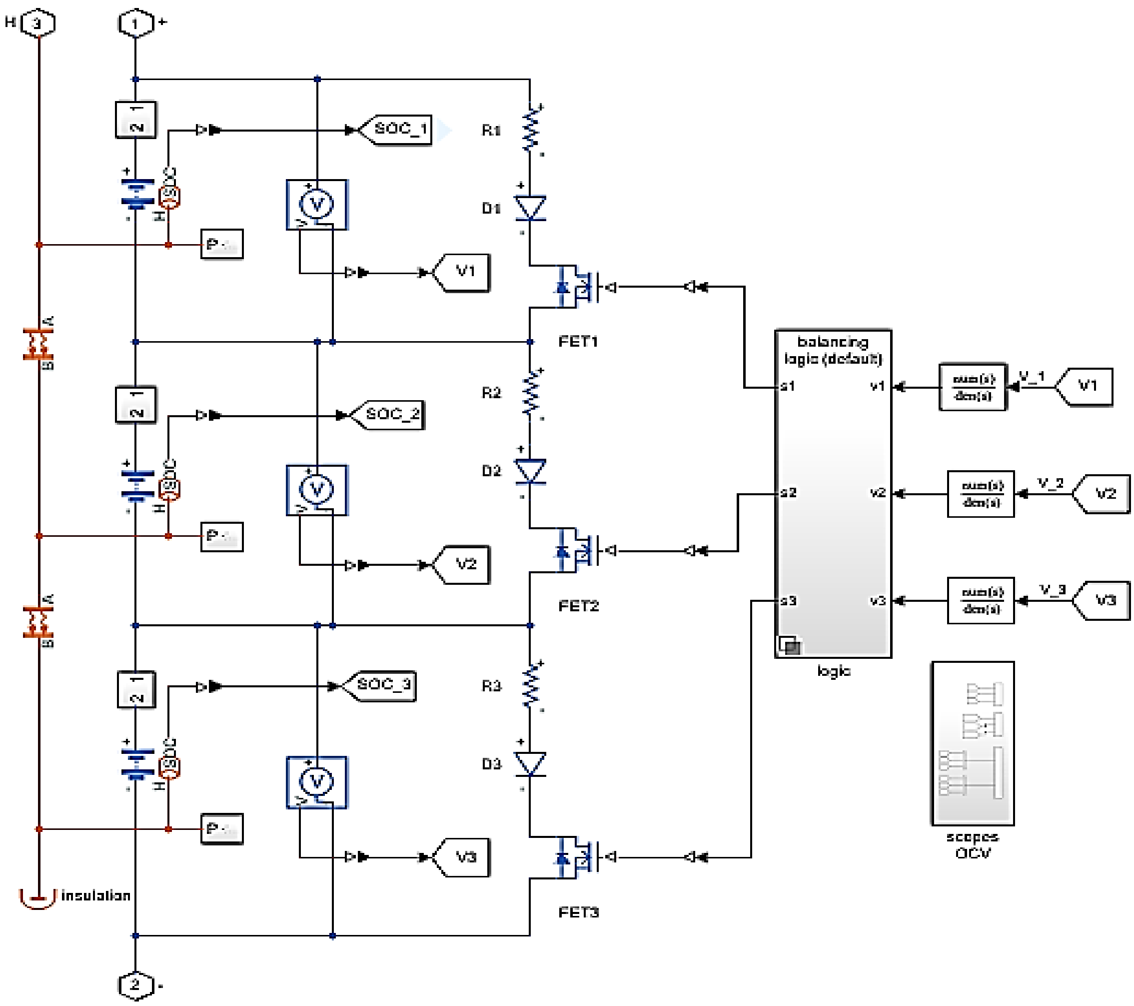

Figure 3. 33 Passive switched shunt battery cell balancing circuit

The control signals that command the MOSFET gates arrive from the logic block on the right. The orange block to the left of the cells represents convective heat transfer between cells. These blocks are connected to the thermal port of each cell and lead to the thermal part of the equivalent circuit. The heat generation is assumed to be only the result of the Joule effect. The thermal connection is asymmetrical since the cell at the bottom is thermally insulated on one side. While the cell at the top connected to the atmosphere via a convective heat transfer block.

Figure 3.34 shows the logic that controls the balancing process. State flow is an add-on library on top of Simulink specifically designed to model state logic algorithm. Each block shown in Figure 3.34 represents a state during which some variables are assigned to a certain value. In this case, those are the output signal feeding the MOSFET gate. Based on OCV values corresponding to each cell, a MATLAB function sorts them based on their relative SOC, and state flow decide which MOSFET to activate and slow down the charging of that cell.

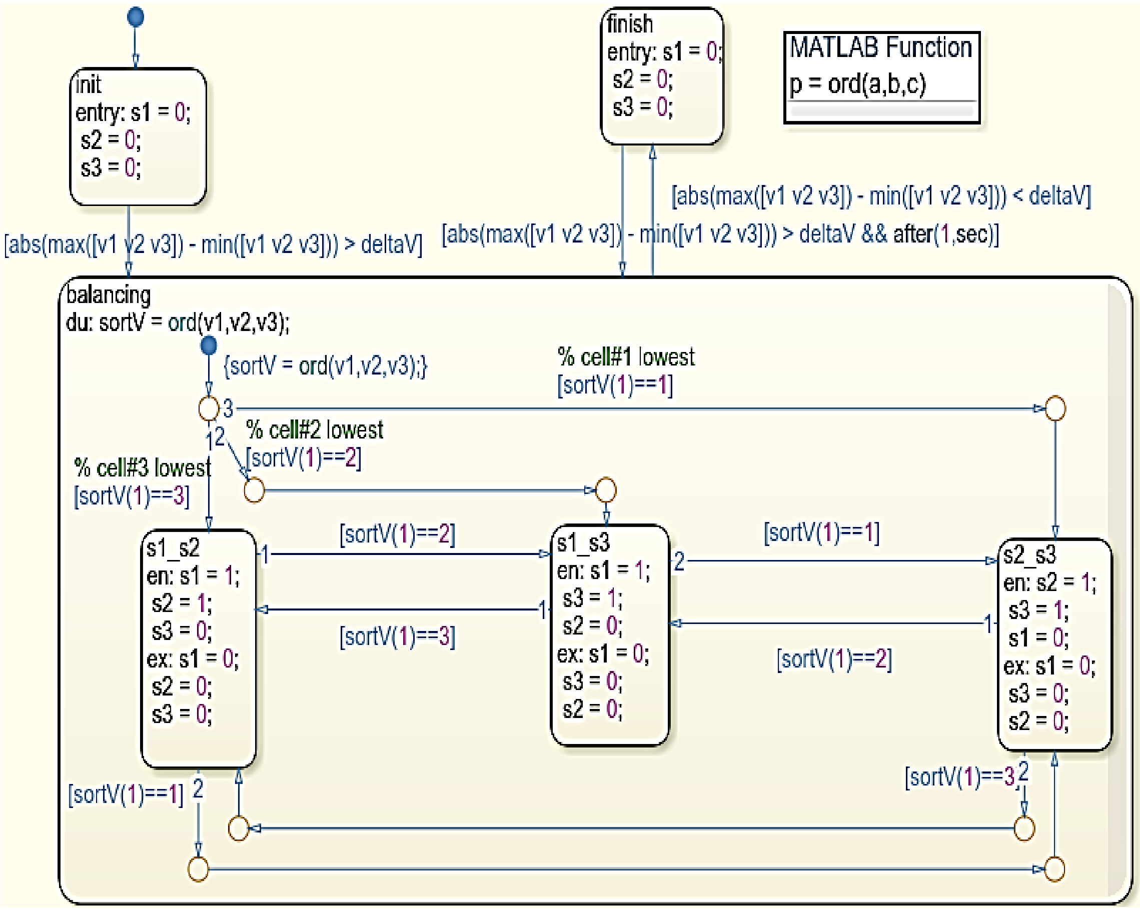

Figure 3. 34 Developed balancing logic algorithm

3.8. Battery Specifications

All high voltage battery packs are made up of battery cells arranged in strings and modules. A battery cell can be regarded as the smallest division of the voltage. Individual battery cells may be grouped in parallel and/or series as modules. Further, battery modules can be connected in parallel and/or series to create a battery pack. The total battery pack voltage is determined by the number of cells in series. To increase the current capability of the battery capacity, more strings have to be connected in parallel.

Table 3.3 and Table 3.4 shows the specifications of an ECADO-4EV traction motor and battery pack that is taken from the proposal.

Table 3. 3 Tractive motor and vehicle specification taken from ECADO-4EV proposal

Parameters	Values
Maximum power (KW)	100
Gross weight (kg)	1500
Rated power (KW/rpm)	60/3600
Maximum torque (NM/rpm)	320/1978
Rated torque (NM/rpm)	159.23/3600
Maximum speed (Km/hr.)	130
Rated speed (km/hr.)	100
Range (km/charge)	40
Seating capacity (person)	4

Table 3. 4 Battery specifications used [ECADO-4EV]

Parameters	Value[unit]
Cell type	Lithium iron phosphate
Total battery energy usage	32KWh
Rated DC voltage supply	360V
Capacity	90Ah
Dimension (W*D*H)	52*225*231cm
Energy density	154Wh/kg
Operating temperature	-10 to 50℃
Battery charging voltage range	320 to 420V

Battery pack calculations are performed as follows. From given specifications of ECADO-4EV. The maximum speed of the car is V_{EV} =130km/hr. Energy usage can be calculated as:

$$E = P * T \tag{3.32}$$

where T is the time taken to cover the given range at maximum speed.

$$T = \frac{D}{V} \tag{3.33}$$

where D is the driving range per one-time charge and V is the maximum speed that the car can be driven.

$$T = \frac{40km}{130km/hr.} = 0.32hr \tag{3.34}$$

From Equation, the total energy usage can be calculated as

$$E = 100kW * 0.32hr = 32kWh \tag{3.35}$$

The lithium-ion battery cell selected for this work has the nominal voltage and nominal capacity of 3.7V and 1500mAh (1.5Ah.) respectively as shown in Appendix E. The nominal battery voltage of ECADO-4EV given as 360V.

Therefore, the nominal capacity of the battery pack can be calculated as

$$Nominal\ capacity\ (Ah) = \frac{Energy\ usage}{nominal\ battervoltage}$$

$$= \frac{32kWh}{360V} = 88.9 = 89Ah \tag{3.36}$$

The battery pack is composed of battery cells which are connected in series and parallel to meet the specified voltage and Ah capacity. Total number of cells calculated as:

$$Total\ number\ of\ battery\ cell = \ cells\ in\ parallel * cells\ in\ series \tag{3.37}$$

Battery cells connected in series are mainly designed to achieve the nominal voltage of the battery pack. The number of series cells can be calculated as

$$Number\ of\ cells\ in\ series = \frac{nominal\ voltage\ of\ the\ battery\ pack}{nominal\ voltage\ of\ the\ battery\ cell}$$

$$= \frac{360}{3.7} = 97.3 = 98 cells \tag{3.38}$$

On the other hand, battery cells are connected in parallel to increase the Ah capacity of the battery pack.

$$Number\ of\ cells\ in\ parallel = \frac{nominal\ capacity\ of\ the\ battery\ pack}{nominal\ cell\ capacity} \tag{3.39}$$

$$= \frac{89}{1.5} = 59.3 \quad = 60\ cells$$

From Equation (3.38) and (3.39), the total number of cells required to construct the propose Electric vehicle will be

$$Number\ of\ cells\ in\ series * Number\ of\ cells\ in\ parallel \quad = 98 * 60$$
$$= 5880\ cells$$

Another parameter that must be considered in calculating the battery pack parameters is charging time. Charging time is the time that takes to fully charge a battery pack which can be calculated as

$$Charging\ time = \frac{nominal\ capacity\ of\ the\ battery\ pack(Ah)}{charging\ current(A)} \tag{3.41 }$$

$$= \frac{89}{18.1} = 4.92 hr.$$

From the above calculation, the ECADO-4EV battery pack is charged fully in 4 hrs and 55 minutes by using the proposed charger.

3.8.1. Designing a 7.6 kW EV Charger

In this section, the design considerations for an interleaved boost and LLC resonant converter based EV charger based on the design considerations discussed above. The design considerations are provided for a level-2 charger rated at 7.6 kW. It is aimed to charge a Li-ion battery with 360 V nominal voltage from depleted (320V) to fully charged (420) conditions. The charging process is divided into constant current (CC) and constant voltage charging (CV) stages.

3.8.2. Charging Profile of The Li-ion Battery

Figure 3.35 provides the charging characteristics of a single Li-ion battery cell. The nominal voltage of the battery is 3.6 V. Based on the charging data of a single battery cell, the charging profile of a Li-ion battery pack could be obtained, as plotted in Figure 3.36.

According to Figure 3.36, there are four key points in the charging process.

1) *Begin point:* Begin point corresponds to the lowest stage of charge. At this point, the battery pack has the minimum voltage (320 V). The charging current equals to 18.1 A. The equivalent load resistance which corresponds to the battery charging power of 5.8 kW is calculated as 17.7 Ω.
2) *Nominal point:* The voltage is equal to the nominal voltage (360 V) while the charging current still equals to 18.1 A. The corresponding load resistance at 6.5 kW is 19.9 Ω .

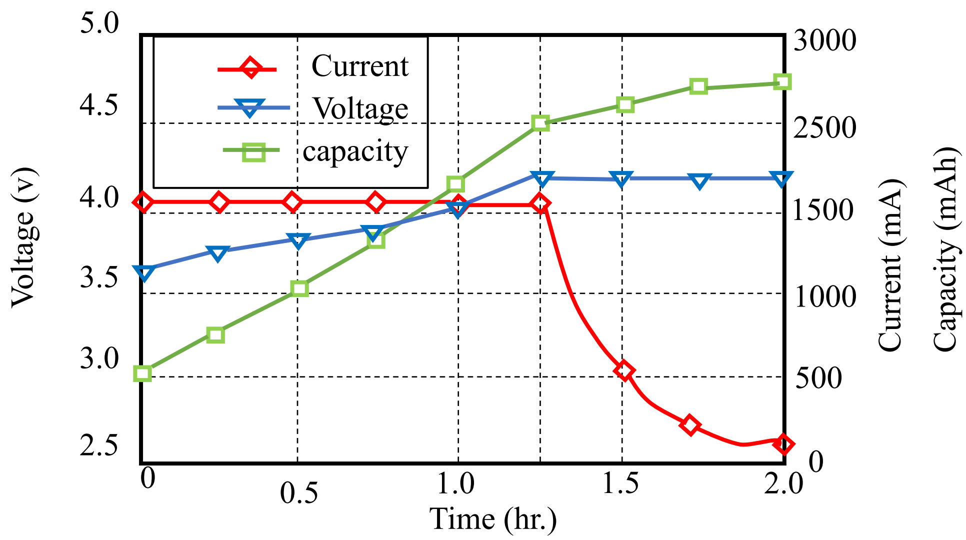

Figure 3. 35 Charging characteristics of a Li-Ion battery cell.

3) *Turning point:* Turning point is the intersection between CC charging and CV charging modes. The voltage is 420 V, and maximum power (7.6 kW) is achieved at this point. The charging current is still 18.1 A. The equivalent load resistance is 23.2 Ω .
4) *Endpoint:* Endpoint marks the end of the constant voltage charging and also the end of the whole charging process. The load resistance corresponds to 420 Ω . The

corresponding quality factors at different operating points could be calculated from Equation (3.42).

$$Q = \frac{\sqrt{L_r/C_r}}{8n^2/\pi^2 * R_L} \tag{3.42}$$

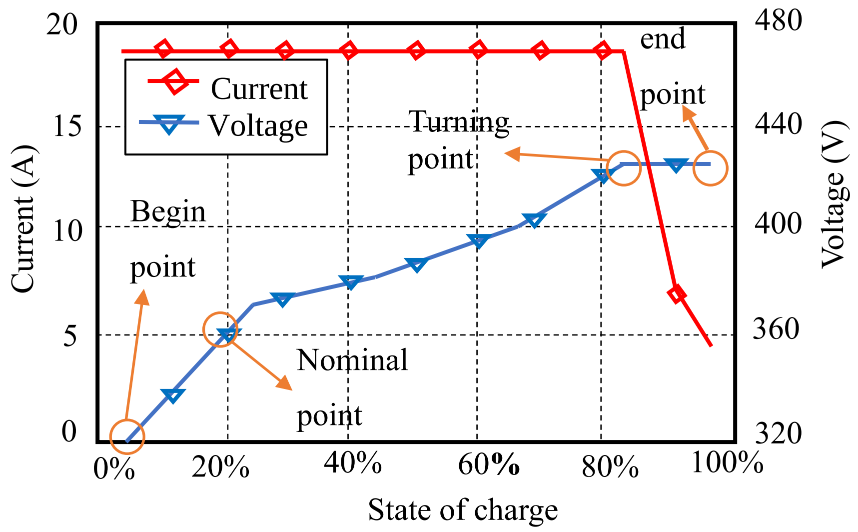

Figure 3. 36 Charging profile of the Li-Ion battery pack.

3.8.3. Interleaved Boost PFC Converter Design

In PFC boost converter, the instantaneous duty cycle d varies with the input voltage as,

$$d(\theta) = 1 - \frac{325.27|sin\ \theta|}{V_{DC}} \tag{3.43}$$

where 325.27 V is the peak input voltage, and θ is the phase angle between the input voltage and current. The inductor current ripple can be expressed as,

$$\Delta I_L = \frac{|V_{in}|}{L} d(\theta) T_s = \frac{325.27 T_s}{L}\left(|\sin\theta| - \frac{325.27}{V_{DC}}(\sin\theta)^2\right) \tag{3.44}$$

Assume $x = |\sin\theta|$, then $0 \le x \le 1$. The derivative of ΔI_L is calculated as Equation (3.45)

$$\frac{d\Delta I_L}{dx} = \frac{325.27\ T_s}{L}\left(1 - \frac{650.54}{V_{DC}}x\right) \tag{3.45}$$

According to Equation (3.45), if $V_{DC} \leq 650.54$ V, the peak ripple happens when $x = V_{DC}/650.54$. Substituting x into Equation (3.43), d is calculated as 0.5. If $V_{DC} > 650.54$ V, the peak ripple happens when $x = 1$ and $\theta = \pi/2$. Based on the previous analysis, the duty cycle close to 50% provides the best inductor current ripple cancellation, as well as RMS capacitor current cancellation.

Conventionally, the dc-link voltage of grid-connected front-end AC-DC converter, V_{DC}, has the typical value to be 390 V. However, in this work, V_{DC} is designed to be 600 V. This is because $V_{DC} = 600$ V has overall duty cycles closer to 0.5 and better ripple cancellation effect, which could be observed in Figure 3.37.

The circuit is designed to operate at 100 kHz switching frequency taking the tradeoff between the sizes of the inductors and dc-link filter capacitor and switching losses into account. The inductor ripple current at the peak of line ($\theta = \pi/2$) is designed to be 30% of the inductor current.

$$\Delta I_{L\,max} = \sqrt{2} I_{L\,rms} * 0.3 = \sqrt{2}\frac{p_{max}}{2V_{in,rms}} * 0.3 \tag{3.46}$$

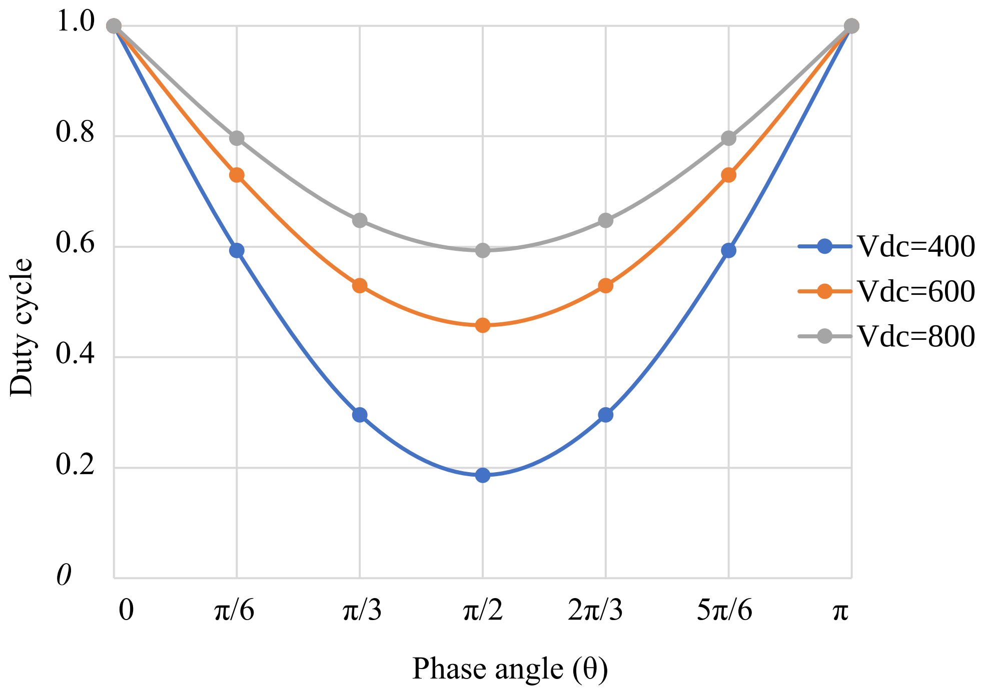

Figure 3. 37 Duty cycles corresponding to different DC link voltages

According to Equations (3.46) and Equation (3.44), inductances could be calculated as:

$$L_1 = L_2 = \frac{T_s V_{in,rms}}{\Delta I_{L\,max}} d\left(\theta = \frac{\pi}{2}\right) \tag{3.47}$$

The ripple voltage at the dc-link capacitor is set to be 5% of the dc-link voltage, which is 30 V. Based on this ripple voltage, the dc-link capacitance could be calculated,

$$C_{DC} = \frac{2P_{max}}{2\pi V_{DC} V_{ripple} 2f_{line}} \tag{3.48}$$

In this design, the inductances and capacitance are calculated as 212.7µH and 1.3mF, respectively.

3.8.4. Full-Bridge LLC Converter Design

f_p and f_s are the two resonance frequencies of the LLC resonant tank. When the switching frequency, f, is higher than f_p, the resonant tank becomes inductive. When the f is lower than f_s, the resonant tank becomes capacitive. In between f_s and f_p, inductive or capacitive operation region is determined by the load. On the other hand, as the switching frequency is varied closer to f_p, the impedance of the resonant tank becomes smaller. This can reduce the circulating energy in the resonant tank, which results in reduction in the conduction losses of the LLC converter. Therefore, the LLC converter is desired to operate in the inductive region and close to f_p for minimizing switching and conduction losses and maximizing efficiency.

For design considerations, f_p is preset by the optimum operating frequency of the MOSFETs, considering the tradeoff between high-frequency operation and switching power loss. Thus, the product of L_r and C_r can be determined as the initial design step. Short circuit performance ($Q = \infty$) and peak voltage gain at maximum output power ($Q = Q_{turn}$) are two important considerations in designing L_r and C_r. When the short circuit happens, the power management module shifts the switching frequency to a higher value (2 ~ 3f_p) to increase the impedance of the resonant tank, hence, the short circuit current could be effectively reduced and limited to a predetermined value. If L_r is large, the resonant tank impedance becomes large as well, while the short circuit current becomes smaller. However, for a constant f_p, a larger L_r would result in a smaller C_r, which increases the voltage stress of the resonant capacitor as well as the quality factor. The increase of quality factor reduces the peak voltage gain. This might cause potential failure to fulfill the voltage gain specification at heavy load condition. The values of L_r and C_r are determined based on this tradeoff.

Based on those two design tradeoffs, the DC-DC stage parameters can be designed.

1) Selection of the turn's ratio of transformer

The transformer turns ratio is determined by the ratio between dc link voltage and the nominal voltage of the battery pack,

$$n = \frac{V_{DC}}{V_{nom} + 2V_d} \tag{3.49}$$

Where V_d is the voltage drop across the diode.

2) Selection of L_r and C

The primary resonance frequency was determined as f_p = 200 kHz. According to Equation (3.50) the product of L_r and C_r can be found as,

$$\sqrt{L_r C_r} = {}^{1}\!\big/\!\left(2\pi f_p\right) \tag{3.50}$$

As aforementioned, there is a tradeoff between the peak voltage gain at heavy load and the short circuit current. In this case, the peak voltage gain at the turning point is the heaviest load condition in CV charging mode. The voltage gain must be larger than 420/360 = 1.17. The short circuit current should be smaller than the maximum current of the charger (18.1 A). Based on this tradeoff, the optimal quality factor at the turning point Q_{turn} is tuned to be 0.94, which satisfies the peak gain voltage and short circuit current requirements. Thus, the ratio between L_r and C_r can be determined by Equation (3.51)

$$\sqrt{L_r C_r} = Q_{turn} * \frac{8n^2}{\pi^2} * 23.3\Omega \tag{3.51}$$

From Equations (3.50) and (3.51), L_r and C_r could be calculated as 33.17µH, and 18.7nF, respectively.

3) Selection of the magnetizing inductance L_m

The design of L_m is based on the tradeoff between conduction and switching losses. Decreasing L_m would increase the resonant tank current at the instant of a turnoff as well as the switching losses. While the increase in L_m would reduce the impedance of L_m and increase the circulating energy in L_m. Different values of L_m are investigated through evaluating circulating energies in the resonant tank and turning off currents. The optimal magnetizing value is determined as 92.17 μH.

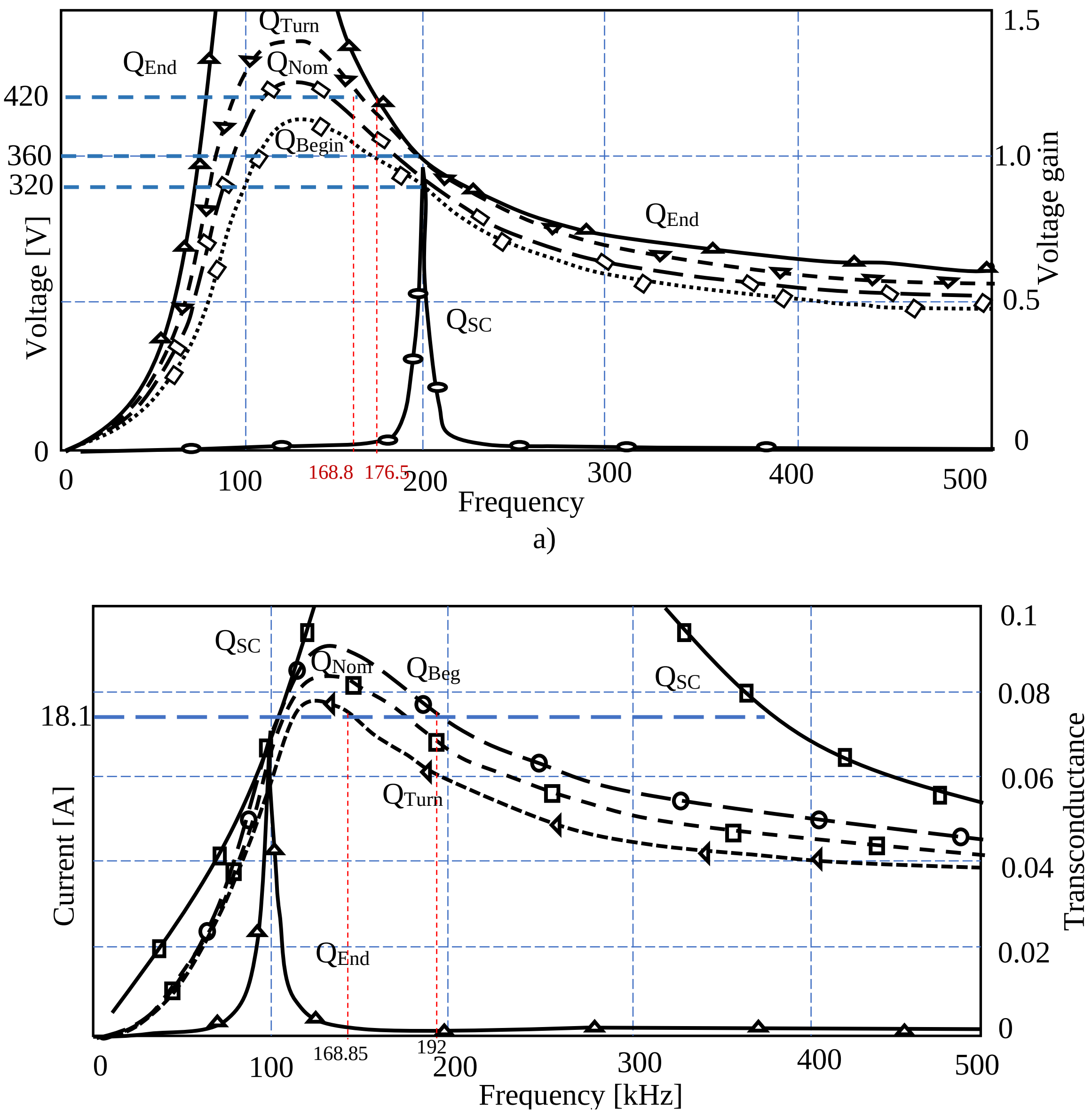

Figure 3. 38 Dc characteristics of the designed 7.6kW LLC converter: a) voltage characteristic b) current characteristic

Voltage and current curves using the determined L_m and L_r parameters, which correspond to the begin point, nominal point, turning point, and end-point are plotted in Figure 3.38.

According to Figure 3.38 (a), in CV charging mode, the output voltage is constrained at 420 V which is the fully charged battery pack voltage. From the turning point to the end-point, the switching frequency increases from 168.85 kHz to 176.5kHz. In CC charging mode, the charging current is constrained at 19.1 A. From the begin point to the turning point, the switching frequency decrease from 192 kHz to 168.85 kHz.

Table 3. 5 Summary of parameters used in the design of an interleaved boost and full-bridge LLC resonant converter-based Li-ion battery onboard charger.

Quantity or Device	Symbol	Parameter
Input voltage	V_{in}	230V,50Hz
Dc link voltage	V_{dc}	600V
Interleaving inductor	L_1, L_2	212.7µH
Dc link capacitor	C_{dc}	1.3mF
Switching frequency for PFC stage	f_{pfc}	100kHz
Battery voltage range	V_b	320V to 420V
Rated maximum power	P_{max}	7.6kW
Primary resonant frequency	f_p	200kHz
secondary resonant frequency	f_s	100kHz
Transformer turn ratio	N	2
Magnetizing inductor	L_m	92.17µH
Resonant inductor	L_r	33.17µH
Resonant capacitor	C_r	18.7nF
Output filter capacitor	C_f	50µF

CHAPTER 4

RESULT AND ANALYSIS

4.1. Chapter Review

This chapter includes the result and analysis of the proposed interleaved boost and LLC multi resonant converter based onboard electric vehicle battery charger. The simulation result of the proposed system is analyzed and compared with the expected result. The simulation result provided in this chapter has the same value as those which are used in the study. But for the battery management system, only three cells connected in series are used to demonstrate how the battery management system need to be model for the battery pack of the electric vehicle.

In this research work, MATLAB/Simulink/Simscape is used to model the overall charger and battery management system. on the charger, the simulation result of the interleaved boost converter mainly shows how the converter maintains harmonics and power factor while charging high voltage battery of the electric vehicle. Also, the simulation result of the back-end LLC converter is analyzed on different battery voltage since battery voltage varies with the state of charge. Results related to the battery management system will demonstrate how developed algorithms control end estimate parameters in the charging process of a lithium-ion battery pack. Finally, other related simulation results are addressed in this chapter.

4.2. The Proposed Electric Vehicle Charger Results

In this work, an interleaved boost converter and LLC resonant converter based electric vehicle battery charger is proposed. The results are discussed in detail in the following sections.

4.2.1. Front-end Interleaved Boost Converter Results.

The waveforms and results obtained in the first stage interleaved boost converter are presented in Figure 4.1 to Figure 4.3. According to Figure 4.1, the output voltage of the interleaved converter is maintained at 600V to make the duty cycle near to 0.5 and to have better inductor current cancelation. On the other hand, the input current is in phase with the input voltage. This makes the charger have a 0.9998(unity) power factor as shown in Figure 4.2.

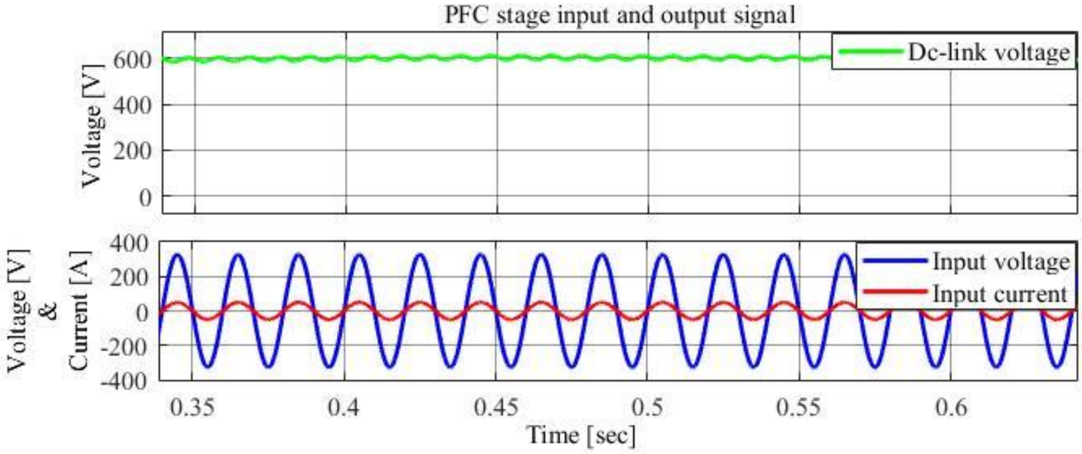

Figure 4. 1 Interleaved converter input voltage, current and output voltages

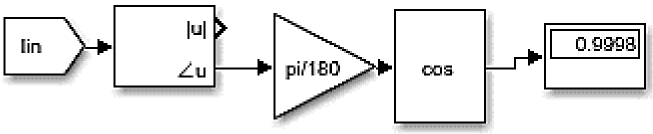

Figure 4. 2 Power factor of the charging system.

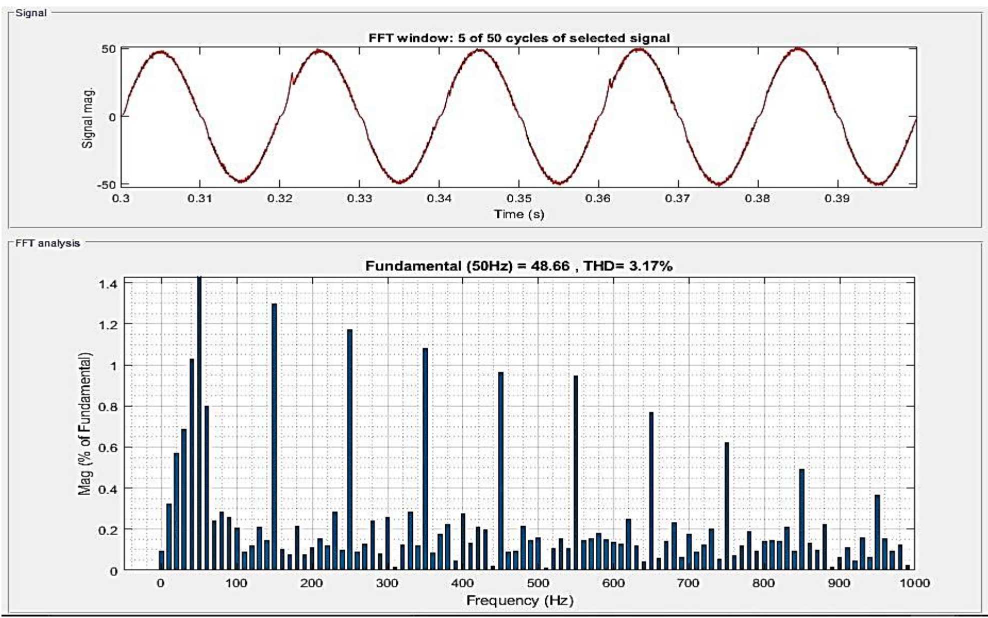

Figure 4. 3 Total harmonic distortions of the charger.

Total harmonic distortion is another factor that needs to be considered in modeling a charging system. total harmonic distortion is how much the noise affects the fundamental input current. according to IEEE std 519-2014, the recommended values for acceptable harmonic distortion is 5%. For the modeled electric vehicle charger 3.17% harmonics is achieved as shown in Figure 4.3.

4.2.2. Back-end LLC-Resonant DC-DC Converters Results

MATLAB simulation of an onboard lithium-ion battery charger which has an output voltage range of 320-420 V and maximum output power of 7.6KW is performed. The rated output voltage $V_{dc\text{-}link}$ of the interleaved boost converter is given to the LLC resonant converter and the waveforms related to the back-end converter will be discussed as follow. Pulse frequency modulation is used to control the output voltage variation of the converter by varying the switching frequency. It can be seen from the Figures below, when the switching frequency of the converter varies the output voltage, resonant current and voltage will vary with it.

As shown in the Figures below the waveforms at starting, nominal and turning point of charging are analyzed as follow.

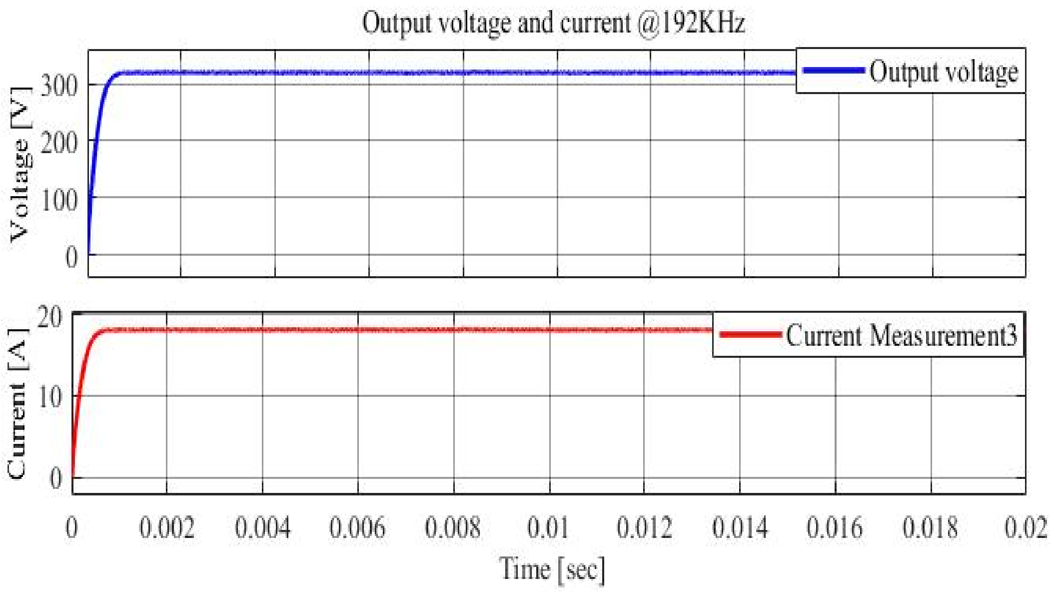

Figure 4. 4 output voltage and output current @192KHz

The resulting waveform shown in Figure 4.4 indicates that at beginning of the charge the switching frequency must near the secondary resonant frequency. At 192 kHz the converter gives us 320V with a current of 18.1A.

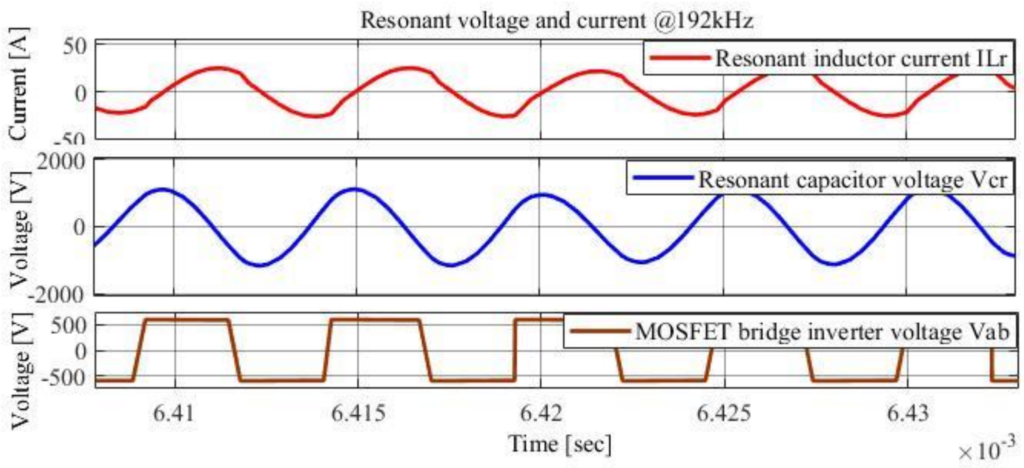

Figure 4. 5 Resonant circuit voltage and current at 192kHz

As can be seen from Figure 4.5 the waveform of the resonant inductor current, resonant capacitor voltage, and MOSFET bridge inverted voltage. even if the converters operating in light load condition it is operating in the inductive region since resonant inductor current i_{Lr} leads the resonant capacitor voltage V_{cr}. I_{Lr} can always lag behind V_{ab}. In this situation, when one switch is turned on, the resonant current flows through the antiparallel body diode, the drain-source voltage is clamped to zero, and ZVS can be realized which reduces the switching losses.

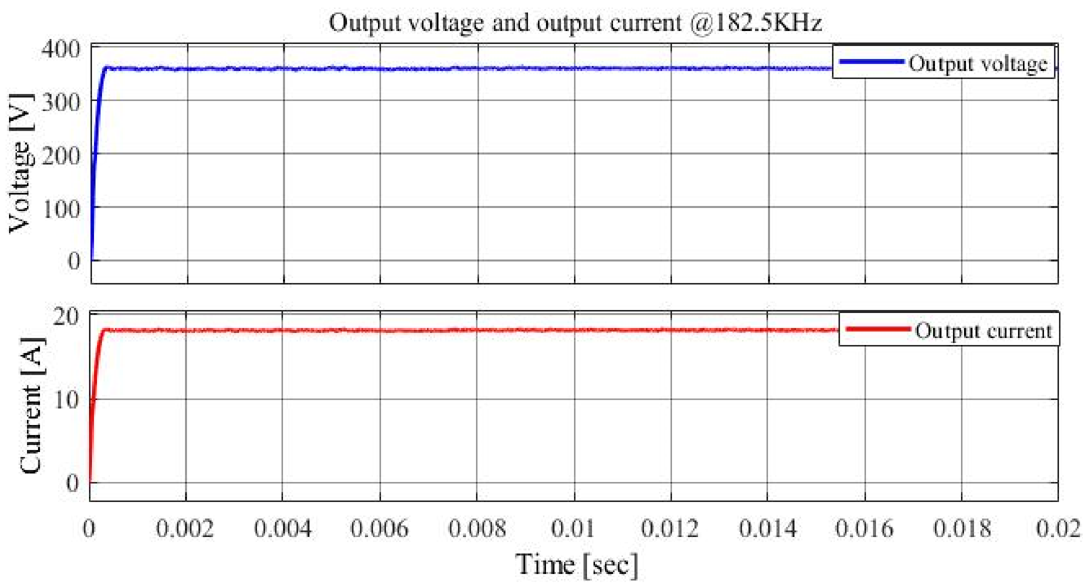

Figure 4. 6 output voltage and output current @ 182.5 kHz

Figure 4.6 indicates the output voltage and current of the LLC converter @182.5 kHz and as it can be seen in Figure the converter is giving the nominal voltage of a battery pack with its charging current of 18.1A. the nominal voltage of the battery pack is maintained with a constant charging current.

The waveform shown in Figure 4.7 demonstrates that the resonant inductor current, resonant capacitor voltage, and bridge inverted voltage. From the Figure it can be seen the waveform is a little bit distorted due to the load is lighter than the cutoff voltage and all parameters are fixed for all load conditions. But still, the converter operates in the inductive region due to the resonant inductor current i_{Lr} leads resonant capacitor voltage V_{cr}. As discussed above here is also the inductor current i_{Lr} lags the inverter bridge voltage. It will assure ZVS since when the switching current flow through antiparallel diodes. This will reduce the switching loss.

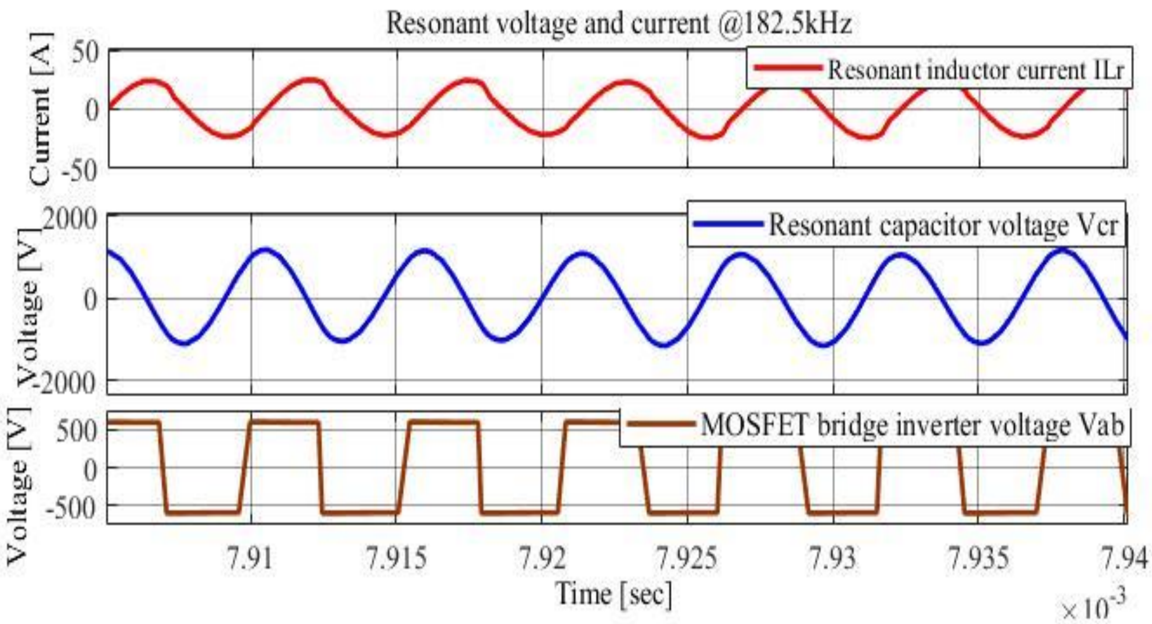

Figure 4. 7 Resonant circuit voltages and current @182.5kHz

Figure 4.8 shows the output voltage and current of the charger in which the battery charged at 90 percent of its capacity or threshold voltage. At this point the switching frequency reaches 168.85kHz and the battery will have 420V and 18.1A.

At this point of the charging time the battery management system changes the charging algorithm into a constant voltage charging. At the turning point, the power of the charger reaches its maximum.

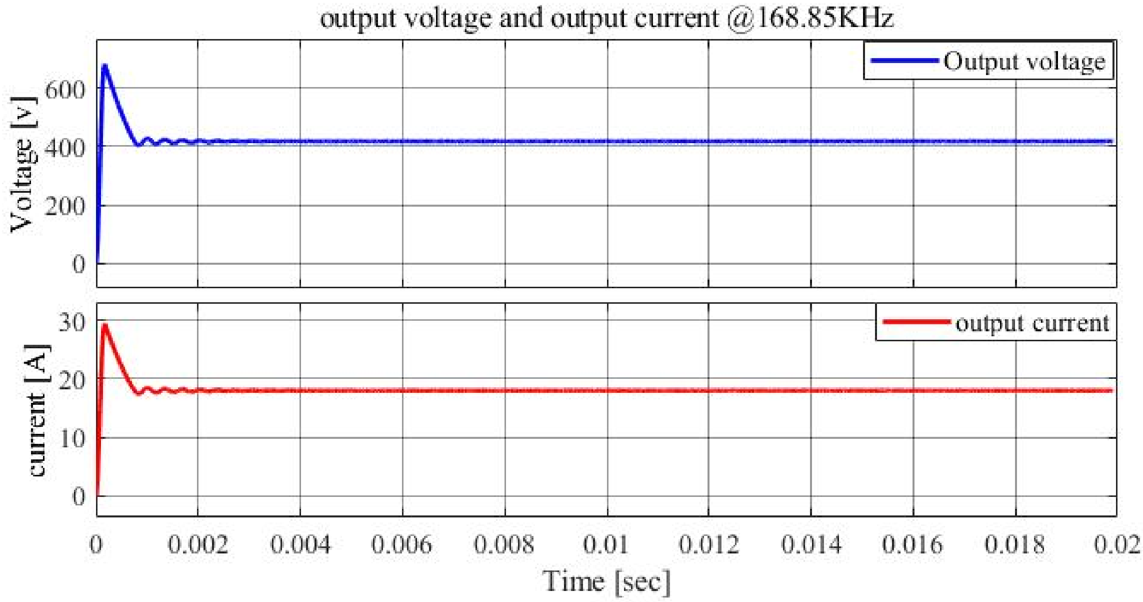

Figure 4. 8 LLC dc-dc converter output voltage and current at turning point (V_{bat} = 420V, I_{bat} = 18.1A at 168.85KHz).

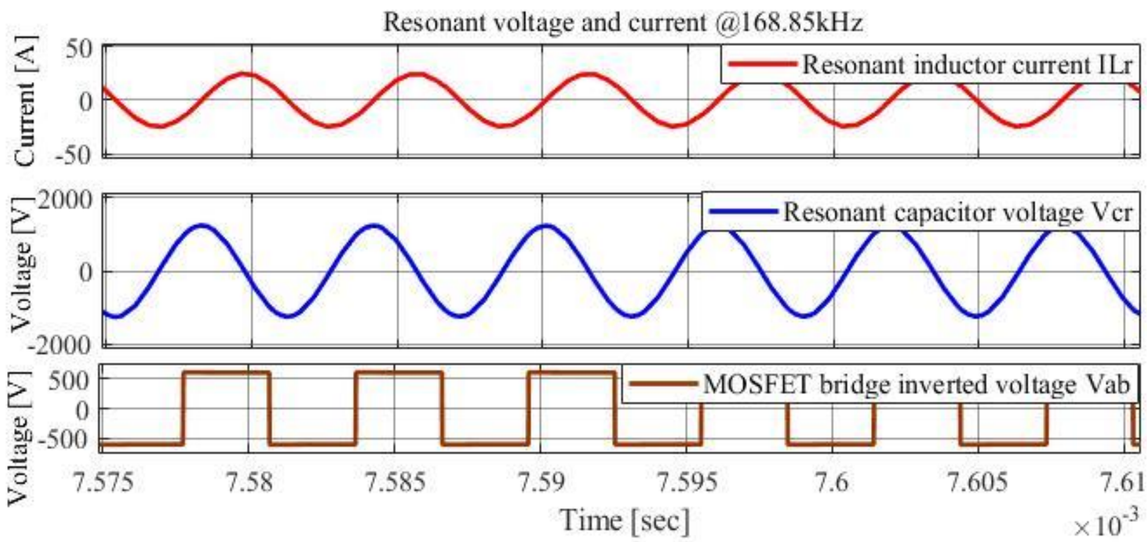

Figure 4. 9 Resonant circuit voltages and current @168.85kHz

Figure 4.9 shows the waveforms of the resonant inductor current, resonant capacitor voltage, and full-bridge inverted voltage. As dis, both the resonant inductor current and resonant capacitor voltage are close to pure sinusoidal wave, which validate the converter operate close to the primary resonant frequency. The waveforms also show that the converter operating in the inductive region where resonant inductor current I_{Lr} leads resonant capacitor voltage V_{cr}.

Figure 4.10 shows the charging voltage and current at the constant voltage region. As can be seen from the figure the voltage stays constant but the current goes to a minimum to protect the battery from overcharging. This is the charging period which charge the electric vehicle battery pack after the threshold value is achieved.

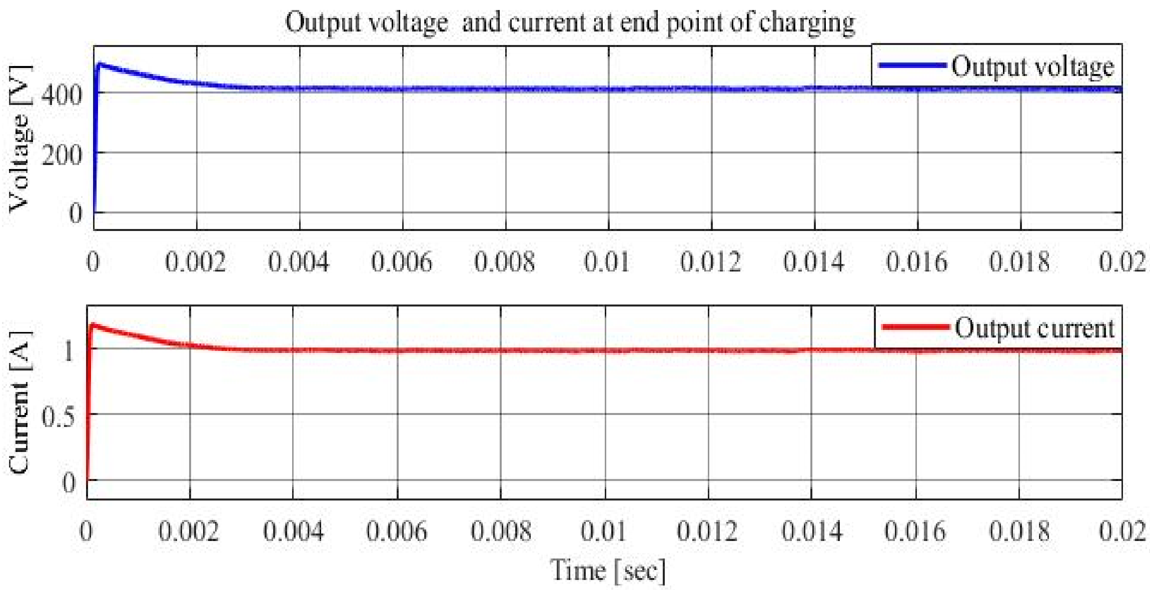

Figure 4. 10 Output voltage and current at the endpoint of the charging

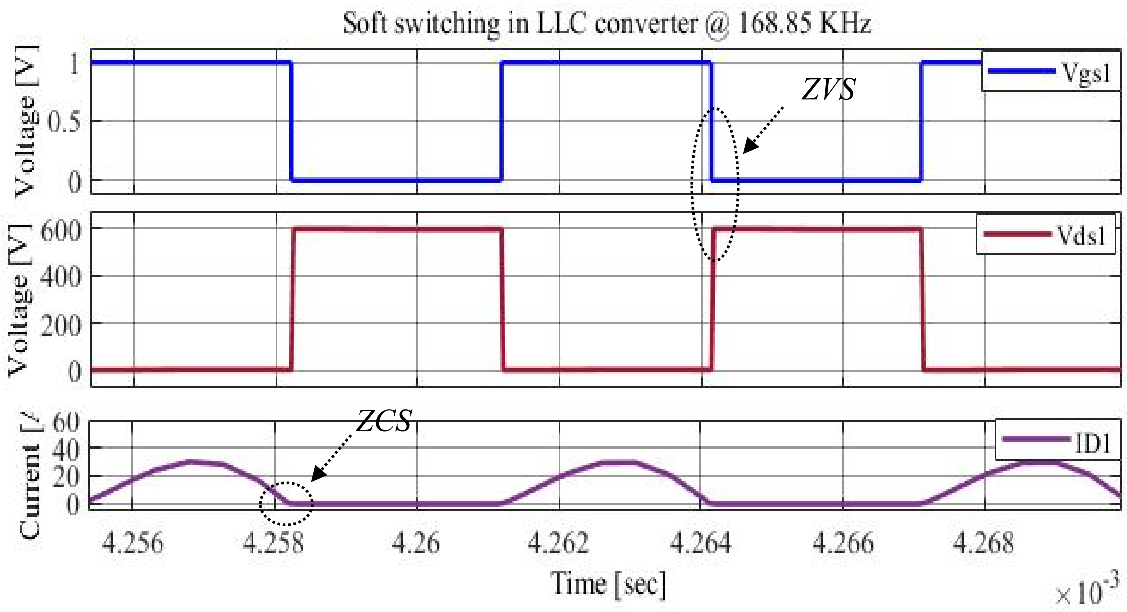

(a)

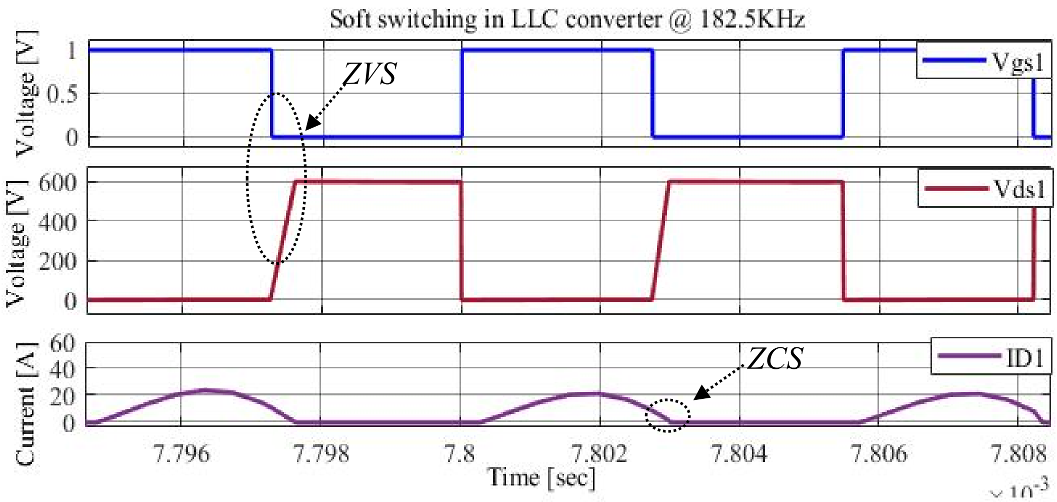

(b)

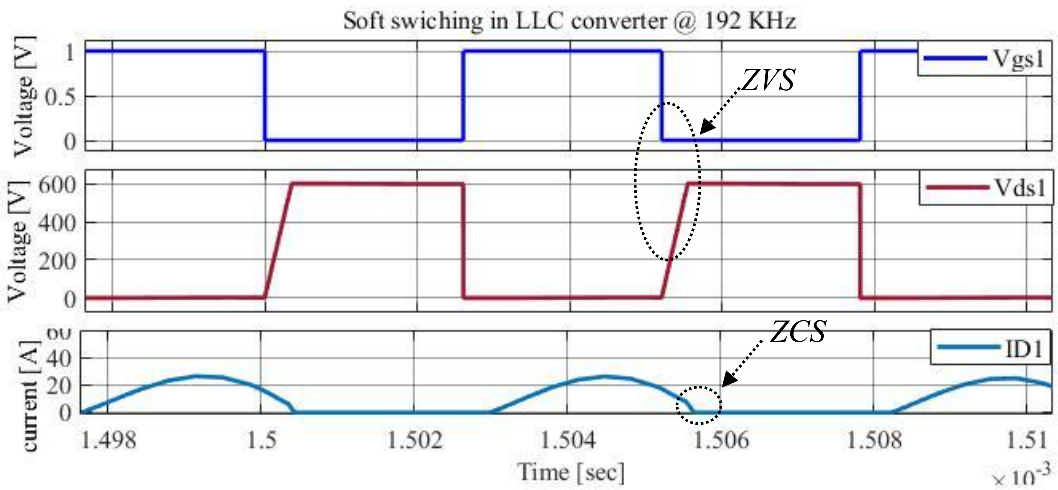

(c)

Figure 4. 11 Soft switching of LLC converter at (a) 168.85KHz and 420V (b) 182.5KHz and 360V (c) 192KHz and 320V

As shown in Figure 4.11 the drain to source voltage of the bridge MOSFET is raised after the gate to source voltage is arrived at zero for all charging cycles. So, for the overall charging cycle, ZVS is achieved during the turn-on of MOSFET. And also, from the same Figure, it can be seen that the secondary side diode bridge is turned off in ZCS.

However, when the voltage level of the battery decreased the switching frequency goes to the primary resonant frequency, which makes the diode bridge operate far from the capacitive region. In this case the in light load (beginning voltage) the diode bridge loses ZCS a little bit. But it still acceptable because it is very small and occurs for a small period of time.

And also, the switching frequency of the proposed full bridge LLC resonant converter varies from 168.85 kHz to 192 kHz. This range is close to the primary resonant frequency f_o (200 kHz), which makes the impedance of the resonant tank small. Thus, the circulating energy in the resonant tank is small, which minimizes the conduction losses.

4.3. Results Related to the Battery Management System

This section briefly describes the results of the battery management system which are closely related to charging a battery pack. As mentioned earlier in chapter three due to time constraint only three battery cells connected in series are used to demonstrate how battery management system control and estimate the parameters of the charging system.

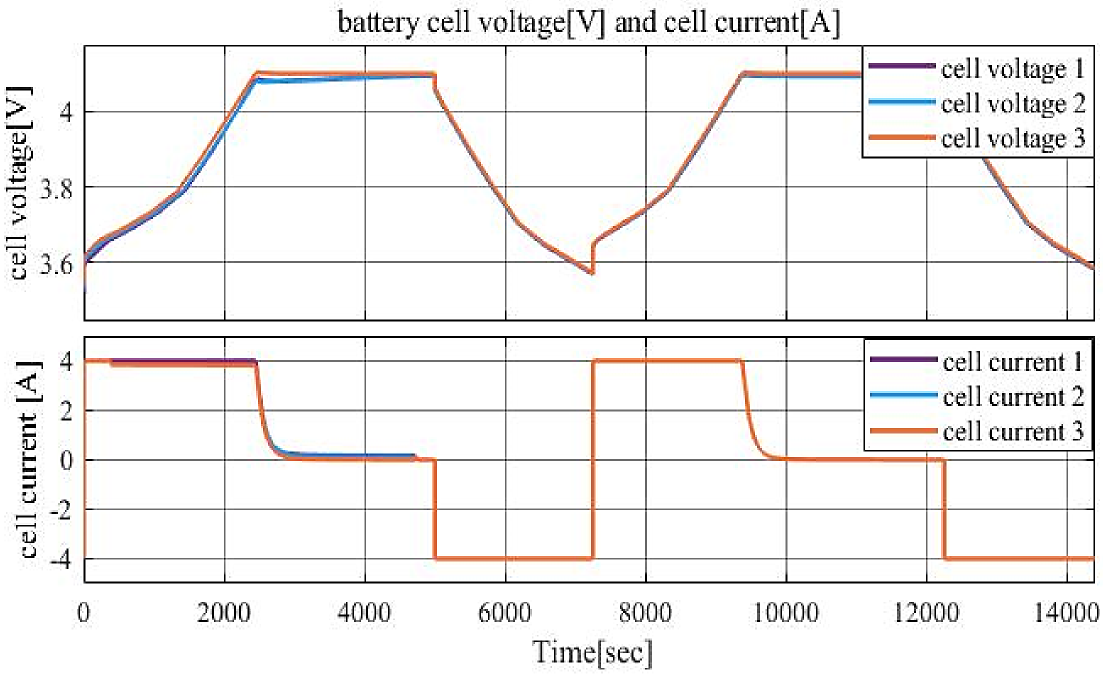

Figure 4. 12 Battery cell voltage and current

As shown above the Figure 4.12 shows the voltage and current of a li-ion battery cell during charging and discharging. The waveform shows that each cell is charging in the same manner as the pack. It starts with a constant current and after it arrives at a threshold voltage of 4.17V, the battery management its charge starts to charge the cell in constant voltage with a minimum current of 0.05A.

Temperature is another factor that has to be considered in the charging battery pack. The lithium-ion battery pack needs to operate at 0 to 45C^o during charging and -20C^o to 60C^o

during discharging. As shown in Figure 4.13 all three cells are operating under determined conditions stated above.

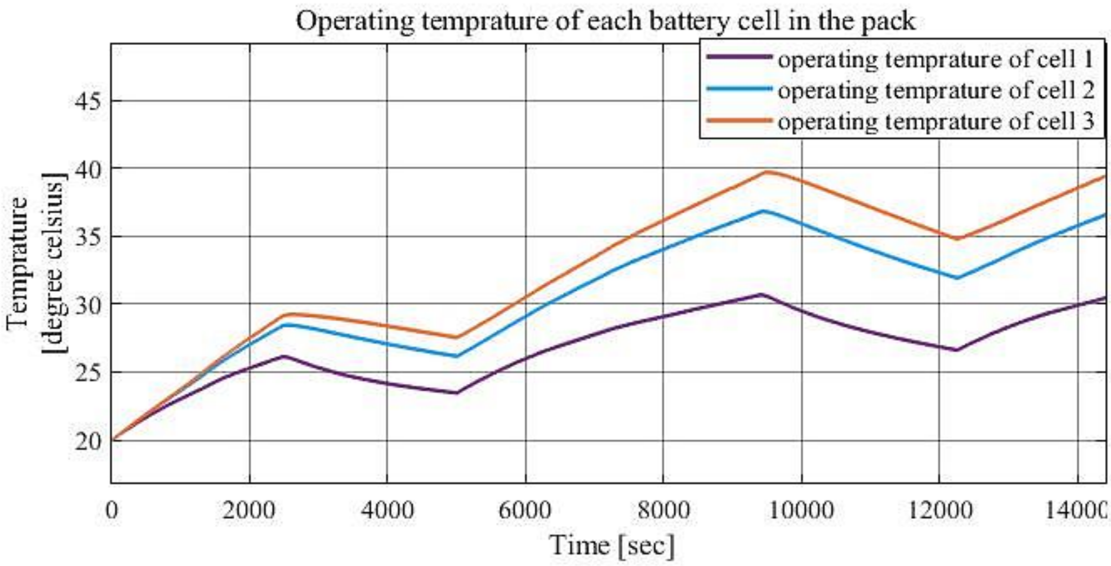

Figure 4. 13 Temperature of the battery cell during charging and discharging

Figure 4.13 clearly shows the temperature evolution of the cells. The temperature builds up is uneven because the current flowing through each resistor is not the same at each moment. the temperature is increasing because of the direct charging and discharging process. Meaning if there is a time gap between charging and discharging the temperature will be less.

Since three cells connected in series the pack will have the voltage which is the sum of all three cells and the charging current will be the same all over the pack. As shown in Figure 4.14 the pack voltage 12.3V which is the sum of all cell voltage. But the pack current is the same as the cell current.

The constant current constant voltage algorithm is seen in Figure 4.14. The charging process is started with constant current and the voltage gradually increases up to the battery fully charged. The full charge occurs when the battery reaches the voltage threshold and the current drops. A battery is also considered fully charged if the current levels off and cannot go down further.

As it can be seen from the Figure 4.14 all the characteristics of the single cell is seen in the battery pack.

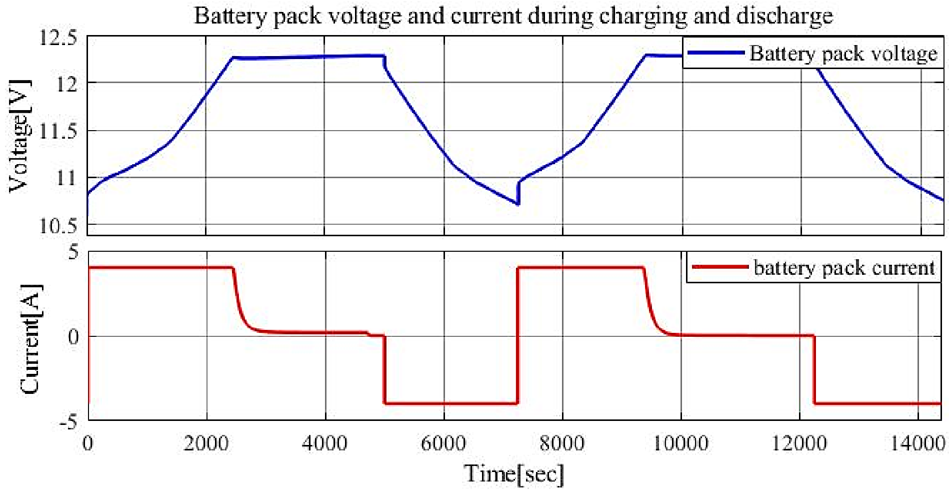

Figure 4. 14 battery pack voltage in battery management circuit

One of the key components of the battery management system is an accurate state of charge (SOC) estimation because SOC reflects battery performance. Determining the state of charge is the first step for balancing the cell capacity in the pack.

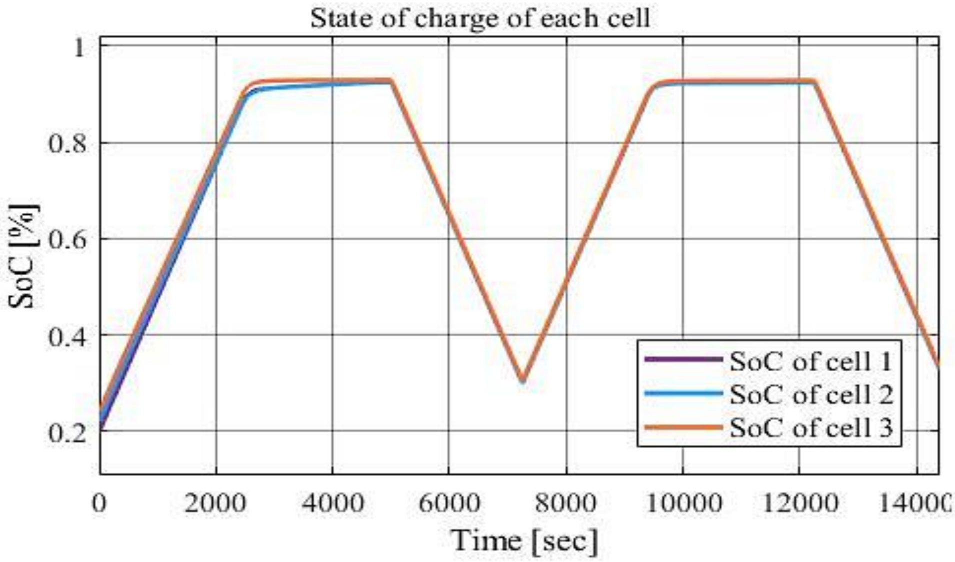

Figure 4. 15 State of charge of each battery cell in the pack

And also Figure 4.12 and Figure 4.15 shows all cells are balanced. When we see both Figures there is the voltage and state of charge mismatch in the first charging cycle but the balancing logic circuit makes all cells charge equally. As can be seen in the second cycle of both Figures all cells are balanced.

CHAPTER 5

CONCLUSIONS AND RECOMMENDATIONS

5.1. Conclusions

In this thesis, a level-2 onboard EV battery charging system is proposed. Interleaved boost topology is used in the first stage for PFC and THD reduction as well as reducing the volume of the magnetic components. In the second stage, a full - bridge LLC resonant converter is employed to achieve high conversion efficiency over the full voltage range of the battery pack. The suitability and advantages of the proposed converter are discussed and design guidelines are provided through theoretical analyses for both converter topologies. As a case study, design considerations for a 7.6 kW level-2 charger, which converts 230 V, 50 Hz AC to the battery voltage range of 320 V to 420 V are provided, considering the characteristics of the converter. Moreover, the charging profile of a 360 V battery pack is detailed to provide a guideline for the charger design.

A battery management system for three cells connected in series is also developed to show the controlling mechanisms of the charging system. Battery cell monitoring, cell voltage balancing, state of charge estimation, and other related systems are simulated in MATLAB. Finally, the simulation results are presented for validation. The first stage interleaved boost converter demonstrates unity power factor operation at the rated power and achieves THD less than 4%. In the second stage LLC converter, the switching losses and conduction losses are optimized through operating in the converter close to the resonance frequency of the resonant tank.

As shown above, the proposed onboard battery charging system can overcome the problems stated above by operating in a unity factor and making the total harmonic distortion minimum. This will stabilize the integration of the charging system with the grid. In this regards the charging system is acceptable in international standards such as IEEE std 519-2014. The back-end converter is also operating in ZVS during turn-on of the MOSFET bridge and the secondary side diode bridge operates in ZCS at the turnoff. This will reduce the losses related to switching.

The battery management system is also designed to safely charge the electric vehicle battery pack. The designed BMS shows an excellent performance in controlling the charging system. This makes the proposed system to be competitive in the research environment and can be applied for ECADO-4EV.

5.2. Recommendations

The hardware implementation of the onboard charging system using the DSP kit is recommended. But it needs high caution while using this device. Besides, it is recommended that the center of transportation and vehicle engineering (ASTU) members need to work strongly on the DSP-based onboard battery charging system to realize the electric vehicle charging system. In Adama Science and Technology University students are not getting DSP workshops. Therefore, it is recommended to have it and teach students as DSP is modern and smart technology. It is also recommended to apply the active balancing of the battery cell because it is most efficient. But its controlling algorithm will be more complex and costly.

Acknowledgments: This research thesis was funded by Adama Science and Technology University under the grant number of **ASTU/SM-R/079/19**, Adama, Ethiopia.

References

[1] Ethiopian Panel on Climate Change, " Ethiopian Panel on Climate Change: First Assessment Report, Summary of Reports for Policy Makers," Ethiopian Academy of Sciences, Addis Ababa, Ethiopia, 2015.

[2] B. Dagnew, "Introduction to transportation system," Department of Transport Management, Ethiopian Civil Service University, Addis Ababa, Ethiopia, 2012.

[3] FDRE Transport Authority, "Annual report of fleet," Addis Ababa, Ethiopia, 2018, Available at http://www.transportauthority.gov.et/.

[4] "X. Chen, W. Shen, T. T. Vo, Z. Cao and A. Kapoor, "An overview of lithium-ion batteries for electric vehicles," 2012 10th International Power & Energy Conference (IPEC), Ho Chi Minh City, 2012, pp. 230-235, doi: 10.1109/ASSCC.2012.6523269.".

[5] "S. Barcellona, D. D. Simone and S. Grillo, "Real-time Electric Vehicle Range Estimation Based on a Lithium-Ion Battery Model," 2019 International Conference on Clean Electrical Power (ICCEP), Otranto, Italy, 2019, pp. 351-357, doi: 10.1109/ICCEP.2019.8890".

[6] A. Shahin, R. Gavagsaz-Ghoachani, J. Martin, S. Pierfederici, B. Davat and F. Meibody-Tabar, "New Method to Filter HF Current Ripples Generated by Current-Fed DC/DC Converters," in IEEE Transactions on Power Electronics, vol. 26, no. 12, pp. 3832-3842,, Dec. 2011, doi: 10.1109/TPEL.2011.2134870..

[7] "M. A. Devi, K. Valarmathi and R. Mahendran, "Ripple current reduction in interleaved boost converter by using advanced PWM techniques," 2014 IEEE International Conference on Advanced Communications, Control and Computing Technologies, Ramanathapuram, 2014," pp. 115-119, doi: 10.1109/ICACCCT.2014.7019291..

[8] Zhang, Cheng & Li, Kang & Mcloone, Sean & Yang, Zhile. (2014). "Battery modelling methods for electric vehicles - A review." 2014 European Control Conference, ECC 2014. pp.2673-2678. .

[9] Shen, Weixiang & Vo, Thanh & Kapoor, Ajay, "Charging algorithms of lithium-ion batteries: An overview.," in *Proceedings of the 2012 7th IEEE Conference on Industrial Electronics and Applications (ICIEA)*, 2012.

[10] IPCC (Intergovernmental Panel on Climate Change), "Climate Change Impacts, Adaptation and Vulnerability. Working Group II, contributing to the fourth assessment report of the IPCC," Retrieved from http://www.ipcc.ch/pdf/ assessmentreport/ ar4/ wg2/ ar4_wg2_full_report.pdf. (24th march, 2020)..

[11] UNFCCC (United Nations Framework Convention on Climate Change) (2011), " "CO2 emissions of road transport," Retrieved from http://unfccc.int/. (27th march , 2020). .

[12] USAID,GHG Factsheet (2015), "Greenhouse Gas Emissions in Ethiopia. Greenhouse Gas Emissions Factsheet," Retrieved from https://www.climatelinks.org/sites / default / files/ asset/ documentGHG% 20Emissions%20Factsheet%20Ethiopia_final%20for%20PDF%20v3_11-02-15.

[13] CRGE, Federal Democratic Republic of Ethiopia, "Ethiopia's Climate Resilient Green Economy Strategy. The Path to Sustainable Development," Addis Ababa, Ethiopia, 2011.

[14] IEEE Standard for Interconnection and Interoperability of Distributed Energy Resources with Associated Electric Power Systems Interfaces,, IEEE Standard 1547, 2018..

[15] M. Kesler, M. Kisacikoglu, and L. Tolbert, "Vehicle-to-Grid Reactive Power Operation Using Plug-in Electric Vehicle Bidirectional Off-Board Charger," *IEEE Transactions on Industrial*, vol. 2, pp. 1-1, 2014.

[16] J. C. Mukherjee and A. Gupta,, "A Review of Charge Scheduling of Electric Vehicles in Smart Grid," *IEEE Systems Journal*, vol. 9, pp. 1541-1553, 2015.

[17] M. Yilmaz and P. T. Krein, "Review of Battery Charger Topologies, Charging Power Levels, and Infrastructure for Plug-In Electric and Hybrid Vehicles," *IEEE Transactions on Power Electronics*, vol. 28, pp. 2151-2169, 2013.

[18] M.A. Hannan, M.M. Hoque, A. Mohamed and A. Ayob, "Review of energy storage systems for electric vehicle applications: issues and challenges," *Renewable & Sustainable Energy Reviews*, vol. 69, pp. 771-789, 2017.

[19] B. Balagopal, C.S. Huang, M. Chow, "Effect of Calendar Aging on Li Ion Battery Degradation and SOH," *43rd Annual Conf. of the IEEE Ind. Ele. Society (IECON)* , pp. 7647-7652, 2017.

[20] Z. B. Omariba, L. Zhang, and D. Sun, "Review on health management system for lithium-ion batteries of electric vehicles," *Electronics,* Vols. 7, no. 5, p. 72, 2018.

[21] K. Liu, K. Li, Q. Peng, and C. Zhang, "A brief review on key technologies in the battery management system of electric vehicles," *Front. Mech. Eng.,* Vols. 14, no. 1, p. 47–64, 2019.

[22] S. Jurkovic, K. M. Rahman, and P. J. Savagian, "Design, optimization and development of electric machine for traction application in GM battery electric vehicle," *IEEE International Electric Machines & Drives Conference (IEMDC),* pp. 1814-1819, 2015.

[23] P. Leijen and N. Kularatna, "Developing a monitoring system for Toyota Prius battery-packs for longer term performance issues," *IEEE International Symposium on Industrial Electronics,,* pp. 1-6, 2013.

[24] K. J. Kelly, M. Mihalic, and M. Zolot, "Battery usage and thermal performance of the Toyota Prius and Honda Insight during chassis dynamometer testing," *Seventeenth Annual Battery Conference on Applications and Advances. Proceedings of Conference (Cat. No.02TH8576*, pp. 247-252, 2002.

[25] G. Renn, G. Ma and N. Cong, "Review of electrical energy storage system for vehicular applications," *Renewable & Sustainable Energy Reviews,* vol. 41, p. 225–236, 2015.

[26] J. R. M. D. Reyes, R. V. Parsons, and R. Hoemsen, "Winter Happens: The Effect of Ambient Temperature on the Travel Range of Electric Vehicles," *IEEE Transactions on Vehicular Technology,* vol. 65, pp. 4016-4022, 2016.

[27] "Is Li-Ion the Solution for the Electric Vehicle?," Available online: https://batteryuniversity.com/learn/archive/is_li_ion_the_solution_for_the_electric_vehicle (accessed on 12 july 2010)..

[28] S. R. Osman, N. A. Rahim, and S. Jeyraj, "Single current sensor with multiple constant current charging method in solar battery charger," *3rd IET International Conference on Clean Energy and Technology (CEAT)* , pp. 1-5, 2014.

[29] Y. D. Lee and S. Y. Park, "Rapid charging strategy in the constant voltage mode for a high power Li-Ion battery," *IEEE Energy Conversion Congress and Exposition,* pp. 4725-4731, 2013.

[30] S. G. Abeyratne, P. S. N. Perera, H. S. Jayakody, S. M. K. B. Samarakoon, and R. R. S. De Bulathge , "Soft Switching fast charger for batteries used in Renewable Energy applications and electric vehicles," *in Industrial and Information Systems (ICIIS), 2012 7th IEEE International Conference,* pp. 1-6., 2012.

[31] L. Yi-Hwa, T. Jen-Hao, and L. Yu-Chung, "Search for an optimal rapid charging pattern for lithium-ion batteries using ant colony system algorithm," *IEEE Transactions on Industrial Electronics,* vol. 52, pp. 1328-1336, 2005.

[32] SAE Standard J1772, SAE Electric Vehicle and Plug-in Hybrid Electric Vehicle Conductive Charge Coupler, 2010.

[33] International Energy Agency, “Global EV Outlook 2018,”IEA Publications, May 2018, [Online]. Available: https://webstore.iea.org/download/direct/1045?filename=global_ev_outlook_2018.pdf.

[34] U.S. Department of Energy Office of Energy Efficiency and Renewable Energy, "Fiscal Year 2018 Advanced Vehicle Technologies Research Funding Opportunity Announcement: DE-FOA-0001919," pp. 6, May 2018. [Online]. Available: https://eereexchange.energy.gov/FileContent.aspx?FileID=a0948ac6-6da7-4a45-a613-d83688193f1c..

[35] T. Kang, C. Kim, Y. Suh, H. Park, B. Kang, and D. Kim, "A design and control of bi-directional non-isolated DC-DC converter for rapid electric vehicle charging system," *IEEE International Conference on Information and Automation,* pp. 14-21, 2012 .

[36] J. G. Pinto, V. Monteiro, H. Gonçalves, and J. L. Afonso, "Onboard Reconfigurable Battery Charger for Electric Vehicles With Traction-to-Auxiliary Mode," *IEEE Transactions on Vehicular Technology,* vol. 63, pp. 1104-1116, 2014.

[37] B. Yang, "Topology Investigation for Front End DC/DC Power Conversion for Distributed Power System," Virginia Polytechnic Institute and State University, 2003.

[38] D. Erickson, R.W. and Maksimovic, Fundamentals of Power Electronics, Springer, 2001.

[39] S. Rogers, "Electric Drive Status and Challenges," us depatment of energy , 2012.

[40] J. P. M. Figueiredo, F. L. Tofoli, and B. L. A. Silva, "A Review of SinglePhase PFC Topologies Based on the Boost Converter," *9th IEEE/IAS International Conference on Industry Applications - INDUSCON,* p. 1–6, 2010.

[41] T. H. Kim, J.-B. Jeong, B.-H. Lee, D.-H. Shin, H.-S. Song, B.-H. Kim, and H.-J. Kim, "Analytical study on low-frequency ripple effect of battery charging," *IEEE Vehicle Power and Propulsion Conference,* p. 809–811, 2012.

[42] P. Kong, S. Wang, and F. C. Lee, "Common Mode EMI Noise Suppression for Bridgeless PFC Converters," *IEEE Trans. Power Electronics* , Vols. 23, no. 1, p. 291–297, 2008.

[43] a V, Jaya & Williamson, Sheldon, "A Review of Front End AC-DC Topologies in Universal Battery Charger for Electric Transportation," *IEEE Transportation Electrification Conference and Expo (ITEC),* pp. 293-298, 2018.

[44] Shenoy, Latha & Nayak, C. & Mandi, Rajashekar, "Design and Implementation of Interleaved Boost Converter," *International Journal of Engineering and Technology,* vol. 9, pp. 496-502, 2017.

[45] F. Musavi, W. Eberle, and W. G. Dunford, "A High-Performance Single-Phase Bridgeless Interleaved PFC Converter for Plug-in Hybrid Electric Vehicle Battery Chargers," *IEEE Transactions on Industry Applications,* Vols. 47, no. 4, p. 1833–1843, 2011.

[46] Zein Eddine, Abbass & Zaarour, Iyad & Guerin, Francois & Hijazi, Abbas, "Improving Fault Isolation in DC/DC Converters Based with Bayesian Belief Networks," *IFAC (International Federation of Automatic Control) Elsevier,* vol. 49 no. 5, p. 303–308, 2016.

[47] "Phase-Shifted Full Bridge DC/DC Power Converter Design guide," Texas Instruments Incorporated, 2014.

[48] Gu, Bin & Lin, Chien-Yu & Chen, BaiFeng & Dominic, Jason & Lai, Jih-Sheng, "Zero-Voltage-Switching PWM Resonant Full-Bridge Converter With Minimized Circulating Losses and Minimal Voltage Stresses of Bridge Rectifiers for Electric

Vehicle Battery Chargers," *IEEE Transaction on Power Electronics* , Vols. 28, no.10, p. 4657–4667, 2013.

[49] Lin, Chang-Hua & Wang, Ming-Chien & Hung, Min-Hsuan & Li, Ming-Hsuan, "Series-resonant battery charger with synchronous rectifiers for LiFePO4 battery pack," *Proceedings of the 2011 6th IEEE Conference on Industrial Electronics and Applications,* pp. 316-321, 2011.

[50] Mohamed Salem, Awang Jusoh, N. Rumzi N. Idris, Tole Sutikno & Iftikhar Abid, "ZVS Full Bridge Series Resonant Boost Converter with Series-Connected Transformer," *International Journal of Power Electronics and Drive System (IJPEDS),* Vols. 8, No. 2, pp. 812-825 , June 2017.

[51] "A Cost-Effective Design and Analysis of Full Bridge LLC Resonant Converter," *International Journal of Energy and Power Engineering,* Vols. 10, No. 8 , pp. 1143-1150, 2016.

[52] Shen, Y., Zhao, W., Chen, Z., & Cai, C. , "Full-Bridge LLC Resonant Converter With Series-Parallel Connected Transformers for Electric Vehicle On-Board Charger," *IEEE Access,* vol. 6, pp. 13490-13500, 2018.

[53] Z. B. Omariba, L. Zhang, and D. Sun, "Review on health management system for lithium-ion batteries of electric vehicles," *Electronics,* Vols. 7, no. 5, p. 72, 2018.

[54] Fujita, Y. Hirose, Y. Kato, & Y. Watanabe T. , "Development of battery management system," *FUJITSU TEN Tech. J.,* vol. 42, p. 68–80, 2016.

[55] Verasamy, M. & Faisal, Mohammad & Ker, Pin Jern & Hannan, M. A., "Charging and Discharging Control of Li-Ion Battery Energy Management for Electric Vehicle Application," *International Journal of Engineering and Technology(UAE),* vol. 7, pp. 482-486, 2018.

[56] Urbain, M.; Raël, S.; Davat, B.; Desprez, P., "State Estimation of a Lithium-Ion Battery through Kalman Filter. In Proceedings of IEEE Power Electronics Specialists Conference, Orlando, FL, USA,," in *In Proceedings of IEEE Power Electronics Specialists Conference,* Orlando, FL, USA, 17–21 June 2007..

[57] Yuan, S., Wu, H. & Yin, C. , " State of charge estimation using the extended Kalman filter for battery management systems based on the ARX battery model," *Energies,* vol. 6, p. 444–470, 2013.

[58] Lee, Y.-S.; Wang, W.-Y.; Kuo, T.-Y., "Soft computing for battery state-of-charge (BSOC) estimation in battery string systems.," *IEEE Transaction of Industrial Electronics*, vol. 1, p. 229–239, 2008.

[59] Li, S.G., Sharkh, S.M., Walsh, F.C. &Zhang, C.N., " Energy and battery management of a plug-in series hybrid electric vehicle using fuzzy logic," *IEEE Transaction of Vehicle Technology,* vol. 8, p. 3571–3585, 2011.

[60] Fang Liu, Jie Ma, Weixing Su, "Unscented Particle Filter for SOC Estimation Algorithm Based on a Dynamic Parameter Identification", Mathematical Problems in Engineering, vol. 2019, Article ID 7452079, 14 pages, 2019. https://doi.org/10.1155/2019/7452079.

[61] Omariba, Zachary & Zhang, Lijun & Sun, Dongbai, "Review of Battery Cell Balancing Methodologies for Optimizing Battery Pack Performance in Electric Vehicles," *IEEE Access,* vol. 10, pp. 1-1, 2019.

[62] Y. Chen, X. Liu, H. K. Fathy, J. Zou, & S. Yang,, " A graph-theoretic framework for analyzing the speeds and efficiencies of battery pack equalization circuits," *International Journal of Electrical Power & Energy Systems,* vol. 98, pp. 85-99, 2018.

[63] T. Bruen, J. Marco, and M. Gama, "Battery energy storage system modeling: A combined comprehensive approach," *ELSEVIER Journal of Energy Storage,* vol. 21, pp. 172-185, February 2019.

[64] Anderson, R., Zane, R., Plett, G., Maksimovic, D. et al., "Life Balancing – A Better Way to Balance Large Batteries," *SAE Technical Paper,* vol. 1, p. 4–6, Apr. 2017.

[65] "Energy," October 2017. [Online]. Available: https://www.energy.gov/sites/prod/files/2017/11/f39/EETT%20Roadmap%2010-27-17.pdf. [Accessed 24 August 2020].

[66] H. Wang and F. Blaabjerg, "Reliability of Capacitors for DC-Link Applications in Power Electronic Converters—An Overview," *in IEEE Transactions on Industry Applications,* Vols. 50, no. 5, pp. 3569-3578, 2014.

[67] Yang, Gang & Lindseth, Roar & liu, hui & Sorsdahl, Torbjorn & Draugedalen, Eirik, "Design of High Efficiency High Power Density 10.5kW Three Phase On-Board-Charger for Electric/Hybrid Vehicles.," in *International Exhibition and*

Conference for Power Electronics, Intelligent Motion, Renewable Energy and Energy Management, Nuremberg, Germany,, 2016.

[68] Lu, Juncheng & Taylor, Allan & Bai, Hua & Liu, Guanliang & Brown, Alan & Johnson, Mike & McAmmond, Matt., "A Modular-Designed Three-Phase High-Efficiency High-Power-Density EV Battery Charger Using Dual/Triple-Phase-Shift Control," *IEEE Transactions on Power Electronics,* pp. 1-1, 2017.

[69] Weise, Nathan & Castelino, Gysler & Basu, Kaushik & Mohan, Niall., "A Single-Stage Dual-Active-Bridge-Based Soft Switched AC–DC Converter With Open-Loop Power Factor Correction and Other Advanced Features," *IEEE Transactions on Power Electronics,* Vols. 29, no. 8 , pp. 4007-4016, 2014.

[70] G. L. e. al., "Comparison of SiC MOSFETs and GaN HEMTs based high-efficiency high-power-density 7.2kW EV battery chargers," *IEEE 5th Workshop on Wide Bandgap Power Devices and Applications (WiPDA), Albuquerque, NM,,* pp. 391-397, 2017.

[71] X. Wang, C. Jiang, B. Lei, H. Teng, H. K. Bai & J. L. Kirtley, "power Loss Analysis and Efficiency Maximization of a Silicon-Carbide MOSFET-Based Three-Phase 10-kW Bidirectional EV Charger Using Variable-DC-Bus Control," *IEEE Journal of Emerging and Selected Topics in Power Electronics,* Vols. 4, no. 3, pp. 880-892 , Sept. 2016.

[72] A. Mallik and A. Khaligh, "Control of a Three-Phase Boost PFC Converter Using a Single DC Link Voltage Sensor," *IEEE Transactions on Power Electronics*, Vols. 32, no. 8 , pp. 6481-6492, Aug. 2017.

[73] A. Mallik, W. Ding, C. Shi and A. Khaligh, "Input Voltage Sensorless Duty Compensation Control for a Three-Phase Boost PFC Converter," *IEEE Transactions on Industry Applications*, Vols. 53, no. 2, pp. 1527-1537, Mar. 2017.

[74] P. M. Johnson and K. H. Bai, "A dual-DSP controlled SiC MOSFET based 96%-efficiency 20kW EV on-board battery charger using LLC resonance technology," in *2017 IEEE Symposium Series on Computational Intelligence (SSCI)*, Honolulu, HI , 2017.

[75] A. Mallik, W. Ding and A. Khaligh, "A Comprehensive Design Approach to an EMI Filter for a 6-kW Three-Phase Boost Power Factor Correction Rectifier in

Avionics Vehicular Systems," *IEEE Transactions on Vehicular Technology,* Vols. 66, no. 4, pp. 2942-2951, 2017.

[76] Singh, Akshay & Mallik, Ayan & Khaligh, Alireza, "A Comprehensive Design and Optimization of the DM EMI Filter in a Boost PFC Converter," *IEEE Transactions on Industry Applications,* pp. 1-1, 2018.

[77] Haijun Tao, Guopeng Zhang and Zheng Zheng, , "Onboard Charging DC/DC Converter of Electric Vehicle Based on Synchronous Rectification and Characteristic Analysis," *Hindawi Journal of Advanced Transportation* , p. 10, 2019.

[78] C.-M. Lai, C.-T. Pan, and M.-C. Cheng, "High-Efficiency Modular High StepUp Interleaved Boost Converter for DC-Microgrid Applications," *IEEE Transaction on industrial application* , Vols. 48, no. 1, p. 161–171, Jan. 2012.

[79] T. Nussbaumer, K. Raggl, & J. W. Kolar, "Design Guidelines for Interleaved Single-Phase Boost PFC Circuits," *IEEE Transaction on Industrial Electronics,* Vols. 56, no. 7, p. 2559–2573, Jul. 2009..

[80] M. R. Mohammadi and H. Farzanehfard, "New Family of Zero-VoltageTransition PWM Bidirectional Converters With Coupled Inductors," *IEEE Transaction Industrial Electronics,* Vols. 59, no. 2, p. 912–919, Feb. 2012.

[81] G. Pellegrino, E. Armando, and P. Guglielmi, "An Integral Battery Charger With Power Factor Correction for Electric Scooter," *IEEE Transaction Power Electronics,* Vols. 25, no. 3, pp. 751–759, , Mar. 2010..

[82] S. Haghbin, S. Lundmark, M. Alakula, and O. Carlson, "Grid-Connected Integrated Battery Chargers in Vehicle Applications: Review and New Solution," *IEEE Transaction Industrial Electronics,* Vols. 60, no. 2, p. 459–473, Feb. 2013..

[83] Chandra Mouli, Gautham Ram & Schijffelen, Jos & Bauer, Pavol & Zeman, Miro., "Design and Comparison of a 10kW Interleaved Boost Converter for PV Application Using Si and SiC Devices," *IEEE Journal of Emerging and Selected Topics in Power Electronics,* pp. 1-1, 2016.

[84] C. Wang, "Investigation on Interleaved Boost Converters and Applications," Virginia Polytechnic Institute and State University, 2009.

[85] X. Liu, W. Li and A. Zhou, "PNGV Equivalent Circuit Model and SOC Estimation Algorithm for Lithium Battery Pack Adopted in AGV Vehicle," *IEEE Access,* vol. 6, pp. 23639-23647, 2018.

[86] "Battery Test Manual For Plug-In Hybrid Electric Vehicles," U.S. Department of Energy Vehicle Technologies Program, available on https://inldigitallibrary.inl.gov/sites/sti/sti/6308373.pdf.

[87] S. Zhang, H. Sun and C. Lyu, "A method of SOC estimation for power Li-ion batteries based on equivalent circuit model and extended Kalman filter Wuhan," in *2018 13th IEEE Conference on Industrial Electronics and Applications (ICIEA),* Wuhan, 2018.

[88] Huria, Tarun & Jackey, Robyn & Gazzarri, Javier & Saginaw, Michael & Sanghvi, Pravesh, "Battery Model Parameter Estimation Using a Layered Technique: An Example Using a Lithium Iron Phosphate Cell.," *SAE Technical Papers. 2. 10.4271/2013-01-1547.*.

[89] B. X. ,. B. L. ,. L. C. ,. Y. L. ,. W. Z. ,. W. a. W. W. Ruifeng Zhang, "State of the Art of Lithium-Ion Battery SOC Estimation for Electrical Vehicles," *Energies 2018,* vol. 11, doi:10.3390/en11071820, 2018.

Reference Links

[L1] Available on https://www.capitalethiopia.com/featured/petrol-companies-default-on-millions/

[L2] BRUSA, "NLG667 – On Board Fast Charger," BRUSA, 2018. [Online] Available https://www.brusa.biz/fileadmin/template/Support-Center/Datenbl%C3%A4tter/BRUSA_DB_EN_NLG667.pdf

[L3] G-Power, "10kW air-cooled on-board charger," G-Power, 2015. [Online] Available http://www.gevpower.com/product_detail_en3/id/5.html

[L4] Continental, "On-Board Charger," Continental, 2017. [Online]. Available https://vitesco-technologies.com/en/Home/Solutions/Electrification

Appendixes

Appendix A: Appendixes Related to Modeling of the Battery Management System.

A.1. MATLAB Code for The Battery Modeling

```
%% Load data for Sanyo UR18650W battery
clear
load('sanyo.mat');
%%
SOC_LUT = (0:.1:1)';
Capacity = 1.5;
%% Resistance and OCV calculation
% Prepare normalized x axes for each current
% x1p5 = sanyo_1p5A_25C(:,1)/sanyo_1p5A_25C(end,1);
% x10  = sanyo_10A_25C(:,1)/ sanyo_10A_25C(end,1);
% x15  = sanyo_15A_25C(:,1)/ sanyo_15A_25C(end,1);
% x20  = sanyo_20A_25C(:,1)/ sanyo_20A_25C(end,1);
x1p5 = sanyo_1p5A_25C(:,1)/sanyo_1p5A_25C(end,1);
x10  = sanyo_10A_25C(:,1)/ sanyo_1p5A_25C(end,1);
x15  = sanyo_15A_25C(:,1)/ sanyo_1p5A_25C(end,1);
x20  = sanyo_20A_25C(:,1)/ sanyo_1p5A_25C(end,1);
%% Plot discharge curves at each current
Figure(1)
plot(    x1p5, sanyo_1p5A_25C(:,2),...
         x10,  sanyo_10A_25C(:,2),...
         x15,  sanyo_15A_25C(:,2),...
         x20,  sanyo_20A_25C(:,2))
legend({'1.5A' '10A' '15A' '20A'})
xlabel('1-SOC')
xlim([0 1])
ylabel('V')
title('Sanyo UR18650W 25ºC')
%% Fitting discharge curves at different currents
fit1p5 = fit(x1p5,sanyo_1p5A_25C(:,2),'smoothingspline');
fit10  = fit(x10, sanyo_10A_25C(:,2), 'smoothingspline');
fit15  = fit(x15, sanyo_15A_25C(:,2), 'smoothingspline');
fit20  = fit(x20, sanyo_20A_25C(:,2), 'smoothingspline');
Figure(2)
hold on
plot(fit1p5,'-k'); plot(fit10,'-r'); plot(fit15,'-b'); plot(fit20,'-g');
legend({'1.5A' '10A' '15A' '20A'})
xlabel('1-SOC')
ylabel('V')
title('Sanyo UR18650W 25ºC Spline Fit')
%% Construct V vs. discharge current for different SOC levels
% Em_MAT is a matrix with rows: SOC, cols: current
for i=1:length(SOC_LUT)
    Em_MAT(i,:) = [fit1p5(SOC_LUT(i)) fit10(SOC_LUT(i)) fit15(SOC_LUT(i))
fit20(SOC_LUT(i))];
end
% Fit and visualize Em vs. I for each SOC level
colorV = {'-k','-r','-b','-g','-c','-k','-r','-b','-g','-c','-k'};
colorF =
{'black','black','black','black','black','red','red','red','red','red','blue'};
Figure(3)
```

```
hold on
for i=1:length(SOC_LUT)
    plot([1.5 10 15
20],Em_MAT(i,:),colorV{i},'Marker','o','MarkerFaceColor',colorF{i})
end
xlabel('i Amps')
ylabel('V Volts')
legend(num2str(SOC_LUT),'Location','eastoutside')
title('Sanyo UR18650W 25ºC - legend: 1-SOC')
%% Fit a line to the V vs. i curve to extrapolate to i=0
fitSOC00 = fit([1.5 10 15 20]',Em_MAT(1,:)','poly1');
fitSOC01 = fit([1.5 10 15 20]',Em_MAT(2,:)','poly1');
fitSOC02 = fit([1.5 10 15 20]',Em_MAT(3,:)','poly1');
fitSOC03 = fit([1.5 10 15 20]',Em_MAT(4,:)','poly1');
fitSOC04 = fit([1.5 10 15 20]',Em_MAT(5,:)','poly1');
fitSOC05 = fit([1.5 10 15 20]',Em_MAT(6,:)','poly1');
fitSOC06 = fit([1.5 10 15 20]',Em_MAT(7,:)','poly1');
fitSOC07 = fit([1.5 10 15 20]',Em_MAT(8,:)','poly1');
fitSOC08 = fit([1.5 10 15 20]',Em_MAT(9,:)','poly1');
fitSOC09 = fit([1.5 10 15 20]',Em_MAT(10,:)','poly1');
fitSOC10 = fit([1.5 10 15 20]',Em_MAT(11,:)','poly1');
R0_25 = abs(mean([fitSOC02.p1 fitSOC04.p1 fitSOC06.p1 fitSOC08.p1 ]));
%% Extrapolate the values of Voltage to i=0 to estimate the OCV at different SOC
levels
Em = [fitSOC00(0) fitSOC01(0) fitSOC02(0) fitSOC03(0)...
      fitSOC04(0) fitSOC05(0) fitSOC06(0) fitSOC07(0)...
      fitSOC08(0) fitSOC09(0) fitSOC10(0) ]';
Figure(1)
hold on
plot(SOC_LUT,Em,'o','MarkerFaceColor','k')
Em_fit = fit(SOC_LUT,Em,'smoothingspline');
Em = Em_fit((0:.01:1)');
% Em (OCV) at 25ºC as a result of extrapolation of discharge curves to 0A
% Em = flipud(Em);
%% Calculate time, current and voltage vectors for simulation
t1p5 =(0:Capacity * 3600 / 1.5)';
t10 = (0:Capacity * 3600 / 10)';
t15 = (0:Capacity * 3600 / 15)';
t20 = (0:Capacity * 3600 / 20)';
i1p5 = 1.5 * ones(length(t1p5),1);
i10 = 10 *   ones(length(t10),1);
i15 = 15 *   ones(length(t15),1);
i20 = 20 *   ones(length(t20),1);
fitV1p5 = fit1p5((0:1/(length(t1p5)-1):1)');
fitV10  = fit10((0:1/ (length(t10)-1 ):1)');
fitV15  = fit15((0:1/ (length(t15)-1 ):1)');
fitV20  = fit20((0:1/ (length(t20)-1 ):1)');
%% Plot discharge at different T's @ i = 10A
xm10C = sanyo_10A_m10C(:,1)/ sanyo_10A_25C(end,1);
x0C   = sanyo_10A_0C(:,1)  / sanyo_10A_25C(end,1);
x60C  = sanyo_10A_60C(:,1) / sanyo_10A_25C(end,1);
Figure(4)
plot(   xm10C, sanyo_10A_m10C(:,2),...
        x0C  , sanyo_10A_0C(:,2),...
        x10  , sanyo_10A_25C(:,2),...
        x60C , sanyo_10A_60C(:,2))
legend({'-10ºC' '0ºC' '25ºC' '60ºC'})
xlabel('1-SOC')
ylabel('V')
xlim([0 1])
%% Time, current, and voltage vectors for simulation
% Capacity should be corrected by temperature
```

```matlab
% Construct fit objects for Voltage vs. SOC
fitm10C = fit(xm10C, sanyo_10A_m10C(:,2), 'smoothingspline');
fit0C   = fit(x0C  , sanyo_10A_0C  (:,2), 'smoothingspline');
fit60C  = fit(x60C , sanyo_10A_60C (:,2), 'smoothingspline');
% If i=constant, we can translate Ah to sec as:
tm10C = (0:sanyo_10A_m10C(end,1) * 3600 / 10)';
t0C   = (0:sanyo_10A_0C(end,1)   * 3600 / 10)';
t60C  = (0:sanyo_10A_60C(end,1)  * 3600 / 10)';
% Evaluate V at each time stamp
fitVm10C = fitm10C((0:1/ (length(tm10C)-1 ):xm10C(end))');%1)');%
fitV0C   = fit0C  ((0:1/ (length(t0C)   -1 ):x0C(end))');%1)');%
fitV60C  = fit60C ((0:1/ (length(t60C) -1 ):x60C(end))');%1)');%
% Calculate duration of each discharge
tm10C = tm10C(1:length(fitVm10C));
t0C = t0C(1:length(fitV0C));
t60C = t60C(1:length(fitV60C));
% Current is a constant in all cases
im10C = 10 * ones(length(tm10C),1);
i0C   = 10 * ones(length(t0C),1);
i60C  = 10 * ones(length(t60C),1);
%% Load LUT calculated using parameter estimation at different temperatures
% load('sanyo_LUT.mat')
% Instead of importing from PE SL procedure, we estimate the resistance at
% different temperatures by doing R = DeltaV/DeltaI
% We first create V = f(SoC) curves
Vm10C = fitm10C(0:.01:1);
V0C   = fit0C  (0:.01:1);
V60C  = fit60C (0:.01:1);
V25C = fit10 (0:.01:1);
% Then we calculate resistance using I = 10A
Rm10C = (Em - Vm10C)./10;
R0C = (Em - V0C)./10;
R25C = (Em - V25C)./10;
R60C = (Em - V60C)./10;
% Since later we will fit R0 as a function of SOC, we need to flip it
% upside down because up until now it was a function of x = 1-SOC
R0_LUT = flipud([Rm10C R0C R25C R60C]);
T_LUT = 273 + [-10 0 25 60];
%% Plot R0 vs. T
Figure(5)
hold on
SOCbkpts = [20 40 60 80];
color = {'k' 'b' 'r' 'g'};
for k=1:4
    scatter(1000./T_LUT , log(R0_LUT(SOCbkpts(k),:)),'MarkerFaceColor',color{k})
end
%%
disp('Temperature dependence of R_0')
for k=1:4
    R0_vs_T_fit = fit(1000./T_LUT' , log(R0_LUT(SOCbkpts(k),:))','poly1');
    plot(R0_vs_T_fit)
    Ea(k) = 8.314 * R0_vs_T_fit.p1;
end
xlabel('1000/T (1000/K)')
ylabel('ln(R_0) (\Omega)')
title('Arrhenius plot of R_0 vs. 1000/T')
disp(' ')
disp('Activation energy for Li ion conduction')
disp(['Ea = ' num2str(Ea) ' kJ/mol'])
% legend({['Ea = ' num2str(Ea) ' kJ/mol']})
legend({'SOC = 20%','SOC = 40%','SOC = 60%','SOC = 80%'})
disp('Compare with Ji et al, JES 160(4) A636-A649 pA640')
```

```
disp('Ea for electrolyte transport in Li ion battery = 20 kJ/mol')
%% Fit a surface of R = f(T,SOC)
R0_LUT_bkpts = [Rm10C(SOCbkpts) R0C(SOCbkpts) R25C(SOCbkpts) R60C(SOCbkpts)];
[R0_vs_T_SOC_fit, gof] =
fit([repmat(SOCbkpts'/100,4,1),reshape(repmat(1000./T_LUT,4,1),16,1)]...
    ,reshape(log(R0_LUT_bkpts),16,1),'poly21');
Figure(6)
plot(R0_vs_T_SOC_fit,[repmat(SOCbkpts'/100,4,1),reshape(repmat(1000./T_LUT,4,1),16
,1)]...
    ,reshape(log(R0_LUT_bkpts),16,1))
xlabel('SOC')
ylabel('1000/T (K)')
zlabel('ln(R)')
```

A.2. MATLAB Code for Charging Control of the Cell

```
%%
numCells = 3;
% load('Kokam_LUT_3RC')%
results.T5C  = load('batteryParameterEstimation_results_3RC_5degC.mat');
results.T20C = load('batteryParameterEstimation_results_3RC_20degC.mat');
results.T40C = load('batteryParameterEstimation_results_3RC_40degC.mat');
SOC_LUT = results.T5C.SOC_LUT;
%% Thermal Properties
% Cell dimensions and sizes
cell_thickness = 0.0084; %m
cell_width = 0.215; %m
cell_height = 0.220; %m
% Cell surface area
cell_area = 2 * (...
    cell_thickness * cell_width +...
    cell_thickness * cell_height +...
    cell_width * cell_height); %m^2
% Cell volume
cell_volume = cell_thickness * cell_width * cell_height; %m^3
%%
for idx = 1:numCells
%% Lookup Table Breakpoints
Battery(idx).SOC_LUT = SOC_LUT;
Battery(idx).Temperature_LUT = [5 20 40] + 273.15;
%% Em Branch Properties (OCV, Capacity)
% Battery capacity
Battery(idx).Capacity_LUT = [31 31 31]; %Ampere*hours
%% Em Branch Properties (OCV, Capacity)
% Em open-circuit voltage vs SOC rows and T columns
Battery(idx).Em_LUT = [ results.T5C.Em ...
                        results.T20C.Em ...
                        results.T40C.Em]; %Volts
%% Terminal Resistance Properties
% R0 resistance vs SOC rows and T columns
Battery(idx).R0_LUT = [ results.T5C.R0 ...
                        results.T20C.R0 ...
                        results.T40C.R0]; %Ohms
%% RC Branch 1 Property
% R1 Resistance vs SOC rows and T columns
Battery(idx).R1_LUT = [ results.T5C.R1 ...
                        results.T20C.R1 ...
                        results.T40C.R1]; %Ohms
% R2 Resistance vs SOC rows and T columns
Battery(idx).R2_LUT = [ results.T5C.R2 ...
                        results.T20C.R2 ...
```

```
                        results.T40C.R2]; %Ohms
% R3 Resistance vs SOC rows and T columns
Battery(idx).R3_LUT = [ results.T5C.R3 ...
                        results.T20C.R3 ...
                        results.T40C.R3]; %Ohms
% C1 Capacitance vs SOC rows and T columns
Battery(idx).t1_LUT = [ results.T5C.tau1 ...
                        results.T20C.tau1 ...
                        results.T40C.tau1]; %Farads
% C2 Capacitance vs SOC rows and T columns
Battery(idx).t2_LUT = [ results.T5C.tau2 ...
                        results.T20C.tau2 ...
                        results.T40C.tau2]; %Farads
% C3 Capacitance vs SOC rows and T columns
Battery(idx).t3_LUT = [ results.T5C.tau3 ...
                        results.T20C.tau3 ...
                        results.T40C.tau3]; %Farads
%%
% Cell mass
Battery(idx).cell_mass = 0.84; %kg
% Volumetric heat capacity
% assumes uniform heat capacity throughout the cell
% ref: J. Electrochemical Society 158 (8) A955-A969 (2011) pA962
Battery(idx).cell_rho_Cp = 2.04E6; %J/m3/K
% Specific Heat
Battery(idx).cell_Cp_heat = Battery(idx).cell_rho_Cp * cell_volume /
Battery(idx).cell_mass; %J/kg/K
%% Initial Conditions
% Charge deficit
% Battery(idx).Qe_init = 15.6845; %Ampere*hours
% Ambient Temperature
Battery(idx).T_init = 20 + 273.15; %K
end
%% Initial charge deficit
Battery(1).SOC0 = 0.2;
Battery(2).SOC0 = 0.22; %Ampere*hours
Battery(3).SOC0 = 0.24; %Ampere*hours
% Convective heat transfer coefficient
% For natural convection this number should be in the range of 5 to 25
h_conv = 5; %W/m^2/K Cell-to-cell
h_conv_end = 10; %W/m^2/K End cells to ambient
%% Passive balancing parameters
% load('tempParam')
I_cc = 15;
R = .2;
R_bleed = 20;
T_volt = 600;
V_th = 11.5;
deltaV = 0.01;
V_top = 12.5;
```

A.3. MATLAB Code for the State of Charge Estimation

```
%%
numCells = 1;
% load('Kokam_LUT_3RC')%
results.T5C  = load('batteryParameterEstimation_results_3RC_5degC.mat');
results.T20C = load('batteryParameterEstimation_results_3RC_20degC.mat');
results.T40C = load('batteryParameterEstimation_results_3RC_40degC.mat');
SOC_LUT = results.T5C.SOC_LUT;
%% Thermal Properties
```

```matlab
% Cell dimensions and sizes
cell_thickness = 0.0084; %m
cell_width = 0.215; %m
cell_height = 0.220; %m
% Cell surface area
cell_area = 2 * (...
    cell_thickness * cell_width +...
    cell_thickness * cell_height +...
    cell_width * cell_height); %m^2
% Cell volume
cell_volume = cell_thickness * cell_width * cell_height; %m^3
%%
for idx = 1:numCells
%% Lookup Table Breakpoints
Battery(idx).SOC_LUT = SOC_LUT;
Battery(idx).Temperature_LUT = [5 20 40] + 273.15;
%% Em Branch Properties (OCV, Capacity)
% Battery capacity
Battery(idx).Capacity_LUT = [31 31 31]; %Ampere*hours
%% Em Branch Properties (OCV, Capacity)
% Em open-circuit voltage vs SOC rows and T columns
Battery(idx).Em_LUT = [ results.T5C.Em ...
                        results.T20C.Em ...
                        results.T40C.Em]; %Volts
%% Terminal Resistance Properties
% R0 resistance vs SOC rows and T columns
Battery(idx).R0_LUT = [ results.T5C.R0 ...
                        results.T20C.R0 ...
                        results.T40C.R0]; %Ohms
%% RC Branch 1 Property
% R1 Resistance vs SOC rows and T columns
Battery(idx).R1_LUT = [ results.T5C.R1 ...
                        results.T20C.R1 ...
                        results.T40C.R1]; %Ohms
% R2 Resistance vs SOC rows and T columns
Battery(idx).R2_LUT = [ results.T5C.R2 ...
                        results.T20C.R2 ...
                        results.T40C.R2]; %Ohms
% R3 Resistance vs SOC rows and T columns
Battery(idx).R3_LUT = [ results.T5C.R3 ...
                        results.T20C.R3 ...
                        results.T40C.R3]; %Ohms
% C1 Capacitance vs SOC rows and T columns
Battery(idx).t1_LUT = [ results.T5C.tau1 ...
                        results.T20C.tau1 ...
                        results.T40C.tau1]; %Farads
% C2 Capacitance vs SOC rows and T columns
Battery(idx).t2_LUT = [ results.T5C.tau2 ...
                        results.T20C.tau2 ...
                        results.T40C.tau2]; %Farads
% C3 Capacitance vs SOC rows and T columns
Battery(idx).t3_LUT = [ results.T5C.tau3 ...
                        results.T20C.tau3 ...
                        results.T40C.tau3]; %Farads
%%
% Cell mass
Battery(idx).cell_mass = 0.84; %kg
% Volumetric heat capacity
% assumes uniform heat capacity throughout the cell
% ref: J. Electrochemical Society 158 (8) A955-A969 (2011) pA962
Battery(idx).cell_rho_Cp = 2.04E6; %J/m3/K
% Specific Heat
```

```
Battery(idx).cell_Cp_heat = Battery(idx).cell_rho_Cp * cell_volume /
Battery(idx).cell_mass; %J/kg/K
%% Initial Conditions
% Ambient Temperature
Battery(idx).T_init = 20 + 273.15; %K
% Initial charge deficit
Battery(idx).Qe_init = 0.5 * mean(Battery(idx).Capacity_LUT); %Ampere*hours
Battery(idx).SOC0 = (Battery(idx).Capacity_LUT(2) - Battery(idx).Qe_init)/...
                                  Battery(idx).Capacity_LUT(2);
end
%%
% Convective heat transfer coefficient
% For natural convection this number should be in the range of 5 to 25
h_conv = 5; %W/m^2/K Cell-to-cell
h_conv_end = 10; %W/m^2/K End cells to ambient
%%
load('BatteryParameters.mat')
```

Appendix B. Related to Onboard Charging MATLAB/Simulink Model

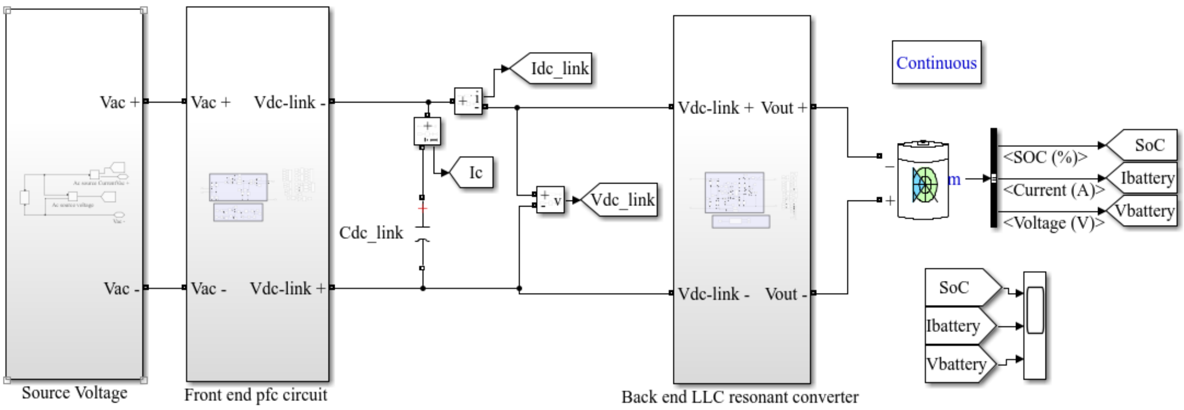

Figure B.1 overall charging system

B.1. Front end power factor correction circuit

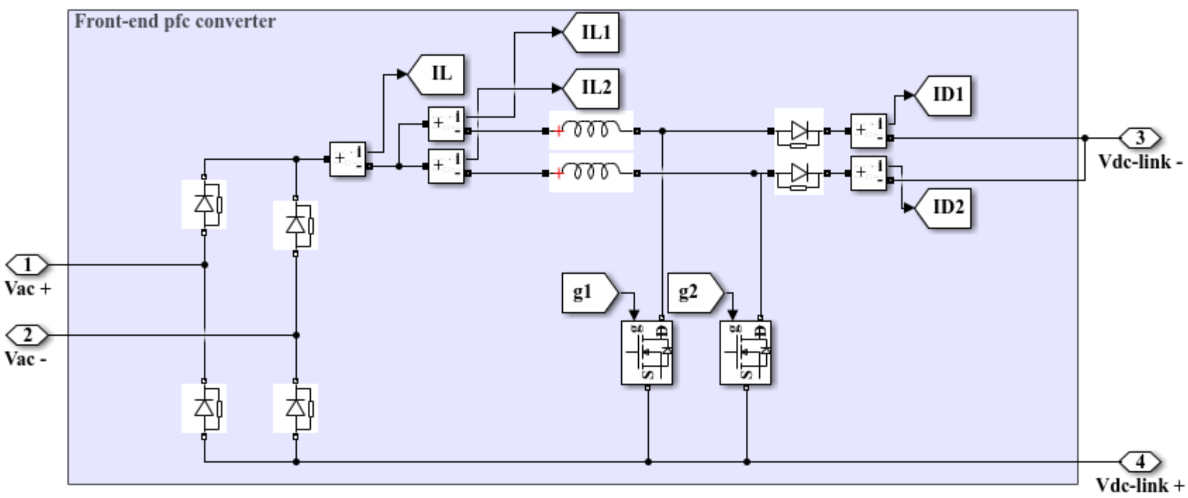

Figure B.2 interleaved boost PFC converter

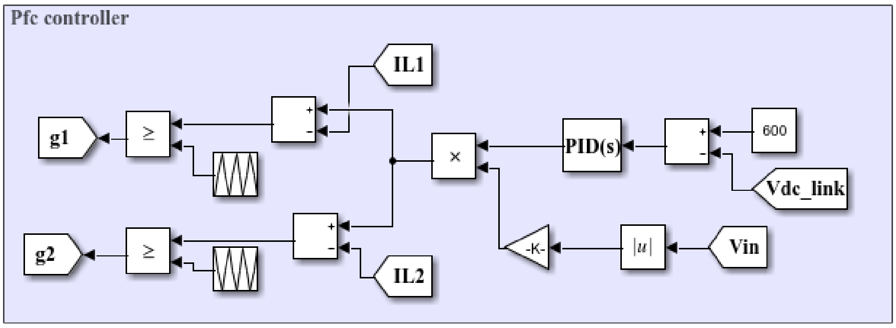

Figure B.3 control circuit of an interleaved boost converter

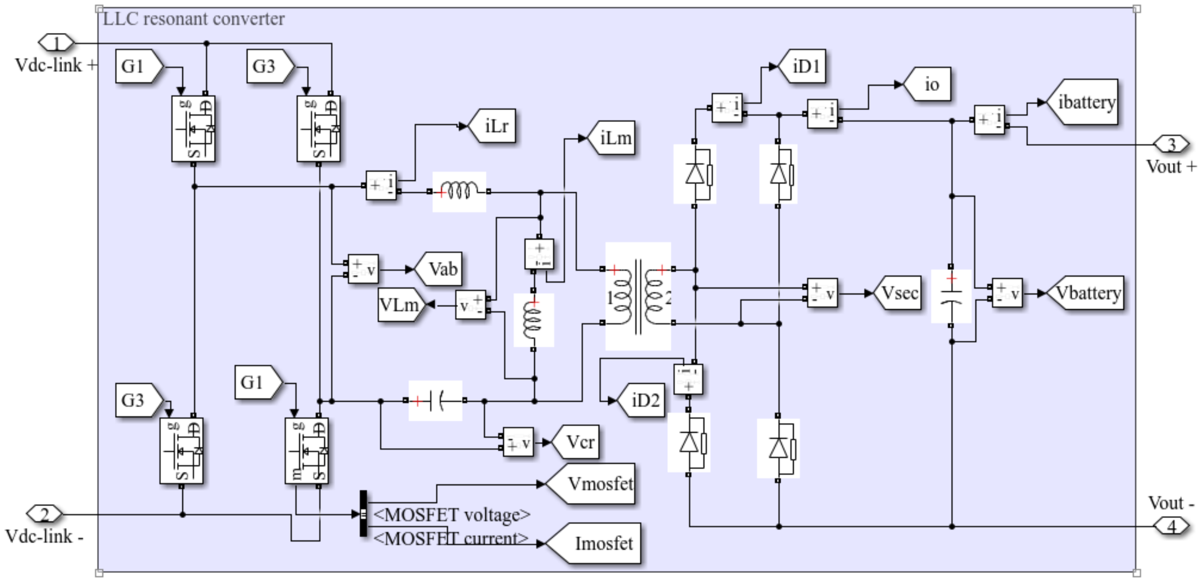

Figure B.4. Back end LLC resonant dc-dc converter

Appendix C: Related to the Battery Management System

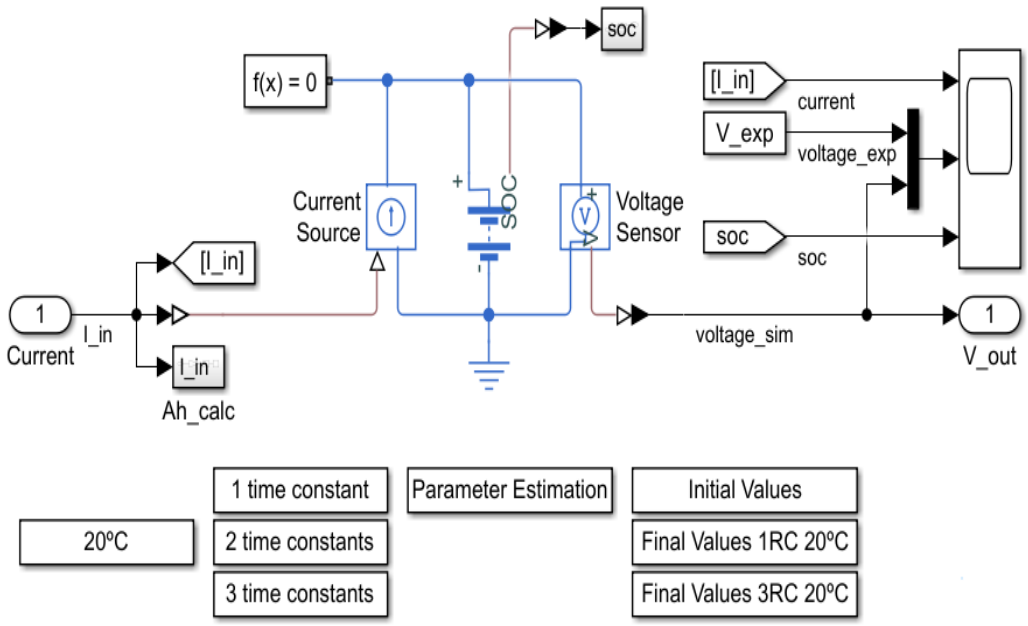

Figure C.1 Battery modeling and parameter estimation circuit.

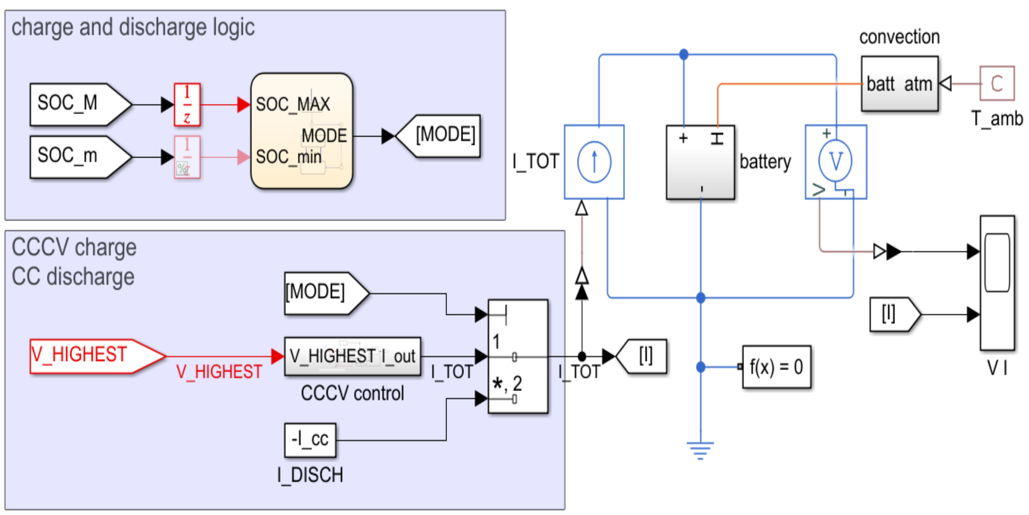

Figure C.2 Overall battery charging-discharging circuit

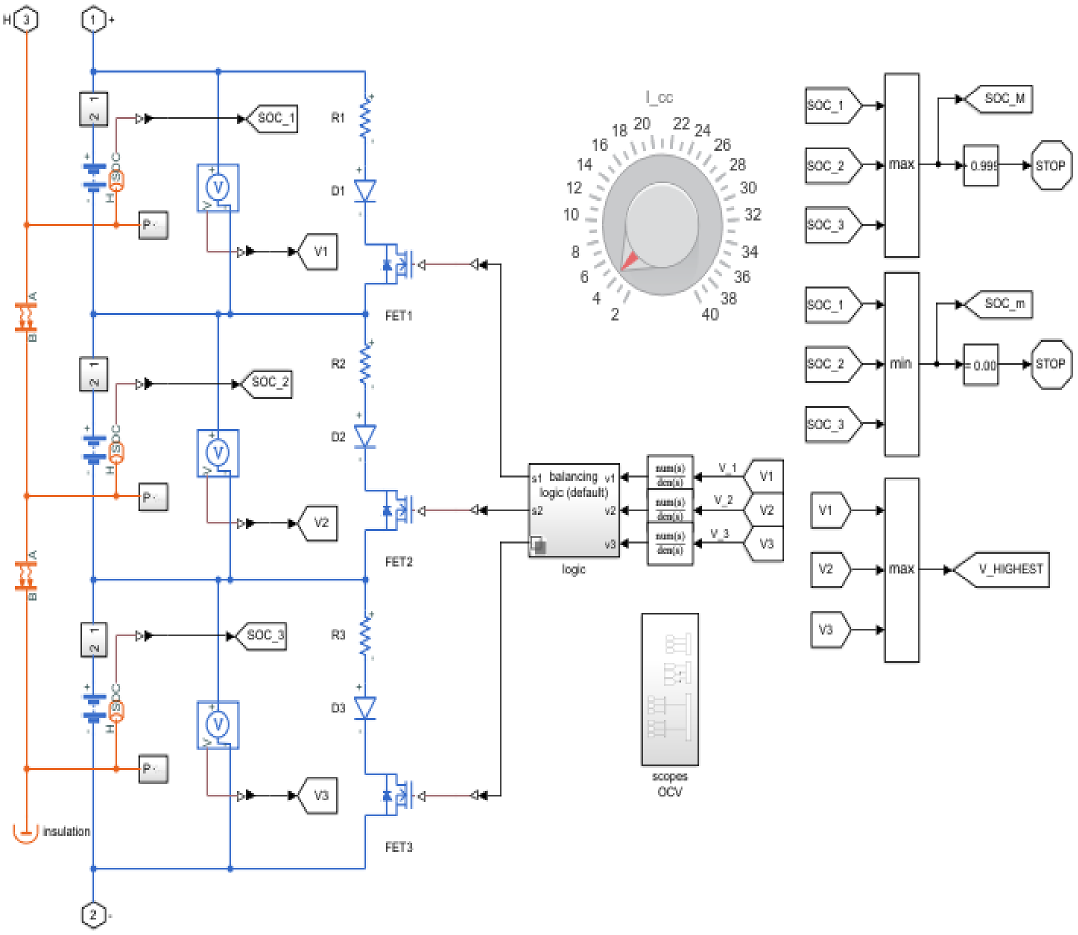

Figure C.3 Simulink model for cell balancing circuit

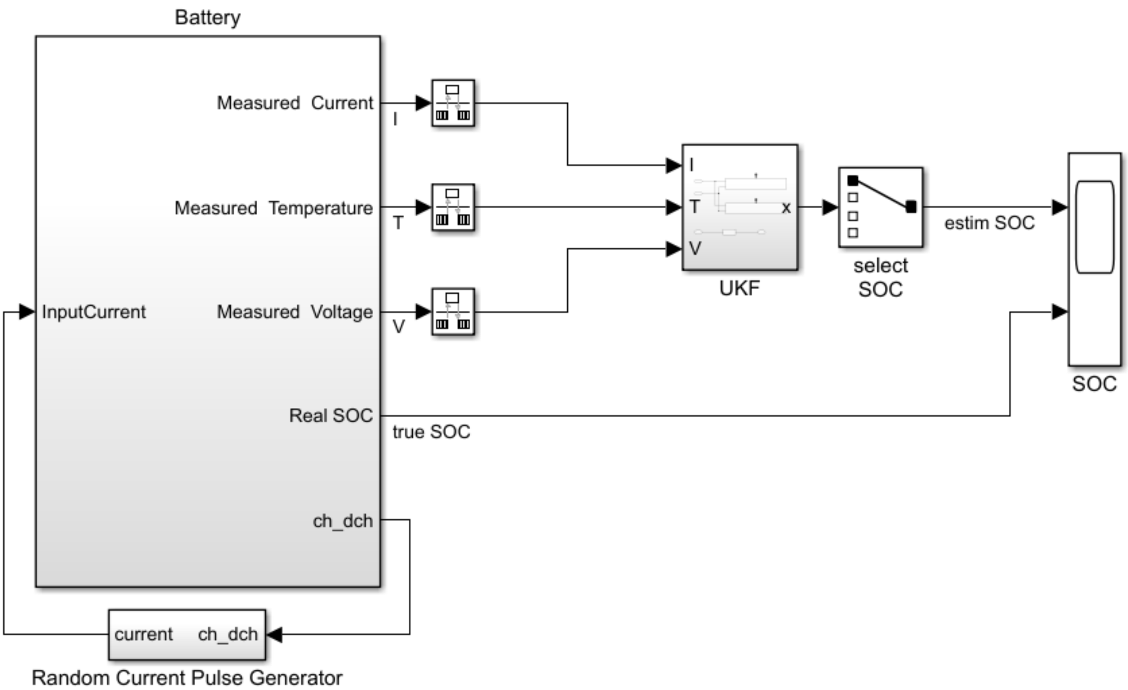

Figure C.4 Unscented Kalman filter based battery state of charge estimation circuit

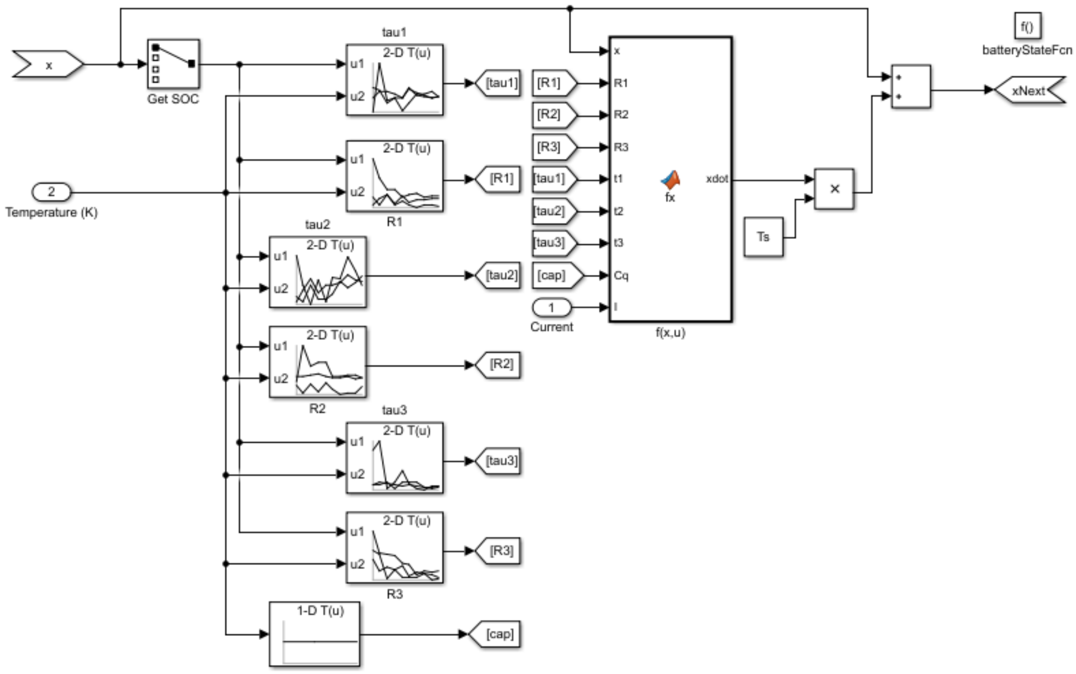

Figure C.5 State transition block for unscented Kalman filter algorithm

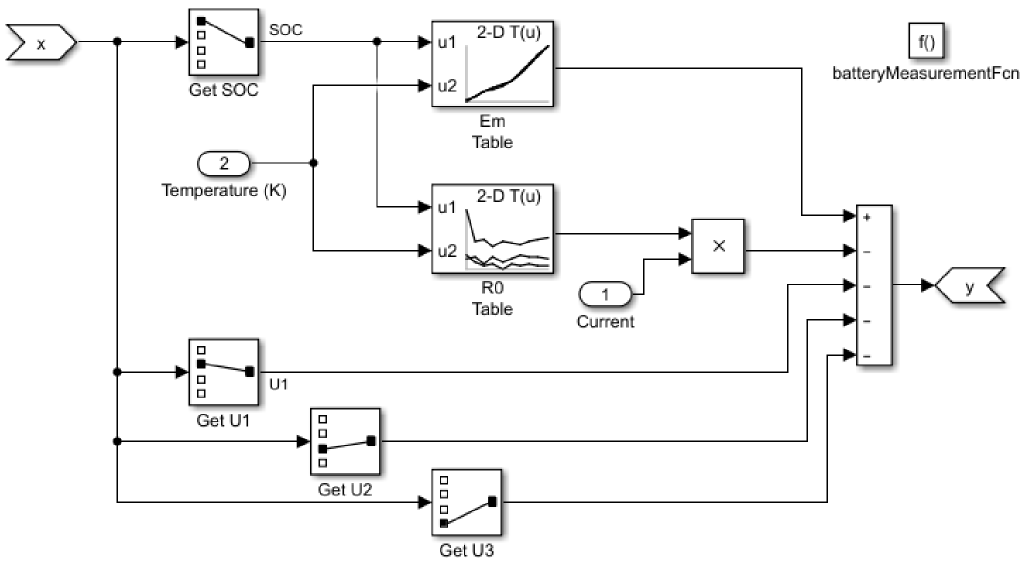

Figure A State measurement block for unscented Kalman filter algorithm

Appendix D. Appendixes Related to ECADO-4EV

D.1. Data’s from Center of transportation and Vehicle engineering ‘ASTU

I. Tractive motor and vehicle specification taken from ECADO-4EV proposal

Parameters	Values
Maximum power (KW)	100
Gross weight (kg)	1500
Rated power (KW/rpm)	60/3600
Maximum torque (NM/rpm)	320/1978
Rated torque (NM/rpm)	159.23/3600
Maximum speed (Km/hr.)	130
Rated speed (km/hr.)	100
Range (km/charge)	40
Seating capacity (person)	4

II. Battery specifications for [ECADO-4EV]

Parameters	Value[unit]
Cell type	Lithium iron phosphate
Total battery energy usage	32KWh
Rated DC voltage supply	360V
Capacity	90Ah
Dimension (W*D*H)	52*225*231cm
Energy density	154Wh/kg
Operating temperature	-10 to 50℃
Battery charging voltage range	320 to 420V

Appendix E: Appendixes Related to Data Collection

E.1. battery used in modeling the battery management system

Lithium ion

Cell Type UR18650W

Specifications

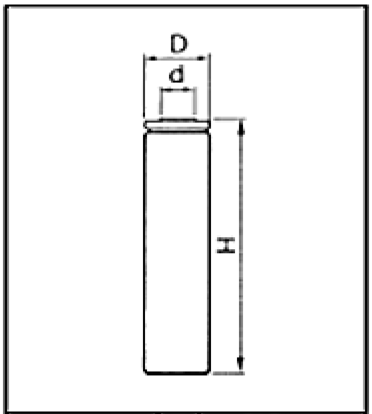

Dimensions(Typ.) of Bare Cell		
	H	64.7 mm
	D	18.05 mm
	d	9.0 mm

Nominal Capacity		Min.1500mAh
Nominal Voltage		3.7V
Charging Method		Constant Current -Constant Voltage
Charging Voltage		4.2V
Charging Current		Std. 1500mA
Charging Time		2.5hrs.
Ambient Temperature	Charge	0～+40℃
	Discharge	-20～+60℃
	Storage	-20～+50℃
Weight (Max.)		44.3g
Dimensions (Max.)	(D)	18.10mm
	(H)	64.80mm
Volumetric Energy Density		332Wh/l
Gravimetric Energy Density		125Wh/kg

Typical Characteristics

Discharge rate characteristics

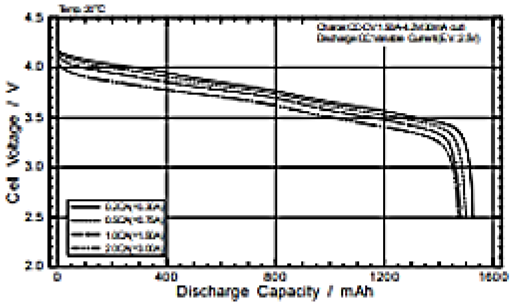

Discharge temperature characteristics

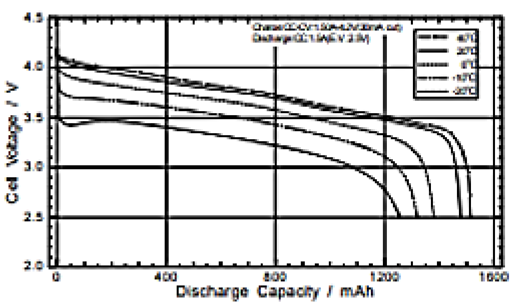

Charge characteristics